Karlsruhe Institute of Technology

Phase-field modeling of microstructural pattern formation in alloys and geological veins

Zur Erlangung des akademischen Grades

Doktor der Ingenieurwissenschaften

der Fakultät für Maschinenbau

Karlsruher Institut für Technologie

genehmigte

Dissertation

von

M.Tech. Kumar Ankit

am

Institut für Angewandte Materialien
Computational Materials Science (IAM-CMS)
der
Fakultät für Maschinenbau
des
Karlsruher Institut für Technologie (KIT)

Tag der mündlichen Prüfung:	15. Dezember 2015
Hauptreferent:	Prof. Dr. rer. nat. Britta Nestler
Korreferent:	Prof. Dr. rer. nat. Christoph Hilgers
Korreferent:	Prof. Dr. rer. nat. Hans Jürgen Seifert

Eidesstattliche Erklärung

Hiermit erkläre ich, dass ich die vorliegende Arbeit selbständig angefertigt und keine anderen als die angegebenen Quellen und Hilfsmittel benutzt sowie die wörtlich und inhaltlich übernommenen Stellen als solche kenntlich gemacht und die Satzung der Karlsruher Instituts für Technologie zur Sicherung guter wissenschaftlicher Praxis in der jeweils gültigen Fassung beachtet habe.

Hiermit weise ich ausdrücklich darauf hin, dass Kapitel 3, 4, 5, 6, 7, 8, 9, 10, 11 und 12 bereits veröffentlicht wurden, siehe Literaturstellen [5], [6], [7], [8], [9], [10] und [11].

Hiermit erkläre ich, dass für mich Promotionsverfahren außerhalb der Fakultät für Maschinenbau des Karlsruher Instituts für Technologie (KIT) weder anhängig sind noch erfolglos abgeschlossen wurden.

Hiermit erkläre ich, dass kein Strafverfahren gegen mich läuft.

Karlsruhe, den 17. August 2015

M.Tech. Kumar Ankit

Abstract

Microstructural patterns are as prevalent in metallurgical technologies, including alloy casting, primary metals production, welding, and soldering as in nature (e.g. snow flakes, frost, minerals and veins). Depending on the material in consideration (natural or synthesized), the interfacial energy is among one of the properties that can vary from being isotropic to strongly anisotropic. In the following thesis, the influence of interfacial energy on pattern evolution during diffusive phase transformations is studied.

In the first part of the following research, a grand chemical potential formulation of the multiphase-field model is employed with an objective to comprehend the influence of isotropic interfacial energies along with other relevant properties and boundary conditions on the microstructural evolution during eutectoid transformation in Fe-C steels. The required thermodynamic information to calculate the driving force is obtained by coupling the phase-field solver with the CALPHAD database. The numerical model is used to simulate the pulling-away of the advancing ferrite-austenite interface from cementite, which results in a transition from lamellar to divorced eutectoid morphology. The influence of preexisting arrangement of phases, undercooling (below A_1) and grain size on the evolving patterns is investigated in detail. For the first time, the onset of a concurrent growth and coarsening regime at small inter-particle spacing and low undercooling is identified. Thorough analyses of the numerical results unravel the essential physics behind this complex spatial and temporal evolution pathway. The existing criteria is amended by constructing a Lamellar-Divorced-Coarsening (LDC) map. Based on the insights derived from parametric studies, factors that favor the evolution of a bimodal size distribution of cementite particles are elucidated.

In the following part, with the aim of understanding the pattern formation in strongly anisotropic systems, the multiphase-field model is used to numerically simulate the free as well as crack-sealing evolution in geological veins. The influence of different boundary conditions such as the crack roughness and opening rate on the vein tracking efficiency is established. The effect of other relevant parameters such as crack location, obliquity of opening, grain size, and orientations on the evolving vein microstructure is also studied and analyzed in detail. Results show many similarities with natural microstructures such as stretched crystals and unitaxial veins and compare well with the previous numerical findings. By adopting a thermodynamically consistent and numerically efficient phase-field approach, the benefits of accounting for an extra third dimensionality are explained. The 3D simulation results are supplemented by innovative numerical post-processing and advanced visualization techniques. The new methodologies to measure the tracking efficiency of fracture cements reflect the incremental fracture opening and demonstrate

the importance of accounting the temporal evolution of grains in 3D; no such information is usually accessible in field studies and difficult to obtain from laboratory experiments. For the first time, the relevance of fragment trails as potential indicators of the opening of crack-seal veins is explained. Finally, the evolution of fluid channel connectivity in 2D and 3D during the sealing process is analyzed.

The phase-field investigation of two distinct scientific problems in consideration suggest a strong influence of interfacial energy on the natural and induced pattern formation in diffusion-controlled regime. The scientific progress will accelerate in the near term is virtually assured, especially with the advent of high performance computing and maturation of simulation techniques. In future, this would in turn, promote further synergistic activities and advancements in the interdisciplinary context. The author looks forward to seeing those anticipated advances unfold in time.

Zusammenfassung

Mikrostrukturelle Muster sind in metallurgischen Technologien, wie beispielsweise der Herstellung von Gusslegierungen oder Primärmetallen, beim Schweißen oder Löten genauso weit verbreitet wie in der Natur (z.B. Schneeflocken, Raureif, Mineralien und Gesteinsadern). In Abhängigkeit der betrachteten Materialien (natürlich oder synthetisiert) ist die Oberflächenenergie eine der Eigenschaften, die zwischen isotrop und stark anisotrop variieren kann.

In der folgenden Arbeit wird der Einfluss der Oberflächenenergie auf die Musterbildung während diffusiver Phasenumwandlungen untersucht. Im ersten Teil wird ein Multiphasenfeldmodell mit einer Formulierung des Großkanonischen Potentials verwendet, um die Auswirkungen der isotropen Grenzflächenenergien zusammen mit anderen relevanten Eigenschaften und Randbedingungen auf die mikrostrukturelle Entwicklung, während eutektoider Umwandlungen in FeC-Stählen, zu analysieren. Die benötigten thermodynamischen Informationen zur Berechnung der treibenden Kraft werden durch Kopplung des Phasenfeldlösers mit der CALPHAD-Datenbank gewonnen. Mit Hilfe des numerischen Modells wird das Zurückdrängen von Zementit bei einer sich nähernden Ferrit–Austenit-Grenzfläche von Zementit simuliert, was zu einem Übergang von einer lamellaren zu einer getrennten eutektoiden Morphologie führt. Der Einfluss der vorgegebenen Phasenanordnung, der Unterkühlung (unter A_1) und der Korngröße auf die sich bildenden Muster wird ausführlich untersucht. Erstmals wird das Auftreten eines gleichzeitigen Wachstums– und Vergröberungsverhaltens bei kleinem Teilchenabstand und niedriger Unterkühlung ermittelt. Sorgfältige Analysen der numerischen Ergebnisse bringen Aufschluss über die grundlegenden physikalische Vorgänge hinter den komplexen räumlichen und zeitlichen Entstehungspfaden. Die existierenden Kriterien werden durch die Darstellung des Übergangs von lamellarem zu vergröbertem Wachstum (Lamellar-Divorced-Coarsening (LDC)) vervollständigt. Ausgehend von den hergeleiteten Erkenntnissen, der parametrischen Untersuchungen werden Faktoren, welche die Entwicklung einer bimodalen Größenverteilung von Zementitpartikeln begünstigen, erläutert.

Im zweiten Teil der Dissertationsschrift wird das Multiphasenfeldmodell mit dem Ziel verwendet, die Musterbildung in stark anisotropen Systemen zu verstehen, um sowohl freies Kristallwachstum als auch Kornstrukturausbildung bei der Rissversiegelung in Gesteinsadern numerisch zu simulieren. Der Einfluss verschiedener Randbedingungen, wie der Rauigkeit der Risse und der Öffnungsrate auf die Effizienz der Verfolgung des Aderverlaufes wird ermittelt. Die Auswirkung anderer relevanter Parameter, wie die Lage des Risses, die Unregelmäßigkeit der Öffnung, die Korngröße und ihre Orientierungen, wird auf die sich herausbildende Mikrostruktur der Gesteinsadern ausführlich untersucht

und analysiert. Die Ergebnisse zeigen viele Gemeinsamkeiten mit natürlichen Mikrostrukturen, wie gestreckte Kristalle und unitaxiale Adern auf und lassen sich gut mit den vorangegangenen numerischen Erkenntnissen vergleichen. Mit einem thermodynamisch konsistenten und numerisch effizienten Phasenfeldansatz werden die Vorteile einer zusätzlichen dritten Dimensionalität erläutert. Die Ergebnisse der 3D-Simulation werden durch innovative Post-Processing- und fortgeschrittene Visualisierungstechniken ergänzt. Die neuen Methoden zur Messung der Verfolgungseffizienz der Korngrenzen während des Bruchvorgangs spiegeln die inkrementelle Öffnungsweite wieder und zeigen, wie wichtig es ist, die zeitliche Entwicklung von Körnern in 3D zu untersuchen. Normalerweise sind derartige Informationen in Feldstudien nicht zugänglich und nur schwer aus Laborexperimenten zu erhalten. Erstmals wird die Relevanz von Fragmentspuren als mögliche Indikatoren für die Öffnungsgeschichte von versiegelten Gesteinsrissen aufgezeigt. Abschließend wird die Verbindung der Flüssigkeitskanäle während des Versiegelungsprozesses in 2D und 3D analysiert.

Die Phasenfelduntersuchungen in zwei Anwendungsbereichen unterscheidlicher Materialklassen und wissenschaftlicher Herausforderangen zeigen einen starker Einfluss der Grenzflächenenergien auf die natürliche und induzierte Musterbildung in einem diffusionskontrollierten Prozess. Der wissenschaftliche Fortschritt wird sich mit großer Sicherheit in naher Zukunft, besonders durch die Einführung von Hochleistungsrechnen und der raschen Entwicklung von Simulationstechniken beschleunigen. In der Zukunft wird dies wiederum weitere synergetische Aktivitäten und Fortschritte im interdisziplinären Kontext voran, treiben. Der Autor freut sich darauf, wenn sich diese erwarteten Fortschritte in absehbarer Zeit entfalten.

Dedicated to my late Nanaji,
a man of extraordinary intelligence,
of superb devotion and dedication to duty,
who taught me to believe in myself.

Acknowledgments

I feel ecstatic and a bit nostalgic as I start writing the last and arguably, the most important part of my thesis. First and foremost, I would like to express my sincere gratitude to my advisor, Prof. Britta Nestler for trusting my capabilities and her guidance. I also thank her for rendering full support in pushing various projects and initiating collaborations, which ultimately benefited the work reported in this thesis.

Profs. Abhik Choudhury and Rajdip Mukherjee deserve a special mention for helping me get started in the working group and for all their support as well as guidance that helped me finish my thesis within a considerably short time. The unconditional support rendered by the computer scientists, especially Dr. Michael Selzer and others proved pivotal in bringing this research to fruition and I acknowledge all your help.

Without the insightful discussions and collaborations with Profs. Janos Urai and Chris Hilgers, my research in the area of numerical modeling of geological veins would not have progressed in the manner it has. I greatly appreciate your guidance for the same. Janos, I completely agree with you when you say that geologists and numerical scientists tend to speak different language which makes the task of collaborating, all the more challenging! Thanks for being patient and taking out time to discuss all my queries as well as the finer details. I am also grateful to Prof. Peter Gumbsch for his valuable suggestions concerning the layout. I am very fortunate to be part of such an amazing research group and I would like to thank all the group members for encouraging discussions on a day-to-day basis.

I would like to thank my family for their love and support which has made all this possible. My parents have always been proud of my endeavors, while simultaneously giving me the freedom to choose my own destiny. The encouragement from Ayush and Amrita have been all the while a great driving force. In fact, I have a tremendous feeling of self-confidence and -assurance as long as both of you guys are around.

I thank my wife Advaita for her constant support and patience over the last years while I was working on this thesis. Adu, I thank you for keeping me sane over the past few months and above all, being my true friend. I owe you everything!

Finally, the work reported in this thesis would not have been possible without the financial support of German Research Foundation within the framework of Graduate School 1483 – Process chains in production.

– Kumar Ankit
Karlsruhe, August 2015

Preface

Numerical modeling and analysis of microstructural evolution is a topic of broad scientific interest. Due to it's versatility, the phase-field method, which essentially is a popular approach in the material science community to model phase transformations has been extended to study natural phenomena pertaining to geophysics and biology.

The present thesis, which is largely inspired by the evolving interdisciplinary context of the phase-field approach, explores it's applicability in the modeling of microstructural pattern formation processes. Exemplary application areas include eutectoid transformation in binary steels and polycrystalline evolution in geological veins. In Part I, a brief overview of the previous developments, with a special focus on various application areas of the phase-field method is presented. The state-of-the-art numerical modeling techniques to simulate polycrystalline evolution in veins are also described. In Part II, the multiphase-field model equations and the extension to grand chemical potential approach are elucidated. Special emphasis is laid on the incorporation of faceted anisotropy in the surface energy and its influence on the temporally evolving patterns as compared to isotropic case. Numerical results reported in Parts III (considers isotropic surface energy) and IV (considers faceted anisotropy in surface energy) were published in the following peer-reviewed articles:

Article 1: K. Ankit*, A. Choudhury, C. Qin, S. Schulz, M. McDaniel, B. Nestler, Theoretical and numerical study of lamellar eutectoid growth influenced by volume diffusion, *Acta Materialia* 61 (2013) 4245–4253.

Article 2: K. Ankit*, R. Mukherjee, T. Mittnacht, B. Nestler, Deviations from cooperative growth mode during eutectoid transformation: Insights from a phase-field approach, *Acta Materialia* 81 (2014) 204–210.

Article 3: K. Ankit*, T. Mittnacht, R. Mukherjee, B. Nestler, Evolution of mixed cementite morphologies during non-cooperative eutectoid transformation in Fe-C steels, *Computational Materials Science* 108 (2015) 342–347.

Article 4: K. Ankit*, R. Mukherjee, B. Nestler, Deviations from cooperative growth mode during eutectoid transformation: Mechanisms of polycrystalline eutectoid evolution in Fe-C steels, *Acta Materialia* 97 (2015) 316–324.

Article 5: K. Ankit*, B. Nestler, M. Selzer, M. Reichardt, Phase-field study of grain boundary tracking behavior in crack-seal microstructures, *Contributions to Mineralogy and Petrology* 166 (2013) 1709–1723.

Article 6: K. Ankit*, M. Selzer, C. Hilgers, B. Nestler, Phase-field modeling of fracture cementation processes in 3D, *Journal of Petroleum Science Research* 4 (2015) 79–96.

Article 7: K. Ankit*, J. Urai, B. Nestler, Microstructural evolution in bitaxial crack-seal veins: A phase-field study, *Journal of Geophysical Research - Solid Earth* 120 (2015) 3096–3118.

Part V concludes the thesis.

At this point, I would like to clarify that the above articles are published as a part of my research since June 2012, while I was a doctoral student at the Faculty of Mechanical Engineering, Karlsruhe Institute of Technology and simultaneously employed (as a collegiate) at the DFG Graduate School - 1483 (Project Number B8). All the corresponding co-authors as well as publishers have granted me their permission (in writing) to present the results in the current thesis. Unanimous written consent of every co-author concerning the description of their contributions have also been secured (refer to the exemplary declaration below and attached documents). Wherever applicable, such contributions are demarcated in footnotes. Unless otherwise stated, the scientific advancements reported in this thesis are *my* contributions. Written permissions to illustrate copyright images in chapter II of this thesis were secured from the corresponding publishers. License for usage of copyrighted images is limited to the following thesis.

* Corresponding author

No Objection Certificate

As a co-author, I hereby claim no objection if the first author (Mr. Kumar Ankit) uses the attached article(s) entirely or in-parts, for his doctoral thesis submitted to Faculty of Mechanical Engineering, Karlsruhe Institute of Technology. Further, I do not object to the description of my contributions as laid in Kumar Ankit's thesis.

This specific no objection certificate is being issued on the specific request by the first author.

– Signed by all the co-authors
August 2015

Declaration of originality

Respondents' contribution to the articles

Article 1: As first author, the respondent (Kumar Ankit abbreviated as K.A.) performed all the phase-field simulations and wrote the entire article with inputs from A. Choudhury (A.C.), C. Qin (C.Q.), and B. Nestler (B.N.). The fitting of thermodynamic free energies is performed along with S. Schulz (S.S.) and M. McDaniel (M.M.) [5].

Article 2: As first author, the respondent performed all the phase-field simulations and wrote the entire article with inputs from R. Mukherjee (R.M.), T. Mittnacht (T.M.) and B.N [6].

Article 3: As first author, the respondent performed all the phase-field simulations and wrote the entire article with inputs from T.M., R.M. and B.N [7].

Article 4: As first author, the respondent performed all the phase-field simulations and wrote the entire article with inputs from R.M. and B.N. [8].

Article 5: As first author, the respondent performed all the phase-field simulations and wrote the entire article with inputs from B.N. M. Selzer (M.S.) and M.Reichardt (M.R.) helped with post-processing algorithms and 3D visualization [9].

Article 6: As first author, the respondent performed all the phase-field simulations and wrote the entire article with inputs from C. Hilgers (C.H.) and B.N. M.S. helped with post-processing algorithms and 3D visualization. Thin section images of polycrystalline quartz are contributed by C.H. [10].

Article 7: As first author, the respondent performed all the phase-field simulations and wrote the entire article with inputs from J. Urai (J.U.) and B.N. Thin section images of bitaxially-sealed veins are contributed by J.U. [11].

The scientific inputs from co-authors are demarcated in footnotes, wherever applicable, in the following thesis.

Contents

List of Figures

List of Tables

Part I.

Introduction and literature review

1. Introduction: Synopsis

In the present thesis, the applications of phase-field method as a microstructure modeling tool in two different study areas are presented. In particular, it has been explored how the concepts of phase-field technique which primarily originated to tackle the phase transition problems pertaining to metal physics can be extended to study polycrystalline evolution in geological veins. The research contents is classified into 3 categories:

- Phase-field modeling of the eutectoid transformation in binary Fe-C steel.
- Phase-field modeling of the polycrystalline evolution in geological veins.
- Establishing synergies between the numerical results and experimental/field findings.

The numerical investigations are performed with an objective to simulate typical morphological patterns observed in laboratory experiments as well as in nature. Polycrystalline evolution in geological veins is simulated by using the multiphase-field model developed by Nestler et al. [1]. The numerical simulations of the eutectoid transformation in binary (Fe-C) steels is performed using the grand-chemical potential formulation (Choudhury and Nestler [2]) of the multiphase-field model. Apart from being of scientific importance, the present work demonstrate the general capability of the multiphase-field model to advance the understanding of the physics of moving-boundary problems at the mesoscale. In the following sections, a brief overview of the work is presented.

1.1. Phase-field modeling of the eutectoid transformation in binary Fe-C steel

This portion of the thesis deals with the multiphase-field modeling of the eutectoid transformation in binary steels (Fe-C). In order to quantitatively model the kinetics of transformation, the grand-potential formulation [2] is used. The variation of the grand-potential of the three phases namely, ferrite, austenite and cementite, are approximated using a polynomial of second degree. The corresponding coefficients are extracted from the thermodynamic functions of the respective phases that are derived from the CALPHAD database [3]. The work is further categorized into two:

1.1.1. Cooperative growth

This first part of this study (Chapter 5) concerns with the cooperative mode where the product phases (ferrite and cementite) evolve cooperatively, sharing a common growth front with the parent phase (austenite). The resulting morphology is the well-known pearlitic structure (lamellar). To begin with, the Jackson-Hunt analysis [4] is extended to account for diffusion in the growing phases. Next, the lamellar growth rates obtained from the phase-field simulations are validated by comparing with the analytical results. A detailed parametric study reveals that diffusion in austenite as well as ferrite leads to the formation of tapered cementite along with an overall increase in the transformation kinetics as compared to diffusion in austenite (only). As the objective of this part of the work is not to consider the pearlitic transformation in totality, diffusion in the phase interfaces is not considered. A near overlap of the numerically simulated and analytical result demonstrate that the objective of the present work have been adequately achieved. The limitations of the presented model as well as possible extensions are discussed at length.

1.1.2. Non-cooperative growth

Experimental findings suggest that the relative contribution of the carbon diffusive flux along the interphase interfaces as well as in the phase volumes determines the mechanism by which eutectoid transformation proceeds.

In the second part (Chapter 6), I incorporate the diffusion along the transformation front into the previous modeling approach and simulate the non-cooperative evolution of ferrite/austenite advancing front. In particular, I investigate the influence of undercooling (below A_1 temperature) and interparticle spacing (λ) in facilitating a pull-away of advancing ferrite/austenite transformation front as it forms interfaces with preexisting cementite particles.

These studies are extended further to investigate the influence of arrangement by assuming a preexisting configuration of phases that consist of a random arrangement of cementite particles (Chapter 7). By investigating the influence of parameters such as prior austenite grain size and thickness of preexisting ferrite layers, I provide explanations and propose mechanisms that contribute to the formation of a bimodal distribution (Chapter 8) of cementite particles in the final microstructure.

1.2. Phase-field modeling of the polycrystalline evolution in geological veins

Vein formation in earth's crust involves a complex interplay of material transport and local precipitation during ongoing deformation. The geological experts try to correlate

the different indicators which may vary across length scales, to reconstruct the past events, in order to gain an understanding of vein formation. However, it is difficult to decompose the effect of different processes that might have acted in sequence or simultaneously in such studies. The approximate reconstruction, which determines the final vein morphology could often be misleading and may result in erroneous interpretation of evolution mechanism. On the contrary, numerical methods applied to the study of vein microstructure formation improves the general understanding, as it is possible to decompose the effect of various boundary conditions. Further, computations provide an in-situ look into the temporal evolution of grains. In spite of numerous attempts in the past to simulate the dynamics of vein growth process, numerical studies are limited to two dimensions. It is to be noted that the grain formation process is generically of 3-D nature and can be interpreted in a physically sufficient manner by methods capable of capturing the growth characteristics and dynamics in full 3-D space.

In the present dissertation, I start by conducting 2D simulations of the vein evolution in unitaxial veins establish a synergy with the natural microstructures as well as with the previous simulations using the front-tracking method (Chapter 10). Then, I extend the previous numerical studies to 3D and analyze the complex morphological evolution in unitaxial veins by the application of advanced post-processing (such as numerical masking) and visualization techniques (Chapter 11). The adopted phase-field approach is validated by analyzing the growth competition arising due to relative misorientation w.r.t to the most-preferred orientation. Finally, the developed approach is extended (Chapter 12) to simulate the morphological evolution in bitaxial vein sealing (in 2D as well as 3D). For the first time, the mechanism by which crystal fragments evolve is discussed and analyzed in the context on deducing back the crack-opening history. Formation of other associated patterns such as stretched crystals and bridges and dynamics of vein permeability are also addressed.

1.3. Establishing synergies between the numerical results and experimental/field findings

In the present dissertation, a strong emphasis is laid on the comparison of numerical results with *real world* findings. In both the application areas, the numerically simulated morphologies are in good agreement with the those observed in experimental or natural microstructures.

For the case of non-cooperative eutectoid transformation, the experimental Lamellar-Divorced transition curve (undercooling plotted against interparticle spacing) is qualitatively reproduced using the phase-field approach ([6]). As the numerically simulated eutectoid transformation that proceeds from a random arrangement of cementite particles and grain boundary ferrite layers, both embedded in polycrystalline austenite, nears completion, particle loops, elongated and bell-shaped morphologies are found to evolve

[8]. Such morphological features bear a strong resemblance with those observed in typical divorced eutectoid microstructures obtained after intercritical annealing.

In the geological arena, simulations of freely evolving quartz polycrystals in liquid show a good comparison with the blocky microstructures [10]. The accepted mechanism of growth competition that sets in due to relative misorientation of grains is also fully recovered using the present approach. Phase-field simulation of unitaxial vein patterns show similarities with the field findings (for e.g. wave-like grain boundaries [9]) that are reported previously. In bitaxial veins, the numerically simulated stretched crystal are shown to compare favorably with the natural examples [11]. Till date, the viability of crystal fragments (known to co-exist with stretched crystals) in recording the rock deformation history have been largely ignored. The simulated fragmented trails that essentially evolve due to growth competition (depending on relative misorientation) compare well with the natural prototypes.

2. Background

2.1. Phase-field modeling and applications

Most materials, whether natural or synthesized are heterogeneous at the mesoscale. Developing an understanding of how they form is a challenge from an industrial as well as philosophical perspective. Many of these materials are polycrystalline, such as metals, minerals, food, ice, snow, cholesterol, kidney stone *etc.*, whose properties are determined by their *microstructure* [12]. Since the mechanical properties of such systems are to a large extent determined by the phases present in their microstructures, acquiring a precise understanding of the mechanisms that drive the phase transformation is a great challenge for scientists, who work in this field.

In the last few decades, the phase-field method has shown tremendous capabilities in accurately predicting the microstructural evolution at the mesoscale. Typical application areas include pattern formation in physics, materials science, geology, biology and medicine. As the present doctoral thesis is largely inspired by the interdisciplinary research activities within the phase-field community, a brief literature overview summarizing the important developments is presented.

2.1.1. Historical developments

The phase-field approach's popularity is due to the elegance with which it treats moving boundary problems. The interface representing the boundary between two mobile phases or grains is replaced with a smoothly varying phase-field parameter, whose change represents phase evolution. The physics of diffusive and displacive mechanism are incorporated, and creation, destruction, and merging of interfaces are handled implicitly.

The history of phase-field modeling dates back to a century-back era of van der Waals [13] who modeled a liquid–gas system by means of a density function that varies continuously at the liquid–gas interface. Much later, Ginzburg and Landau [14] formulate a model for superconductivity using a complex valued order parameter and its gradients. In their pioneering work, Cahn and Hilliard [15] propose a thermodynamic formulation that accounts for the gradients in thermodynamic properties in heterogeneous systems with diffuse interfaces.

Important theoretical developments during the past decades led to the modern use of phase field methods in materials science. The earlier works primarily focus on

dendritic solidification of pure and binary materials. Langer [16] and Fix [17] were the first to introduce a phase-field model for the study of first-order phase transformation. Simultaneously, Collins and Levine also develop a similar diffuse interface model [18]. Langer and Sekerka [19] consider a diffuse interface model for binary alloy system with a miscibility gap in solid solution phase. Caginalp et al. [20–24] investigate the effects of the anisotropy and the convergence of the phase-field equations to the conventional sharp interface models in the limit of vanishing interface thicknesses. Penrose and Fife [25, 26] provide a framework for deriving the phase-field equations in a thermodynamically consistent manner, which allowed for the modeling of non-isothermal solidification

In spite of the earlier developments, the application of phase-field model to study microstructural emerge as fascinating discipline only by 90's. Two types of phase-field models exist: The first kind of approach [27, 28] is derived from the microscopic theory of Khachaturyan [29]. The phase-field variables are related to microscopic parameters, such as the local composition and long-range order parameter fields reflecting crystal symmetry relations between coexisting phases. The model has been applied to a variety of solid-state phase transformations (see [30] for an overview) that involve a symmetry reduction, for example the precipitation of an ordered intermetallic phase from a disordered matrix [31, 32] and martensitic transformations [33, 34]. It was also applied to ferroelectric [35, 36] and magnetic domain evolution [37] (refer to [38, 39] for a detailed overview) and can account for the influence of elastic strain energy on the evolution of the microstructure. A similar approach has been adopted to study the interaction of stress, strain and dislocations with the evolving precipitate and displacive transformations [40–42].

In the second approach, the numerical interface width is allowed to exceed the physical width, however, doing so leads to the introduction of unsolicited error that scales with the interfacial width [43]. Development of thin-interface models is therefore, a valuable stride in this direction as they converge to the Gibbs-Thomson relation in the limit of vanishing interfacial width [44, 45]. In such models, the excessive solute trapping that occurs due to a choice of large interfacial width can be remedied by application of antitrapping currents [46].

Wheeler et al. [47] develop a model for studying the solidification in binary alloys. Kim et al. [48] show the existence of a potential excess, arising from the variation of the grand chemical potential across the interface at equilibrium. This model was also extended to multi-component systems together with the incorporation of anti-trapping currents [49]. Tiaden et al. [50] propose a solution to this problem by adopting different concentration fields for the solid and the liquid, connected to each other through a partition coefficient, which is a function of velocity. Cha et al. [51] develop a model on similar lines, as the model of Kim. In order to circumvent this problem, some more related variational and non-variational methods were formulated by Folch and Plapp [43, 52] for two phase eutectic solidification, without the use of separate concentration fields for the solid and the liquid.

Owing to a genuine requirement to address topological changes in multicomponent and

multiphase systems, Steinbach et al. [53], Garcke et al. [54] and Nestler et al. [1] develop the multiphase-field model to study the complex interaction of arbitrary number of phases. Tiaden et al. [50] extend the multiphase-model of Steinbach to incorporate solute diffusion into the multiphase field approach. An important advancement in the quantitative modeling that is built upon the multiphase-field model of Nestler, is the grand-chemical potential model [2], which conceptualize the decoupling of bulk and interfacial energy contributions in the total free energy, to facilitate an increase in the length-scale of numerical simulations. Kobayashi et al. [55, 56] and Gránásy et al. [57] develop vector-valued models in which the phase-field parameter is coupled with an orientation field for representing different crystal or grain orientations.

2.1.2. Solidification of pure metals and alloys

Dendrites are easily the most widely studied microstructures in the area of solidification in metals, polymer, ceramics and concrete. The first large scale simulations of thermal dendrites of snow was reported by Kobayashi [58]. Parallel attempt was made by Wheeler et al. [59] to quantitatively compare the morphology of the dendritic tip with the Ivantsov solutions [60, 61]. Warren and Boettinger [62] employ a thermodynamic consistent model to simulate solutal dendrites in Ni-Cu alloys (Figure 2.1). The thin interface limit proposed by Karma and Rappel [44, 45] for pure metals was extended by Losert et al. [63]. for binary alloy, thereby, paving way for quantitative simulations. Danilov and Nestler [64] study the dendritic to globular transition in ternary, glass-forming $Ni_{60} - Cu_{40} - xCr_x$ alloys. The developed approach show good agreement with experiments [65, 66].

From an engineering perspective, eutectic alloys are useful owing to their low melting temperature and the superior mechanical properties that they posses by the virtue of their homogeneous microstructure. The first ever phase-field model to simulate eutectic solidification was developed by Karma [67]. The results of the average interface undercooling and the minimum undercooling spacing accentuated the predictions of the classical *Jackson-Hunt theory* [4]. Karma and Sarkissan [68] employ a boundary integral method to investigate purely oscillatory and tilted states in eutectic solidification. A multi-component multiphase-field technique was employed by Nestler and Wheeler [69], for the first time, which illustrate different oscillatory patterns in 2D (Figure 2.2). Kim et al. [70] and Plapp [71] report a systematic study of the instabilities in 3D. Parisi et al. [72] perform 3D phase-field simulations to investigate morphological transitions from rod to lamellar during directional solidification (Figure 2.3).

Many commercially important alloys exhibit peritectic transitions during solidification, Fe–C, Fe–Ni, Cu–Zn, Cu–Sn and Ti–Al being commonly known. From the perspective of pattern formation, peritectic reactions are known to yield different kinds of microstructures. One of the varieties is the engulfing microstructure in which, the peritectic phase grows over the pro-peritectic phase in the form of spherical nuclei, or infinite plate. The phase-field study of the evolution of such microstructures have been reported by Tiaden et al. [50], Nestler and Wheeler [69] and Choudhury et al. [73] (Figure 2.4) . The stability

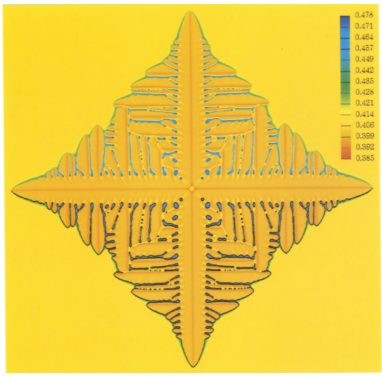

Figure 2.1.: A plot of the concentration and phase field profiles for a nickel-copper alloy. The calculation was done on a 750×750 grid, and then reflected about the x and y axes. The colors range from red (lowest concentration) to green (central concentrations) to blue (highest concentrations). The dark black lines shown in the lower half of the figure are the phase field contours from $\phi = 0.1$ to 0.9. The diffusion rate in the solid is assumed to be 10^{-4} times smaller than the liquid diffusion rate. Reprinted from [62] copyright (1995), with permission from Elsevier.

of other variants such as the banded structures and those evolving by the island and coupled mechanisms have also been examined using the phase-field method [74].

Aluminum and copper based monotectic alloys have been intensively investigated during last decades as possible new bearing materials [75]. Since the process of monotectic solidification involves the interaction of two fluids of differing concentration, a number of physical phenomena resulting from the coupling of the fluid properties with the diffusion and capillary effects influence the final microstructure. The first phase field method used for studying monotectic solidification was reported by Nestler et al. [76]. Tegze et al. [77] use a Cahn-Hilliard approach that was coupled with the Navier-Stokes equations to study the influence of thermal Marangoni convection on the coagulation and size distribution of droplets in Al-Bi alloys. This work, however, did not address the monotectic reaction entirely and is limited to the study of liquid-state phase separation. Wang et al. [78] adopt a similar approach to study the influence of solutal Marangoni convection on the size distribution of droplets in Fe-Sn alloys (Figure 2.5). The simulated size distributions in presence of solutal Marangoni convection, which show a characteristic departure from the Lifshitz-Slyozov-Wagner (LSW) theory, compare well with the analytical results of Ratke and Thieringer [79]. In parallel, Wang et al. [80] also develop a new model for monotectic solidification to study the decomposition of the parent liquid phase into

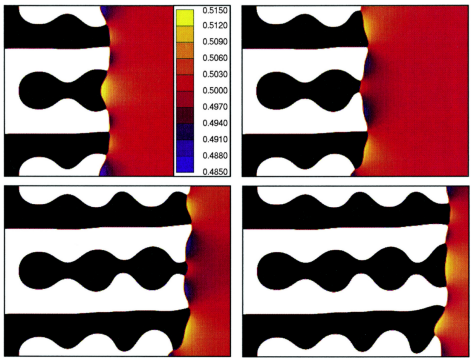

Figure 2.2.: Simulation of varicose instabilities that occur during eutectic growth after new lamellae have been formed by nucleation. The microstructural evolution is shown at four representative time steps. Reprinted from [69] copyright (2000), with permission from Elsevier.

product solid and liquid phases.

A more detailed review of the above developments can be found in the review articles of Boettinger et al. [81], Singer-Loginova and Singer [82], Moelans et al. [83], Asta et al. [84], Provatas and Elder [85] and Nestler and Choudhury [86].

2.1.3. Solid-state transformations

Based on kinetic considerations, the solid-state transformations can be categorized into (a) Diffusion controlled and (b) Displacive [87]. The following section provides an overview on the application of phase-field models to investigate solid-state transformations in steels, with a special focus on diffusive transformations. For a more general review of the solid-state transformations in multicomponent alloys, the reader is referred to the review article of Thornton et al. [88].

A cursory look on the available literature reveals that the austenite-ferrite transformations is an area, which has been actively investigated using the phase-field method. The first works in this area was reported by Yeon et al. [89], who analyze the local equilibrium conditions for Fe–Cr–Ni and para-equilibrium conditions for the Fe–C–Mn alloys. Loginova et al. [90] develop a phase-field model for binary Fe-C alloys to investigate the transition between diffusion controlled and *partitionless* massive transformations in 1D. In the following work, Loginova et al. [91] incorporate an anisotropic ferrite/austenite interfacial energy function to study the two-dimensional evolution of Widmanstätten ferrite in

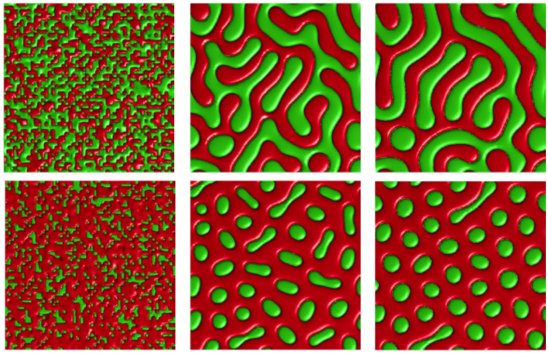

Figure 2.3.: Evolution of lamellar pattern with isolated rods (top) and rod patterns with isolated lamellae (bottom) in symmetric model alloy, depending upon eutectic composition. Reprinted from [72] copyright (2010), with permission from IOP publishing.

Fe–0.22%C alloy (Figure 2.6). Yamanaka et al. [92] propose an alternative approach to incorporate the interfacial energy anisotropy and report a similar computational study. Recently, Yan et al. [93] investigate the evolution of Widmanstätten plates by using the Kim-Kim-Suzuki's (KKS) and Loginova's phase-field models and compare the simulated plate spacing obtained from the two different approaches with experimental findings, respectively.

Nakajima et al. [94] report a phase-field study of the cooperative growth mode during the pearlitic transformation in Fe-C alloys. Although, the simulated growth rates (at different interlamellar spacings) of the pearlitic lamellae show a reasonable agreement

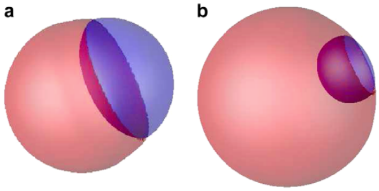

Figure 2.4.: Phase-field simulation of the process of pro-peritectic phase engulfment in 3-D at (a) an early stage and (b) a late stage of the peritectic reaction. Reprinted from [73] copyright (2010), with permission from Elsevier.

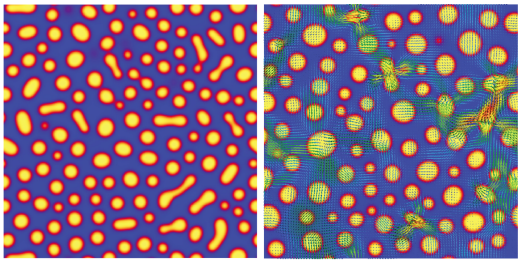

Figure 2.5.: Phase separation morphologies in Fe-40 at.% Sn alloy without (left) and with (right) solutal Marangoni convection. Reprinted from [78] copyright (2012), with permission from American Physical Society.

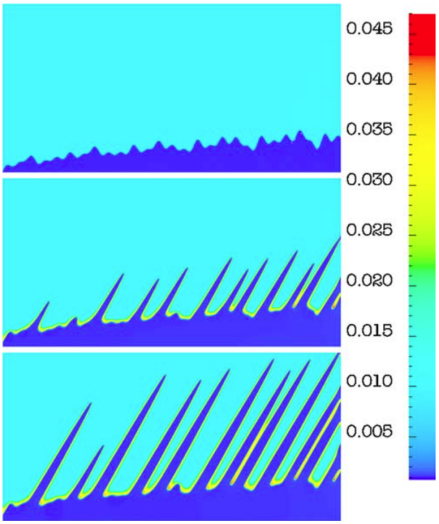

Figure 2.6.: Phase-field simulation illustrating the evolution of Widmanstätten plates. Reprinted from [91] copyright (2004), with permission from Elsevier.

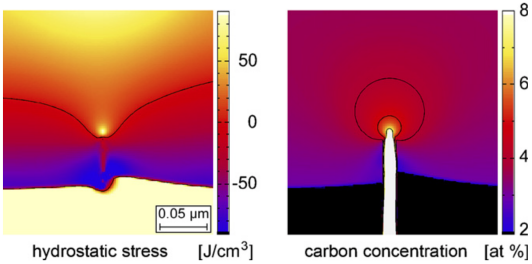

Figure 2.7.: Snapshot of the tip region as calculated for the staggered growth mode. Left: Hydrostatic stress. The austenite around the cementite tip is under large expansion, caused by the lattice match to cementite. A large part of the expansion is compensated by enrichment of carbon. Therefore elastic stress is limited to 90 MPa. The iso-line divides compressive (middle) from tensile stress. Right: Carbon distribution around the cementite tip. The carbon enrichment is mainly due to the expansion of the austenite lattice. The concentration reaches its maximum at 6 at.% in austenite. Reprinted from [97] copyright (2007), with permission from Elsevier.

with the Zener-Hillert theory [95, 96], which excludes the diffusion in growing phase as well along the transformation front, sufficient closure with the experimental findings could not established. Steinbach and Apel [97] extend their previous study by incorporating the effects of lattice strain on the pearlitic transformation (Figure 2.7). However, Pandit and Bhadeshia [98, 99] have been critical of such efforts and assert that the pearlitic transformation proceeds by a re-constructive mechanism.

In view of such criticisms, Ankit et al. [5] recently investigate the lamellar growth of pearlite in the volume-diffusion controlled regime by comparing the results of an extended *Jackson-Hunt* analysis that accounts for the diffusion of solute in all phases, with the numerical findings. In the following work [6], diffusion along the transformation front was incorporated and the new model was used to study non-cooperative evolution of the ferrite/austenite front that results in a product phase typically known as the *divorced eutectoid*. Both these works are discussed in detail, in the following chapters.

Microalloying small amount of elements (0.05 to 0.15%) in steel, such as Nb, V, Ti, Mo, Zr, B and rare-earth metals, facilitate precipitation hardening and grain refinement [100]. Mecozzi et al. [101–103] report 2D phase-field studies to describe continuous cooling transformation kinetics in low-carbon steels including a Nb microalloyed grade. These findings replicate the mixed-mode characteristics of the austenite to ferrite decomposition as reported by Sietsma and Zwaag [104]. First 3D investigation of the austenite-ferrite transformation during continuous cooling in 0.1 wt.%C–0.49 wt.%Mn alloys was reported

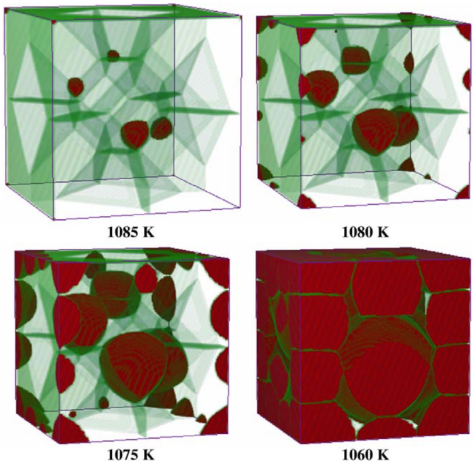

Figure 2.8.: Predicted 3D microstructure evolution for 0.4 K/s using the initial tetrakaidecahedron configuration; ferrite shown in red and interfaces in green. Reprinted from [105] copyright (2006), with permission from Elsevier.

by Militzer et al. [105] (Figure 2.8).

In comparison to the austenite-ferrite transformation, phase-field studies of the reverse transformation i.e. austenite formation has not been as frequently reported. Thiessen et al. [106, 107] employ a phase-field model in 2D to investigate the austenite formation from a mixture of ferrite-pearlite and ferrite-martensite structures during heat treatment cycles. However, the developed model has a drawback that the pearlite is treated as a supersaturated ferrite and the pearlitic lamellae are not resolved. Savran [108] build upon this earlier work and attempted preliminary simulations of intercritical austenite formation. Azizi-Alizamini and Militzer [109, 110] simulate austenite formation in the Fe–C system using ultra-fine ferrite–cementite aggregates, pearlite and ferrite–pearlite as the initial microstructures. More recently, Rudnizki et al. [111] use the pseudo-phase approximation to model pearlite to austenite decomposition in 2D, using the multiphase-field approach. In spite of the reported advancements in computational modeling of austenite formation, the modeling efforts in this direction are still at a nascent stage and therefore, need to be developed further.

The phase-field models have been extensively used to simulate static and dynamic recrystallization [112–115], normal and abnormal grain growth [116–120] and the influence of particle pinning [121–123]. Recently, the approach has been extended to model austenite grain growth in the heat-affected zone of a Nb–Ti microalloyed low-carbon steel [124].

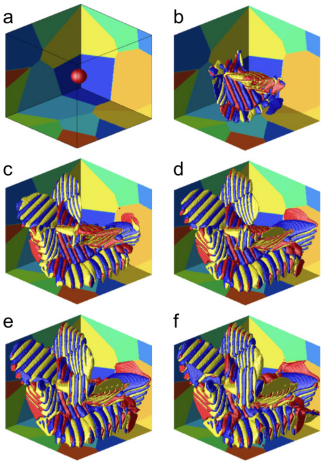

Figure 2.9.: Temporal evolution (a-f) of martensite in 3D with clamped boundary conditions. The colors in the domains show three different orientation variants of martensite. The colors in the boundary represent different crystals. Reprinted from [139] copyright (2012), with permission from Elsevier.

In the following work, it is also demonstrated that 2D and 3D simulations essentially yield the same result provided the effective mobility in the 3D simulations is a factor 0.7 smaller than in the 2D simulations [125].

The first efforts to numerically simulate the evolution of martensitic microstructures were made by Khachaturyan [29] and his co-workers [33, 34, 126, 127]. Numerous contributions in this area have been made, notably by Bhattacharya [128], Saxena and co-workers [129, 130] and Levitas and co-workers [131–134], In spite of these well reported developments which are nicely summarized in the review article of Mamivand et al. [135], phase-field modeling of martensitic microstructures in steel began to be actively discussed only in the last 3-4 years. Recent progresses in this area have been reported in the series of articles of Yeddu, Malik and co-workers [136–146]. (Figure 2.9).

2.1.4. Polymers and liquid crystals

In the area of polymer science, the well known Cahn-Hilliard approach [15] coupled with the fluid flow has been applied to study the influence of external agents [147, 148] and boundary conditions ([149] and references therein) on the characteristics of phase separation. Phase-field approach to model the evolution of spherulites that are formed

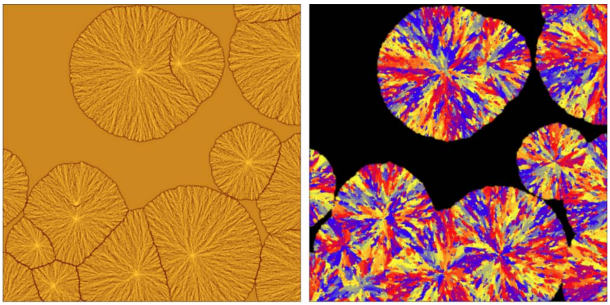

Figure 2.10.: Nucleation and growth of polycrystalline spherulites in the phase-field theory. Left: concentration map, Right: orientation map. Reprinted from [150] copyright (2005), with permission from American Physical Society.

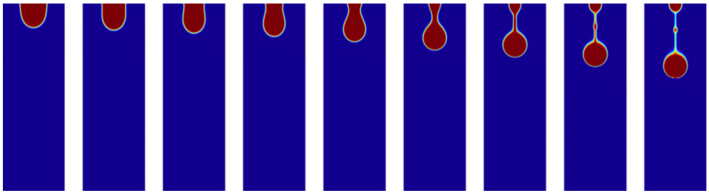

Figure 2.11.: Snapshots of the leaking liquid crystal faucet into a viscous, slightly less dense, fluid, at representative time-steps with Ericksen number and anchoring energy strength equal to 1 and 0 respectively. Reprinted from [153] copyright (2013), with permission from Elsevier.

by quenching liquids into crystalline solids, is described by Gránásy et al. [150] (Figure 2.10).

The molecules of the nematic phase in liquid crystals are locally oriented, resulting in anisotropic viscosity and interfacial energy. Folch et al. [151] develop a phase-field model to study the viscous fingering in nematic liquid crystals. Oates et al. [152] report a phase-field approach to study the evolution of domain structure in nematic phase liquid crystal elastomers. Recently, Yang et al. [153] derive a phase-field model to explore the influence of distortional elasticity and nematic anchoring at the liquid crystal-air interface and how they modify the capillary instability (Figure 2.11). The above developments demonstrate the capability of phase-field method as a valuable alternative to study the non-linear dynamics in liquid crystals, which are otherwise predominately investigated using molecular simulations.

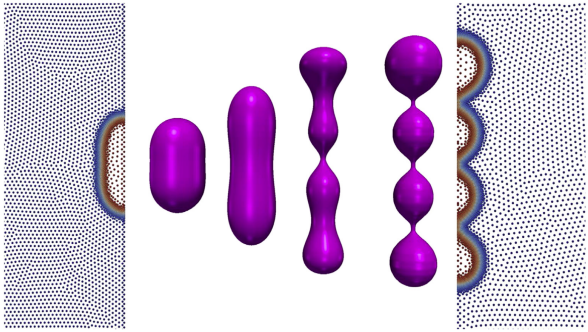

Figure 2.12.: Relaxation dynamics of a constant area vesicle under combined volume decrease and spontaneous curvature increase. Reprinted from [159] copyright (2013), with permission from Elsevier.

2.1.5. Biological applications

In the last few years, there has been a surge in the application of phase-field models to address the problems beyond the realms of typical areas of study, where topological changes at the mesoscale is of primary interest. In the biological arena, the phase-field models have been applied to study the influence of hydrodynamic and mechanical forces on the domain separation in vesicles, such as the red blood cells. The primary objective in this area has been to study the phenomena of microscopic vesicle dynamics. Du et al. [154] compute the equilibrium configurations (volume preserved) of a vesicle membrane under elastic bending energy. Biben et al. [155, 156] extend this work by incorporating hydrodynamic flow. The phase-field studies provide deeper insights into the blood circulation physiology and rheology as the red blood cells have a tendency to tumble if diluted with plasma. Wang and Du [157] and Lowengrub et al. [158] extend the phase-field approach to study the dynamics of multicomponent vesicles. Recently, Peco et al. [159] propose an adaptive–Lagrangian–meshfree technique for phase-field modeling of biomembranes (Figure 2.12).

A tumor is a complex system with a variety of different mechanisms relevant to its growth. The proliferation of solid tumor is essentially a moving boundary problem, where the different constituents in the system organize themselves in different phases. The phase-field models have been used to capture relevant features of the angiogenesis (birth of new blood cells) dynamics which provide insights into the parameters controlling the final capillary network morphology and explain the mechanisms that influence the capillary formation in living organisms [160, 161]. These developments in the numerical approach are summarized in a recent review article by Travasso et al. [162]. It is worth

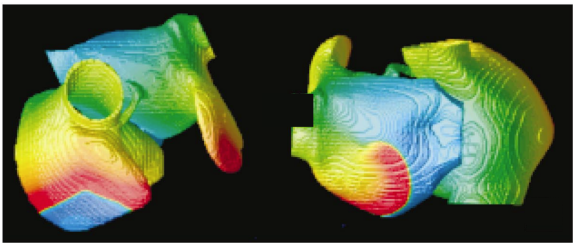

Figure 2.13.: Example simulations of a spiral wave in the anatomical model of the human atria. Reprinted from [164] copyright (2005), with permission from AIP publishing.

noting that in all such phase-field models, the endothelial cells are treated as discrete agents, which implicitly assumes their movement to be driven by chemotaxis (chemical stimulus). Recently, Vilanova et al. [163] develop a new approach, which considers the migration of the tip endothelial cells as a stochastic process and introduces it as a biased circular random walk.

Cardiac arrhythmia (also known as irregular heartbeat) is a group of conditions in which, the electrical activity of the heart is irregular. The numerical modeling of wave propagation in heart geometries has emerged as an exciting discipline. From the modeling perspective, the challenge essentially lies in accurately describing the electro-physiological properties of the heart and a precise implementation of the geometrical structure and fiber orientation within the tissue (networks of cardiac cells). The phase-field approach considers the boundaries between the heart muscle and the surrounding medium as a spatially diffuse interface of finite thickness [164]. The recent studies have focused on elucidating the origin of spatiotemporal patterns of period doubling oscillations of calcium and voltage signals in cardiac cells and tissue which lead to the irregular heartbeat. The review article of Karma [165] summarizes the role of phase-field approach in advancing the understanding of heart rhythm disorders such as ventricular tachycardia and ventricular fibrillation, which are the leading causes of morbidity and mortality in the present era of industrialization.

Finally, the phase-field models have also been applied to explore the morphological transitions associated with defects and deformation [166], electrodeposition of metals [167], colloids [168, 169] and irradiated materials [170].

2.2. Numerical modeling of vein growth

Veins are sub-planar discontinuities in the Earth's crust, containing minerals which precipitate from a super-saturated solution in a fracture [218]. They provide a wealth of information on growth conditions in a fracture which ranges from euhedral growth in open space to elongate-blocky to fibrous growth formed in syntectonic rock microstructures (e.g. [219, 220]) (Figure 2.14).

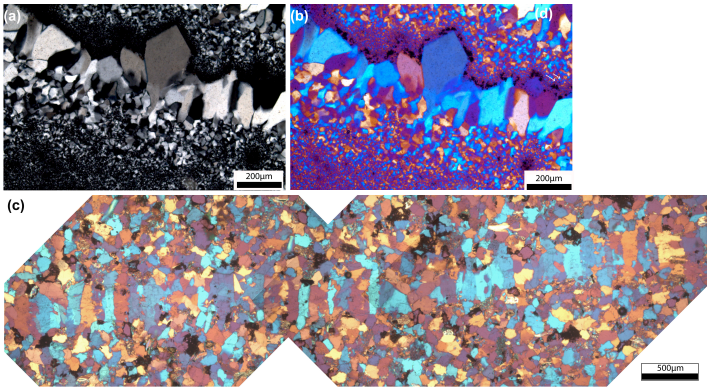

Figure 2.14.: (a) Thin section image of quartz growing upwards from microcrystalline quartz substrate under crossed polarizers. (b) Same image in crossed polarizers and lambda plate. Blue colored crystals indicate NE-SW trending c-axis orientations and yellow colored crystals NW-SE c-axis orientations. Multiple colors on the upper part of the image highlight different crystallographic orientations. During ongoing growth, blue colors prevail. (c) Thin section image of quartz crystals by multiple crack seal increments. Vertically elongated crystals are aligned along a horizontal line. Blue colored crystals indicate N-S trending c-axis orientations and yellow colored crystals W-E orientation. Note that in comparison to (a) and (b), more crystallographic orientations prevail indicated by different birefringence colors of the individual quartz crystals. Image in crossed polarizers and lambda plate.

The elongate and fibrous morphologies are quite different from what is formed if the same mineral grows in an open fluid. These unusual microstructures have been long known. Taber [221] and Mügge [222] explained their formation by proposing crystal growth, which keeps track with syntectonic opening. Often, fracture cements with fluid inclusion bands aligned sub-parallel to the fracture wall suggest that they formed by

repeated fracturing and sealing increments. This crack-seal mechanism [223–226] provides a boundary condition, which suppresses the growth competition and allows growth of elongate crystals. At higher metamorphic conditions, a lens shaped geometry forms due to an irreversible deformation of the host rock and a crack parallel shortening induced by to stress relaxation Nüchter and Stöckhert [227, 228]. These authors thus favored the term cavity sealing. The importance of cements to occlude and stiffen fractures was highlighted in several studies [229–231].

There is an extensive literature describing and analyzing natural vein microstructures (Hilgers and Urai [233, 234], van Noten et al. [235] and many more). Experimental simulation of crystal growth in veins [233, 234, 236–239] has provided a basis for comparison with natural veins in addition to the numerical simulations.

Simulation of unitaxial (one-sided) growth to produce antitaxial veins by Urai et al. [218] shows similarities with natural microstructures and explains the mechanism of curved fibre growth. Subsequent numerical modeling using front-tracking methods [240–242] have explored growth where the crystals can partially seal the crack before the next cracking event, developing facets during the process of partial growth competition. More recent studies using phase field methods [9] have for the first time simulated this process in 3D, showing that the principles developed in 2D simulation essentially hold in 3D.

Bitaxial (from both sides) crack seal growth, where a crack is filled by the same phase as the wall rock (producing quartz veins in quartzite and calcite veins in limestone), is by far the most common vein forming process in the Earth's crust, with unitaxial veins typically composed of calcite in claystones. Therefore, it is surprising that very few simulations of this process have been done to date. This can be partially attributed to the numerical issues experienced on using front-tracking algorithms, for simulating bitaxial sealing.

For a more detailed description of the terminologies pertaining to vein growth, the reader is referred to chapter 3.

Because of this increased complexity, bitaxial vein microstructures can be expected to be more complex than unitaxial. To illustrate some aspects of syntaxial quartz veins in very low grade metamorphic quartzites [226, 235], I present typical microstructures in Figure 2.15. The numerous delocalized microcracks produce veins with many host rock inclusion bands and fluid inclusion trails, and stretched crystal microstructures with frequently jagged grain boundaries (called radiator structures). In some cases, series of isolated grains (in 2D) in trails parallel to the stretched crystals is also present. More details of these microstructures can be obtained by CL imaging which I expect would show numerous healed fractures, and by analysis of fluid inclusions, stable isotopes etc.

2.2.1. Front-tracking models

Cox and Etheridge [171] and Urai et al. [218] propose a kinematic model for crystal growth

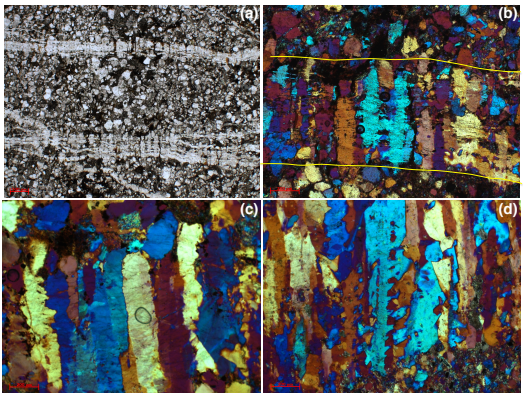

Figure 2.15.: Polarized microscope images of the typical microstructures studied in this thesis, from very low grade metamorphic siltstones of the Variscan of the Ardennes and Eifel (Rursee and Cielle outcrops). (a) overview image showing bundles of crack-seal antitaxial veins in siltstone, with many inclusion bands and stretched crystals in plane polarized light. (b) Stretched crystals with typical radiator morphology and solid inclusion trails, yellow line indicates vein boundary. (c) stretched crystals with smooth boundaries alternating with crystals with irregular boundaries. (d) stretched crystals with irregular boundaries developing into trails of separate grains, at least in thin section. b,c and d are taken with crossed polarizers and the gypsum plate.

in crack seal veins and show the importance of the wall-rock morphology for the resulting vein microstructure. According to this model, if the crystals have already sealed the space available before the next crack event, the facets are lost and they assume the morphology of the rough vein wall interface. If opening increments are sufficiently small, the crystals cannot develop crystal facets and therefore, grow isotropically. An important conclusion of this model is that the crystal growth kinetics is effectively isotropic if the crack surface is sufficiently rough and crack opening rate is smaller as compared to rate of crystal growth front. As a step to implement crystal anisotropy in 2D, an efficient numerical program *Vein Growth* is developed by Bons [240] which is further utilized to simulate the anisotropic growth of crystals under complex boundary conditions. Simulations with *Vein Growth* produce fibrous crystals with the potential to track the opening trajectory of the crack when the wall morphology is rough and the average opening velocity is smaller (Figure 2.17) than the growth velocity of the crystals [172, 237, 241]. A 2D simulation program FACET is separately developed by Zhang and Adams [173] to study the growth of polycrystal based on deposition flux of atoms. Nollet et al. [237] use the algorithms

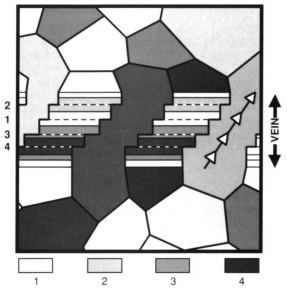

Figure 2.16.: Kinematic simulation of syntaxial crack-seal vein developed by delocalized cracking. Numbers refer to successive crack-seal events, dashed lines mark the sites of each seal and legend shows material added during the corresponding seal event. Reprinted from [218] copyright (1991), with permission from Elsevier.

Vein Growth and FACET to study crystal growth competition leading to orientation selection and transition from blocky to fibrous morphology during crack-seal growth.

The numerical programs *Vein Growth* and FACET suffer from geometric restrictions and are vulnerable to inaccuracies at triple/quadruple crystal junctions. The artifacts of the algorithm *Vein Growth* namely 'Crystal terminations' and 'Long-distance effects' cause the euhedral angles between facets at crystal terminations to depart from an angle corresponding to the equilibrium shape and the effect of non-neighboring crystals on growth process respectively. Further, the method advocates the switching of the numerical program to FACET in order to produce *crystallographically correct* facets that develop during free growth of crystals. However, the switching of numerical program induces new complications; the complete sealing of the crack can no longer be simulated correctly. Besides, the algorithm FACET is not capable of generating the crystal facets from a randomly shaped nucleus and implicitly assumes the presence of *crystallographically correct* facets prior to the growth process. These aspects are addressed in great detail by Nollet et al. [242].

2.2.2. Cellular-automaton-type model (Prism2D)

Lander et al. [231] developed a simulation algorithm (Prism2D) to incorporate the anisotropy in quartz growth kinetics into a calibrated cellular-automaton-type model. The numerical simulations showed how for small wall rock grains, initial overgrowth develop euhedral terminations and the growth competition is controlled by slow-growing crystal facets. When the host rock is coarse grained, initial epitaxial growth until the

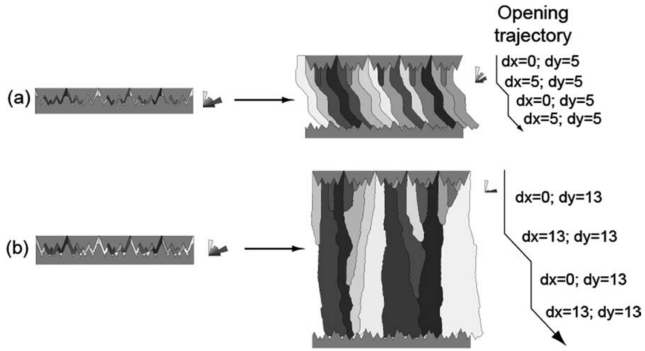

Figure 2.17.: Numerical simulations with oblique opening trajectories in Vein Growth. (a) Oblique opening in small increments (5 pixels lateral offset). (b) Oblique opening in larger increments (13 pixels lateral offset). Fibres track the opening trajectory only when the opening increments are sufficiently small. Reprinted from [237] copyright (2005), with permission from Elsevier.

formation of euhedral facets is more important. Such results are currently implemented into novel reservoir quality prediction codes for porous siliciclastic reservoir rocks [174]. This model was also used to numerically simulate dolomite growth within dolostone fractures [175]. Recently, Lander and Laubach [176] investigated the influence of quartz growth and crack opening rates on the evolving vein morphologies such as bridges, rinds and massively sealed structures. The results compare quite well with the microstructures in partially sealed quartz veins with bridges, as shown by CL microscopy, and also compare favorably with earlier simulations of stretched and elongate blocky textures in quartz veins reported by Urai et al. [218] and Bons et al. [220].

2.2.3. Diffuse interface model

Despite the above achievements of the front-tracking as well as cellular-automaton-type models, their applications have been limited to 2D. In the present context, I emphasize that the curvature of grain boundaries as well as the grain-liquid surfaces is an important factor which governs the morphological evolution of crystal growth patterns in veins. Since these curvatures are different in 3D as compared to 2D, the underlying physics of this complex evolution can be interpreted in a physically sufficient manner by methods capable of capturing the growth characteristics and dynamics in full 3D space. Moreover, it is also important to account for a statistically higher number of grains to establish the relevance of the simulated results. Therefore, the present numerical techniques need to

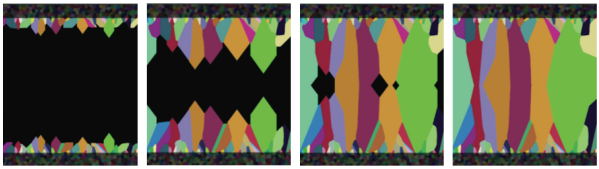

Figure 2.18.: Temporal evolution of metamorphic vein textures that use the same host rock properties and initial fracture position. “Elongate blocky” vein texture develops in this opening- mode fracture by the passive growth of quartz into the fracture void. Reprinted from [176] copyright (2014), with permission from the Geological Society of America.

be extended to 3D for a meaningful comparison with experimental data. However, such an extension, all though desirable, turns out to be a nontrivial task, as the computational requirements needed to carry out the numerical simulations increase dramatically with the number of spatial dimensions. The phase-field method, long established in the material science community, is a stand-out approach to describe microstructural evolution during phase transitions for e.g. solidification, spinodal decomposition etc. [30, 82, 86, 88] The phase-field method's popularity in modeling material processes is due to the elegance with which it treats moving boundary problems by obviating the necessity to explicitly track the interfaces. Thus it can overcome many of the problems suffered by earlier models such as the *Vein Growth* and FACET. The model equations are derived on the basis of general thermodynamic and kinetic principles and contain a number of phenomenological parameters related to the physical properties of the material. These parameters are determined based on experimental and theoretical information. Different thermodynamic driving forces for microstructure evolution, such as chemical bulk free energy, interfacial energy, elastic strain energy and different transport processes, such as mass diffusion and advection, can be coupled and the effect on the over all evolution process can be studied simultaneously.

Hubert et al. [178] introduce a phase-field model to study sealing in fractures, which uses a non-faceted anisotropy for the interfacial energy. However, such smooth continuous functions have two limitations, if utilized to simulate the evolution of crystals with flat facets and sharp corners [179]. First, sharp corners that arise due to missing orientations in the equilibrium shape are related to the non-convexity of the parametric inverse interfacial energy plot. This leads to ill-posed phase-field equations for these orientations, which have to be regularized [180]. The second problem is that ideal straight facets require sharp cusp-like minima in the interfacial energy. The non-differentiability at cusps result in undefined equilibrium and motion equations, for interfaces having the orientation of a facet. Eggleston et al. [180], Fleck et al. [181] and Selzer [182] present a computationally efficient implementation of the phase-field models that account for arbitrary crystal symmetries with curved facets and high angle rotations of crystalline

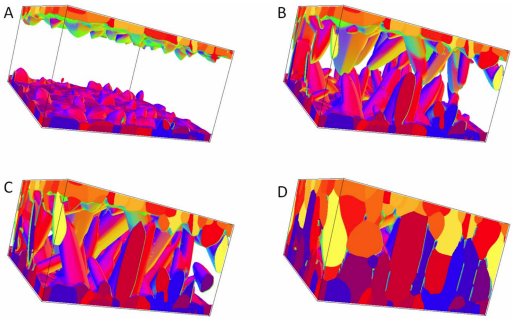

Figure 2.19.: (a-d) 3D phase-field simulation of fracture sealing (quartz surface in fracture rendered according to surface normal). Reprinted from [183] copyright (2015), with permission from John Wiley and sons.

axes. Ankit et al. [9, 10] show the importance of adopting a general thermodynamically consistent approach in modeling the evolution of fracture cement microstructures by considering faceted-type anisotropy formulations of the interfacial energy function to simulate crystals with flat facets and sharp corners. Wendler et al. [183] present phase field simulations of the epitaxial growth of quartz in hydrothermal veins (Figure **??**), in a study of one-step sealing (without crack-seal), comparing their results with those of hydrothermal experiments.

Part II.

Research objectives and methods

3. Objectives of this work

Scientific objectives presented in this chapter are published in parts in [5–11].

The present thesis serve dual objectives:

1. Investigation of the pattern formation processes by assuming isotropic interfacial energy. In order to achieve this objective, eutectoid transformation in Fe-C steels is considered as an example. The overall idea is to demonstrate the richness in microstructural pattern formation in steels, even if the anisotropy in interfacial energy is not considered.
2. Investigation of the pattern formation processes by assuming faceted (strong) anisotropy in the interfacial energy. The process of polycrystalline evolution in geological veins is considered as an exemplar. In particular, the objective is to decompose the influence of various boundary conditions on vein textures. Two distinct minerals, namely alum and quartz are considered in order to gain insights into the natural pattern formation in rocky veins.

3.1. Pattern formation during eutectoid transformation in Fe-C steels

3.1.1. Cooperative growth: Pearlite

The mechanisms of microstructural evolution during eutectoid transformation in steel has been a topic of theoretical as well as experimental investigation since inception of steel as a structural material. The eutectoid transformation involves the formation of a pearlite colony which appears as alternate lamellae of ferrite and cementite phases, that grow as a common front with the austenite. Cementite is the carbon rich phase whereas the carbon solubility in ferrite is relatively quite low [184–186].

The two principal mechanisms of eutectoid reaction, i.e. austenite to pearlite phase transformation, cited in the literature are volume diffusion and grain boundary diffusion. The former suggests the volume diffusion of carbon ahead of the phase interface, while the latter emphasizes the role of grain boundary diffusion as the rate controlling step. The pioneering work of Zener [187], Hillert [96] and Tiller [188] on pearlite formation explains the relation between the lamellar spacing and undercooling during the phase transformation. In spite of making a generous effort to explain the phenomenology

of pearlitic transformation, the classical Zener-Hillert model shows large deviations from the experimentally measured lamellar growth velocities. The model assumes no diffusion in the ferrite phase whilst considering diffusion in austenite phase (only). This would be a reasonable assumption in case of eutectic solidification problem, where the diffusivity in solid is lower than the diffusivity in liquid (bulk phase) by a factor of 1000. However, in a solid state phase transformation like the eutectoid reaction, the diffusivity in austenite (bulk phase) is comparable to the ferrite. Thus, it is reasonable to expect some disagreement of experimental velocities with corresponding values derived from the Zener-Hillert co-operative growth model.

Jackson and Hunt [4] adapt the Zener-Hillert model for investigating directional solidification in eutectics with a constant velocity of growth front, which broadly falls in the same class of moving boundary problem as the eutectoid transformation. Recently, Nakajima et. al [94] use the multi phase-field method to simulate the co-operative pearlite growth by accounting for diffusion in the ferrite as well as the austenite phase. They predict a successive process of diffusion in ferrite and growth of cementite from the ferrite, resulting in an increase of the kinetics of pearlitic transformation by a factor of four as compared to growth from austenite exclusively. The simulated cementite lamella is found to be tapered and exhibits a conical morphology. This is interpreted as an effect of diffusion in ferrite. Steinbach and Plapp [189] claim an overlap of phase-field results with Hillert's model in absence of diffusion in ferrite. Further, they couple a stress-driven diffusion field to the phase field and study the effect of transformation strains. However, Pandit and Bhadeshia [98] argue that pearlite forms by reconstructive transformation, in which case, transformation strains should not be significant. They also emphasize the need to consider both the mechanisms, volume as well as interfacial diffusion, simultaneously for an overlap with experimental findings.

In chapter 5, I extend the previous work on Jackson-Hunt (JH) analysis of ternary eutectic alloys [205] to study the eutectoid transformation. The main question which I address is: Can a JH type analysis (previously done for eutectics) be extended to predict lamellar growth velocities of pearlite by accounting for diffusion in austenite as well as ferrite? In order to answer this question, I first extend the JH analysis for eutectics by accounting for diffusion in austenite as well as ferrite. Then I analyze the case of stable lamellar coupled growth and derive the expressions for lamellar growth velocity as a function of undercooling and lamellar spacing. This is followed by comparison of analytical prediction with the numerical results of a thermodynamically consistent phase-field model.

3.1.2. Non-cooperative growth: Divorced eutectoid

The eutectoid transformation in steel involves the decomposition of the parent austenite (γ) into two product phases, ferrite (α-Fe) and cementite (θ-Fe_3C). When both the product phases, evolve cooperatively, sharing a common growth front with austenite, the morphology of the resulting product is lamellar, popularly known as pearlite [5, 96, 184,

187]. On the contrary, under a given set of conditions (low undercooling and small inter-particle spacing of pre-existing cementite), the α/γ advancing transformation front begins to pull-away from cementite, leading to the formation of a divorced eutectoid. Hillert et al. [184] establish that a pearlitic colony comprises of inter-penetrating bi-crystals of ferrite and cementite phases. Steels with a fully pearlitic microstructure (0.8 wt.% C), find extensive application in the manufacture of ropes, where high tensile strength is desirable.

Manufacture of a significant proportion of engineering components, obligate the use of steels with low hardness and good machinability (for e.g. in ball-bearings [190]). Two, well-known spheroidizing annealing heat treatment cycles, that are adopted to soften the pearlite, prior to machining, are shown in Figure 3.1. The sub-critical annealing involve the spheroidization of the fine pearlite, by holding the hypoeutectoid steel isothermally, just below the A_1 temperature, as shown in Figure 3.1(a). The driving force for morphological transition is the reduction in θ/α interfacial area. For softening hypereutectoid steels, intercritical annealing [Figure 3.1(b)] is a more economical method (see [190] and references therein). The steel is fully austenised, such that a small amount of cementite particles remain undissolved, and then held below A_1 to generate a spheroidized transformation product (cementite particles embedded in ferritic phase), popularly known as *divorced eutectoid microstructure*, which is much softer than the lamellar counterpart i.e. pearlite [Figure 3.2(a)]. Experimental studies indicate that the presence of pre-existing cementite particles in the parent austenitic matrix results in the non-cooperation between the ferrite and cementite phases [191–193] and yields divorced eutectoid as the final transformation product [Figure 3.2(b)].

The history of divorced eutectoid dates back to the time of Honda and Saito [195], who report the morphological dependence of the final-transformed product (lamellar to completely spheroidized) on the austenising temperature. Oyama et al. [191] describe a heat treatment schedule, that is adopted for spheroidizing a microstructure, comprising of a mixture of pearlite and proeutectoid cementite. Verhoeven and Gibson [196] develop a theoretical framework (for binary Fe-C alloy) to establish the criteria, that governs the transition from lamellar to divorced eutectoid morphology. Luzginova et. al [197] study the influence of chromium concentration on the formation of divorced pearlite in a hypereutectoid steel. Pandit and Bhadeshia [99] amend the earlier theory of lamellar to divorced eutectoid transition, by accounting for the diffusion of carbon along the transformation front.

It is apparent from the brief literature survey, that much of the investigation of divorced eutectoid transformation is primarily limited to experimental and theoretical studies. They delineate the basic concept of the evolution mechanism, but unable to provide the finer details required for tailoring the microstructure to achieve the desired properties (e.g. better machinability). Therefore, a theoretical understanding of the complex evolution pathways during the divorced eutectoid transformation is paramount to comprehend the final microstructure, which is indispensable from a technological point of view.

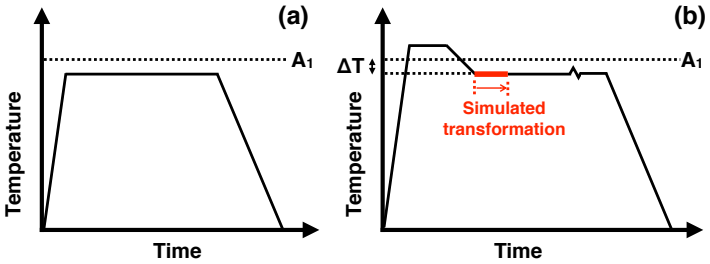

Figure 3.1.: Typical spheroidizing annealing heat treatment cycles [194]. (a) Sub-critical annealing is carried out slightly below the A_1 temperature and does not involve the formation of austenite. (b) Inter-critical annealing involves heating the hypereutectoid steel to fully austenise it, with a small amount of cementite remaining undissolved and then, holding it just below A_1 temperature. The final transformation product is known as the divorced eutectoid. The divorced eutectoid transformation, that is numerically simulated in the present work (for three different undercoolings, ΔT), is shown by the colored (thick) line.

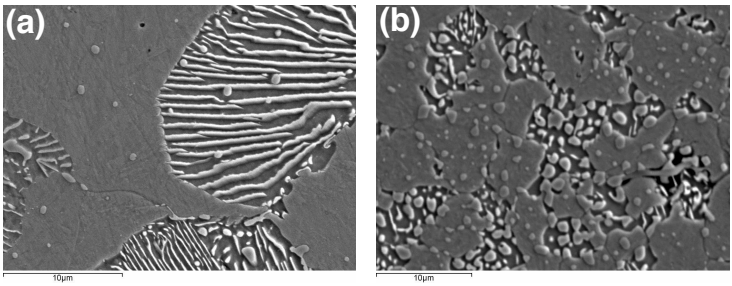

Figure 3.2.: Cooperative and non-cooperative growth regimes are observed during eutectoid transformation in Fe-0.92C-0.66Si-1.58Mn-1.58Cr-0.12Ni-0.05Mo-0.178Cu (wt. %) alloy. Samples are austenised at 870 °C for 2.5 hours and held for $\sim$ 65 minutes below the eutectoid temperature (at T_1 and T_2). These are finally quenched to ambient temperature. (a) Lamellar and (b) divorced eutectoid morphologies are obtained for $T_1 = 710\,°C$ and $T_2 = 705\,°C$, respectively (private communication with Z.X. Yin and H.K.D.H. Bhadeshia).

In view of establishing a synergy between theoretical and experimental studies concerning the eutectoid transformation, the phase-field method holds great promise in terms of the ability to describe the interface evolution in the diffusion length scale. In chapter 6, I use

a multiphase-field model (explained in chapter 4) to scrutinize (and amend) the existing theory by providing an in-depth understanding of the carbon redistribution mechanism, which has profound implications in eventual optimization of the process control parameters related to heat treatment of steel. Based on the insights from numerical simulations, my further intention is to depict the interplay between two important parameters – (a) spacing between the pre-existing cementite particles and (b) undercooling, which can result in different eutectoid morphologies.

The theoretical basis reported earlier [99, 196] as well as the numerical results in chapter 6 are primarily limited to the case of symmetric arrangement of preexisting θ particles, (Figure 3.3(a)). In this regard, a typical approach has been to generalize the transformation mechanism on the basis of simplified theories (limited to symmetric configuration, as shown in Figure 3.3(a)) and thereby, elucidate the complex carbon redistribution pathways in the experimental microstructures, where the transformation proceeds from a preexisting random arrangement of θ particles, as shown in Figure 3.3(b). It is worth mentioning that the influence of curvature-driven coarsening is more pronounced, as the transformation proceeds from a random spatial arrangement of θ particles. In the present article, I aim to bridge this gap in understanding by reporting a detailed parametric study of the non-cooperative eutectoid transformation, which proceeds from random arrangement of preexisting θ particles.

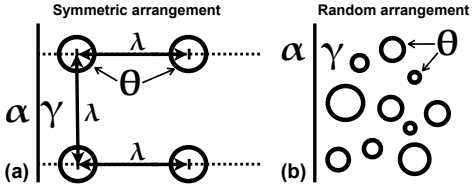

Figure 3.3.: Schematic diagrams showing the arrangement of preexisting cementite (θ) particles. (a) Particles are in symmetric position – arranged in rows parallel to the α/γ growth front. The centers of the particles in two consecutive rows lie on a straight line (dashed line) perpendicular to the growth front and maintain the same interparticle spacing λ (for more than two rows of particles). (b) Particles are in random position – the centers of the particles do not necessarily lie on straight lines perpendicular to the growth front and the interparticle spacings are variable.

In chapter 7, I analyze the influence of coarsening by introducing a third preexisting θ particle at a symmetric position (refer to Figure 3.3(a)). Changes in carbon redistribution mechanism, which arise due to introduction of the new particle is of particular interest. Next, I relax the assumption of a preexisting symmetric arrangement and study microstructural evolution characteristics as the transformation proceeds from a random distribution of θ particles. Due to overlapping concentration fields of the preexisting par-

ticles, which essentially depends on their relative arrangement, a competition between the various carbon redistribution mechanisms is anticipated, as the α/γ transformation front temporally evolves. Various theories have been proposed in the past to explain the occurrence of a bimodal θ size distribution in the transformed microstructure [197, 213, 214]. In view of interesting experimental findings, I numerically simulate and analyze the complex microstructural evolution starting from different preexisting arrangements of θ particles at various undercoolings and thereby, propose a general mechanism which result in a bimodal (or multimodal) distribution of θ particles.

In the final chapter of Part III (chapter 8), I study how the preexisting spatial arrangement of θ particles influences the evolution of α/γ transformation front (non-cooperative or otherwise). To begin with, I analyze the coarsening regime in detail, starting from an asymmetric configuration of preexisting θ particles. Next, I investigate the influence of prior γ grain boundaries and morphology of preexisting α layers on the temporal evolution of divorced eutectoid microstructure. Finally, by qualitatively comparing the simulated θ morphologies with those observed in experimental microstructure, I deduce the mechanisms by which mixed morphologies (spheroidal as well as non-spheroidal) evolve.

3.2. Pattern formation in geological veins

The evolution of veins is of importance in many fields of applied and basic earth science, because of the associated large changes in transport properties and rock strength. A range of microscale processes have been identified, which depend on parameters such as the degree of supersaturation, rates of transport by diffusion and advection, epitaxial and anisotropic crystal growth, local rates of deformation, and the relative strengths of the wall rocks and vein minerals [232]. Therefore, it is not surprising that the process of vein formation in deformed rocks is complex.

Growth of crack-seal veins can take place in two different kinematics. In unitaxial veins, epitaxial crystal growth takes place on the vein fill only, towards the wall rock, and thus on only one side of the crack. In bitaxial veins, crystals grow on the wall rock or fractured vein material, on both sides of the crack. Which of the two mechanisms will operate depends mainly on material contrast between wall rock and vein material. This determines the local mechanical properties and thus, the site of renewed cracking, together with the locations of epitaxial growth sites. These two fundamental types, combined with localized or delocalized cracking, and different rates of anisotropic crystal growth versus opening rate, produce a wide range of microstructures called fibrous, elongate-blocky, stretched crystal, ataxial, etc.

One essential aspect of the repetitive crack-seal process is that after each cracking event, the crystal surfaces developed are rough, grow isotropically until facets form, continue to grow until the crack is sealed and a new rough surface is produced by the next cracking

event. The difference between unitaxial and bitaxial growth is that in the first case, the template against which, the crystals grow is invariant, and in the second case, it evolves.

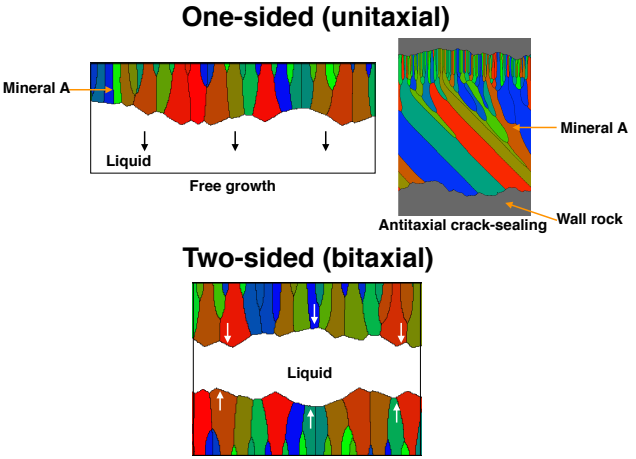

Figure 3.4.: Diagram illustrating free growth, antitaxial and bitaxial crack-sealing in veins.

3.2.1. Free growth in open cavity

In chapter 9, I use a thermodynamically consistent multiphase-field model (described in chapter 4) to extend the 2D numerical studies of vein growth to 3D. Here, I present the specific formulation of the multiphase-field model for alum and quartz growth by considering anisotropy of the surface energy to produce flat facets and sharp corners. I also briefly discuss about the computational optimization technique used to make large-scale studies feasible in the present simulations. The phase-field model is used to simulate and analyze the kinematic properties of the anisotropic growth competition in polycrystal, arising due to mis-orientation with respect to most preferred growth direction. In this regard, I also make a strict check for any model artifacts (if present).

3.2.2. Unitaxial veins

When minerals grow from only one side into a dilatation site, it is usually referred to as unitaxial growth (as shown in Figure 3.4). In chapter 10, I modify the boundary condition

and parameters (used for free growth) to present a systematic study of the influence of crack surface roughness, crack opening velocity, opening trajectory and number of crystal nuclei on unitaxial sealing. This is followed by a detailed analysis of the 3D tracking efficiency and wall surface pinning in chapter 11. It expands the discussion presented in the previous chapter and considers natural fractured rocks as an example. By employing advanced visualization and innovative post-processing techniques, new methodologies to calculate the general tracking efficiency for a more complex motion of grain boundaries is proposed. The present work highlights the importance of accounting the time evolution rather than calculating tracking efficiency solely based on final grain boundary morphology. Further, grain statistics such as temporal evolution of the number of tracking grain boundaries and the corresponding orientation and size distribution is obtained from the present large scale 3D phase-field simulations with an aim to relate the shift in growth mechanism as a function of crack-opening rate, which is missing in chapter 10.

3.2.3. Bitaxial veins

When minerals grow from both the sides into a dilatation site, it is usually referred to as bitaxial sealing (as shown in Figure 3.4). In chapter 12, I validate the model (described in chapter 4) by examining the curvature of grain boundaries that evolve during the bitaxial sealing of two grains. Next, I present a systematic study to explore the effects of changing the crack-opening vector and location of the crack, on the vein texture and grain statistics. Then, I numerically simulate and analyze the mechanism by which the associated crystal fragments evolve. Finally, I present a discussion of numerical results and compare them with natural examples. Considering the large and complicated parameter space, this study, which complements that of Lander and Laubach [176], is only a first look with a discussion on the directions of further parameter studies.

4. Methods

Description of the phase-field models in this chapter are published in parts in [5–11].

4.1. A phase-field model for polycrystalline evolution

In this section, I present and adapt a multiphase-field model capable to treat the problem of polycrystalline growth of crystals of distinct growth shape. The general model and a short sketch of the numerical methods used to treat a multi-phase/multi-grain problem in veins is given below. This is followed by a bench-marking of the anisotropic growth of alum and quartz, by numerically simulating and analyzing equilibrium geometries. Key modeling assumptions are also enumerated.

4.1.1. Multiphase-field model

A set of phase-field parameters denoted by $\boldsymbol{\phi}(\vec{x},t) = (\phi_1(\vec{x},t) \cdots \phi_N(\vec{x},t))$ are considered, where each component of the vector $\phi_\alpha(\vec{x},t)$ varies smoothly from 1 inside 0 outside the crystal α over a small finite distance ε (diffuse interface). The location of the crystal-liquid or crystal-crystal interface is defined by a level set at $\phi_\alpha(\vec{x},t) = 0.5$ which is determined mathematically by solving the evolution equation. The external fields like temperature or concentration can be coupled to the phase-field parameter $\boldsymbol{\phi}$, hence no external boundary conditions needs to be applied at the interfaces.

For vein growth simulations, I use the phase-field equations derived from non-equilibrium thermodynamics guaranteeing a locally positive entropy production. The model is well suited to describe a polycrystalline system by accounting for an arbitrary number of phase-field parameters [1]. In the considered applications to crystal growth in veins, I restrict model definition to an isothermal problem. The Helmholtz free energy functional can be formulated as

$$\mathcal{F}(\boldsymbol{\phi}) = \int_\Omega \left(f(\boldsymbol{\phi}) + \varepsilon a(\boldsymbol{\phi}, \nabla\boldsymbol{\phi}) + \frac{1}{\varepsilon} w(\boldsymbol{\phi}) \right) dx, \tag{4.1}$$

where $f(\boldsymbol{\phi})$ is the bulk free energy density, ε is the small length scale parameter related to the interface width, $a(\boldsymbol{\phi}, \nabla\boldsymbol{\phi})$ is a gradient type and $w(\boldsymbol{\phi})$, a potential type energy density. Each of these terms are discussed in detail below.

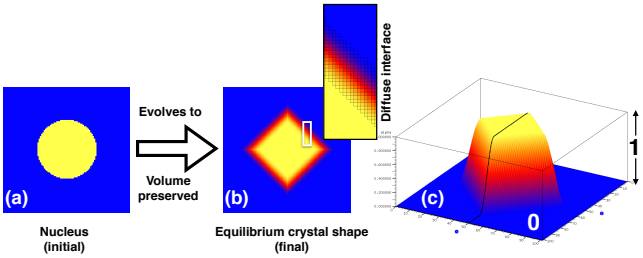

Figure 4.1.: Diffuse interface approach: The phase-field variable evolves continuously (smooth transition) from one phase to another. (a) An initial crystal nucleus embedded in liquid, evolves to (b) the equilibrium shape, whilst maintaining a numerically constant volume. The distinct number of grid-points, which constitute the simulated solid-liquid interface is shown in the inlet picture. (c) Contour plot showing the smooth transition of the phase-field variable along the simulated solid-liquid interface (numerically equals to 0 in liquid and 1 in solid).

The phase-field parameter $\boldsymbol{\phi}(\vec{x},t) = (\phi_1(\vec{x},t) \cdots \phi_N(\vec{x},t))$ describes the location of 'N' crystals with different orientation. The value of each phase field parameter ϕ_α lies in the interval $[0,1]$ and fulfills the constraint $\sum_{\alpha=1}^{N} \phi_\alpha = 1$. The interfaces between the different domains (represented by phase-field parameter) are identified by a continuous variation of the properties within a narrow region (Figure 4.1), in contrast to the front-tracking approach for microstructure modeling. The integral shown in functional (4.1) extends over the entire domain of consideration.

The gradient energy density $a(\boldsymbol{\phi}, \nabla\boldsymbol{\phi})$ is given by

$$a(\boldsymbol{\phi}, \nabla\boldsymbol{\phi}) = \sum_{\substack{\alpha,\beta=1 \\ (\alpha<\beta)}}^{N,N} \gamma_{\alpha\beta} a_{\alpha\beta}^2(\boldsymbol{\phi}, \nabla\boldsymbol{\phi}) |\vec{q}_{\alpha\beta}|^2 \tag{4.2}$$

where $a_{\alpha\beta}(\boldsymbol{\phi}, \nabla\boldsymbol{\phi})$ defines the form of the surface energy anisotropy of the evolving phase boundary and $\gamma_{\alpha\beta}$ is the surface free energy per unit area of the $\alpha-\beta$ boundary which may additionally depend on the relative orientation of the interface. The vector quantity $\vec{q}_{\alpha\beta} = \phi_\alpha \nabla\phi_\beta - \phi_\beta \nabla\phi_\alpha$ is a generalized gradient vector normal to the $\alpha-\beta$ interface. To assign an isotropic surface energy to the $\alpha-\beta$ phase boundary, $a_{\alpha\beta} = 1$ is chosen. For including a strongly anisotropic surface energy, so that crystals develop flat facets and sharp corners according to directions of the crystal symmetry, a piece-wise defined

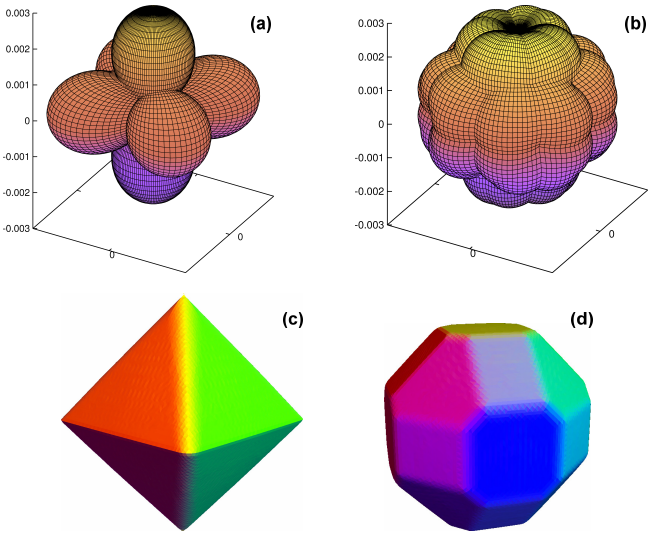

Figure 4.2.: Polar plot of function (4.3) for (a) cubic and (b) alum (truncated octahedral symmetry). These anisotropic functions are incorporated in phase-field model to simulate the equilibrium crystal shapes for (c) an octahedral crystal and (d) an alum in free growth conditions. The colors in Figures 4.2(c) and 4.2(d) differentiate among crystal facets.

function is used

$$a_{\alpha\beta}\left(\boldsymbol{\phi}, \nabla\boldsymbol{\phi}\right) = \max_{1\leq k\leq \eta_{\alpha\beta}} \left\{ \frac{\vec{q}_{\alpha\beta}}{|\vec{q}_{\alpha\beta}|} \cdot \vec{\eta_{k,\alpha\beta}} \right\} \tag{4.3}$$

where $\{\vec{\eta}_{k,\alpha\beta} | k = 1, \cdots, \eta_{\alpha\beta}\}$ for $\eta_{\alpha\beta} \in M$ denotes the complete set of vertex vectors of the corresponding Wulff shape of a crystal α embedded in the bulk phase β and M represents the number of edges. In Figures 4.2(a) and 4.2(b), a polar plot of function (4.3) for a cubic symmetry and for a truncated octahedral shape are shown[1]. The corresponding equilibrium crystal shapes are displayed in Figures 4.2(c) and 4.2(d), respectively.

In the free energy functional (4.1), the function $w\left(\boldsymbol{\phi}\right)$, which represents a multi-obstacle

[1]The Gnuplot script to generate the cubic symmetry and the corresponding surface energy plot was provided by M.S. This was extended by K.A. to generate the Wulff shape of alum and the associated surface energies.

potential is chosen of the form

$$w(\boldsymbol{\phi}) = \begin{cases} \dfrac{16}{\pi^2} \sum\limits_{\substack{\alpha,\beta=1 \\ (\alpha<\beta)}}^{N,N} \gamma_{\alpha\beta}\phi_\alpha\phi_\beta + \sum\limits_{\substack{\alpha,\beta,\delta=1 \\ (\alpha<\beta<\delta)}}^{N,N,N} \gamma_{\alpha\beta\delta}\phi_\alpha\phi_\beta\phi_\delta & \text{if} \quad \boldsymbol{\phi} \in \sum \\ \infty & \text{elsewhere,} \end{cases} \tag{4.4}$$

where $\sum = \left\{ \boldsymbol{\phi} \mid \sum_{\alpha=1}^{N} \phi_\alpha = 1 \text{ and } \phi_\alpha \geq 0 \right\}$. The higher order term proportional to $\phi_\alpha\phi_\beta\phi_\delta$ in function (4.4) is added to reduce the presence of an unwanted third or higher-order phase at binary interfaces.

The term $f(\boldsymbol{\phi})$ represents the interface driving force due to the occurrence of different bulk phases. A general formulation of $f(\boldsymbol{\phi})$ can be given as an interpolation of different free energy densities f_α of the bulk phases,

$$f(\boldsymbol{\phi}) = \sum_\alpha f_\alpha h(\phi_\alpha) \tag{4.5}$$

For studying the kinematics of crystal growth, a suitable interpolation function $h(\phi_\alpha) = \phi_\alpha^3 \left(6\phi_\alpha^2 - 15\phi_\alpha + 10\right)$ and a constant value for f_α for the bulk free energies are chosen.

The evolution equations for the phase fields can be derived from the free energy functional (4.1) by relating the temporal change of the order parameter, i.e. $\dfrac{\partial\phi_\alpha}{\partial t}$ to the variational derivative of the functional $\mathcal{F}$. Applying the Euler Lagrange formalism yields:

$$\tau\varepsilon\frac{\partial\phi_\alpha}{\partial t} = \varepsilon\left(\nabla \cdot a_{,\nabla\phi_\alpha}(\boldsymbol{\phi}, \nabla\boldsymbol{\phi}) - a_{,\phi_\alpha}(\boldsymbol{\phi}, \nabla\boldsymbol{\phi})\right) - \frac{1}{\varepsilon} w_{,\phi_\alpha}(\boldsymbol{\phi}) - f_{,\phi_\alpha}(\boldsymbol{\phi}) - \lambda, \tag{4.6}$$

$$\lambda = \frac{1}{N}\sum_\alpha \varepsilon\left(\nabla \cdot a_{,\nabla\phi_\alpha}(\boldsymbol{\phi}, \nabla\boldsymbol{\phi}) - a_{,\phi_\alpha}(\boldsymbol{\phi}, \nabla\boldsymbol{\phi})\right) - \frac{1}{\varepsilon} w_{,\phi_\alpha}(\boldsymbol{\phi}) - f_{,\phi_\alpha}(\boldsymbol{\phi}), \tag{4.7}$$

where the comma separated subindices represent derivatives with respect to ϕ_α and gradient components $\dfrac{\partial\phi_\alpha}{\partial\chi_i}$. The Lagrange multiplier λ guarantees the summation constraint $\left(\sum\limits_{\alpha=1}^{N} \phi_\alpha = 1\right)$. In the evolution equation (4.6), τ is the kinetic coefficient which establishes a relationship between the interface growth velocity and the driving force.

The phase-field evolution equation (4.6) is solved numerically using an explicit forward Euler scheme. The spatial derivatives of the right hand side equation are discretized

using a second order accurate scheme with a combination of forward and backward finite differences. The phase-field solver is written in programming language C and only solves the evolution equation next to the locally present interfaces. The implementation of such a locally reduced order parameter optimization (LROP) facilitates a reduction in computation time from $O(N^3)$ to $O(1)$ and in memory consumption from $O(N)$ to $O(1)$ per cell in the domain, N being the number of crystals in the system[2]. Thus, the computation is independent of the number of phases making the large scale crystal growth studies feasible even in 3D [243, 244]. Further, the simulation code is 3D parallelized on the basis of message passing interface (MPI) standard including 3D domain decomposition and dynamic redistribution schemes. For the present article, the simulations are performed on multiprocessor workstations as well as on a Linux high performance cluster

4.1.2. Modeling equilibrium quartz geometry

Quartz occurs in different forms and the relative size of the facets vary as per the growth conditions. For the sake of simplicity at this stage of modeling, one can choose a common quartz geometry containing the facets, $(10\bar{1}0)$, $(10\bar{1}1)$ and $(01\bar{1}1)$. The surface energy is proportional to the distance of the facet from the geometrical center. The tables in Appendix A show the vertices of the chosen quartz geometry (Figure A1) and the corresponding surface energies of the facets (Table A1) .

A two-dimensional representation is derived from the three-dimensional geometry by considering two possibilities: symmetric and asymmetric as shown in Figure 4.3. If the vertices pertaining to the symmetric case are projected on a plane, a symmetric 2D variant is derived. On the contrary, projection of the vertices that correspond to the asymmetric case, lead to two identical asymmetric 2D geometries, which can be classified as (a) left-handed and (b) right-handed quartz. Lander et al. [231] and Lander and Laubach [176] also use a similar growth form of quartz to derive 2D symmetric variants (only) for their simulations. However, it is necessary to consider the effect of intrinsic handedness of the quartz symmetry as the *most-preferred-orientation* for asymmetric variants is somewhat tilted from the usual c-axis of the symmetric variant and ultimately result in a different microstructure, as they evolve freely. With a motive to highlight the influence of handedness on the freely evolving quartz veins, I use an asymmetric variant for the present 2D simulations.

In order to simulate the precise equilibrium shape of a single quartz crystal growing in liquid, we adopt the volume preservation approach, proposed earlier by Nestler et al. [246]. The polar-plot of the interfacial energy and the corresponding equilibrium crystal shape are shown in Figures 4.4(a) and 4.4(b), respectively.

[2]This statement written by K.A. is based on a discussion with M.R.

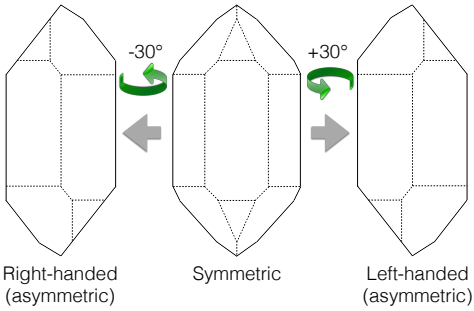

Figure 4.3.: Schematic diagram to demonstrate the method of obtaining 2D variants from the 3D quartz geometry. The solid lines represent the projections of the edges of 3D quartz geometry on a plane. For the present numerical simulations, the asymmetric variants are preferred over symmetric, due to handedness. The illustrated geometry is an adaptation of form number 10 available at the open-source crystal atlas [245].

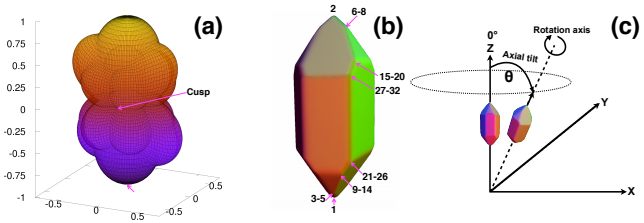

Figure 4.4.: (a) Polar plot of the interfacial energy for the symmetry of a quartz crystal. (b) Equilibrium quartz shape obtained from phase-field simulation. The complete set of vectors corresponding to the labeled vertices are presented in Table A1. (c) The definition of crystal orientation in 3D. The radius of the horizontal circle gives a measure of the misorientation with respect to the *most preferred orientation* of the crystallographic c-axis (which is along Z axis for 3D quartz). Apparently, a concentric circle with a larger radius refers to a larger axial tilt (or larger misorientation) and vice versa. The colors in figure 4.4(b) and 4.4(c) is an illumination effect to differentiate among crystal facets and should not be confused with the color coding used to represent crystal misorientation in the polycrystalline growth.

4.1.3. Assumptions

In this section, I list the assumptions of the modeling and briefly discuss their relevance in the vein growth process.

- Precipitation is the rate limiting step in the vein growth process. Thus, the attachment kinetics of the solute on the evolving crystal/liquid surface is much slower than transport to the precipitation site through the hydrothermal solution. Therefore, the supersaturation of the liquid is constant.

- The evolution of crystal in veins occurs by an interplay of surface energy anisotropy and growth kinetics. Typically, a crystal nucleates in its equilibrium (Wulff) shape, and evolves towards the corresponding 'kinetic Wulff shape'. In the present work, I assume that crystal facets develop due to strong (faceted) anisotropy of the surface energy (see Equation 4.3), whereas, the growth kinetics are isotropic. The anisotropy in growth kinetics can be accounted for in the present model by using a piece-wise function, similar to Equation 4.3 for the kinetic coefficient τ (in Equation 4.6). However, in absence of any reliable data on kinetic Wulff shape of quartz, which can be used to validate the numerical simulations of kinetically controlled growth shape of quartz geometry, the present assumption seems to be reasonable.

- The present study deals with the precipitation of quartz in veins at a temperature (very low grade metamorphism) which is significantly lower than the recrystallization temperature (lower greenschist facies). At such temperatures, GBs are immobile, where as the grain surfaces (grains touching the liquid) can freely evolve. Therefore, the kinetic coefficient τ (in Equation 4.6) for grain/grain interaction has been assigned suitable values to ensure stiff or immobile GBs.

- The Discrete Element simulations of Virgo et al. [247, 248] explored the complex interaction of fractures with veins, as a function of vein misorientation with respect to principle stress, and strength ratio between the vein and host rock and degree of sealing of the vein. On the contrary, the algorithm that I use to introduce the crack inside the numerical domain is purely geometrical (reported in chapters 10, 11 and 12). The crack shape in every event is kept constant but the location is varied. Additionally, the crack aperture is chosen to be constant in simulations of bitaxial sealing (Figure 4.5(c)), such that the crystal facets develop and growth competition sets in before the fracture is sealed. For the unitaxial sealing, I assume the opposite i.e. crystal facets do not develop and growth competition does not set in before every sealing event is completed. These assumptions are essentially made to keep the parameter study manageable, and it can be easily varied in future models to simulate systems with variable crack aperture [249]. In future studies, location of the fractures can be calculated using mechanics-based discrete element algorithms presented by Virgo et al. [247, 248].

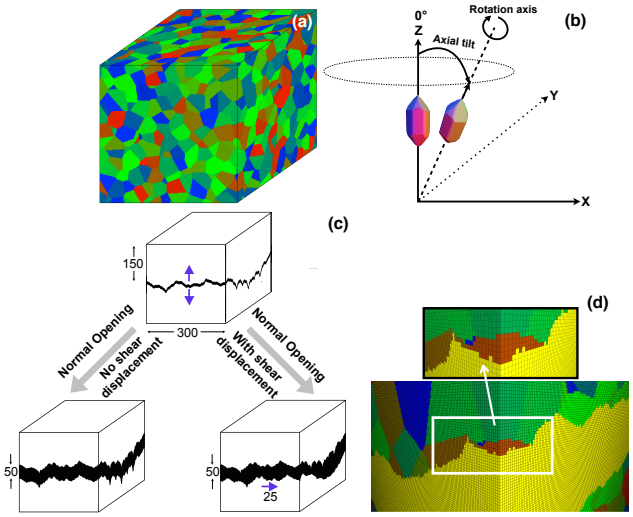

Figure 4.5.: (a) 3D polycrystalline quartz generated using voronoi tessellation. The colors illustrate the axial tilt as per the color-map below (b) The definition of crystal orientation in 3D. The colored facets are meant for visual illustration and is *not* related to the color legend shown below. (c) Schematic diagram showing the simulation box size and crack configurations used for 3D phase-field simulations. A crack aperture size of 50 grid points is used for normal opening (left). A shear displacement of 25 grid-points towards right-hand size is induced by numerical pre-processing for the second case (right). The 3D surface profiles of fractures are generated using diamond-square algorithm [250]. (d) Magnified views of the fractured domain to qualitatively demonstrate the numerical grid resolution.

4.2. Grand chemical potential modeling approach

In order to conduct large scale quantitative pattern formation simulations of the order of micrometer, certain modifications are required in the model proposed in the previous section. The need for such modifications are borne out of twin difficulties:

1. The interfacial energy $\sigma_{\alpha\beta}$ of an α/β interface is a function of the chemical free energy density landscape in the system, and

2. the equilibrium interface width $\Lambda_{\alpha\beta}$ becomes far too restrictive for simulating large

scale microstructures.

Both these restrictions are described elegantly in the previous work of Choudhury and Nestler [2]. In the following section, these model modifications are summarized. This is followed by the thermodynamic description of the Fe-C alloys in consideration.

4.2.1. Phase-field model

I start by writing down the grand-potential functional of the system, incorporating the interfacial and bulk contributions of the respective phases. The evolution equations for the phase and concentration fields can be evaluated in the standard way. Phase evolution is determined by the phenomenological minimization of the modified functional which is formulated as the *grand potential functional*[3],

$$\Omega\left(T,\boldsymbol{\mu},\boldsymbol{\phi}\right) = \int_{V}\left(\Psi\left(T,\boldsymbol{\mu},\boldsymbol{\phi}\right)+\left(\epsilon\tilde{a}\left(\boldsymbol{\phi},\nabla\boldsymbol{\phi}\right)+\frac{1}{\epsilon}\tilde{w}\left(\boldsymbol{\phi}\right)\right)\right)dV. \tag{4.8}$$

I write the grand potential density Ψ, as an interpolation of the individual grand potential densities Ψ_α, where Ψ_α are functions of the chemical potential $\boldsymbol{\mu}$ and temperature T in the system,

$$\Psi\left(T,\boldsymbol{\mu},\boldsymbol{\phi}\right) = \sum_{\alpha=1}^{N}\Psi_\alpha\left(T,\boldsymbol{\mu}\right)h_\alpha\left(\boldsymbol{\phi}\right) \quad \text{with,} \tag{4.9}$$

$$\Psi_\alpha\left(T,\boldsymbol{\mu}\right) = f_\alpha\left(\boldsymbol{c}^\alpha\left(\boldsymbol{\mu}\right),T\right)-\sum_{i=1}^{K-1}\mu_i c_i^\alpha\left(\boldsymbol{\mu},T\right) \tag{4.10}$$

The concentration $c_i^\alpha\left(\boldsymbol{\mu},T\right)$ is an inverse of the function $\mu_i^\alpha\left(\boldsymbol{c},T\right)$ for every phase α and component i. From equation 4.9, the following relation can be derived,

$$\frac{\partial\Psi\left(T,\boldsymbol{\mu},\boldsymbol{\phi}\right)}{\partial\mu_i} = \sum_{\alpha=1}^{N}\frac{\partial\Psi_\alpha\left(T,\boldsymbol{\mu}\right)}{\partial\mu_i}h_\alpha\left(\boldsymbol{\phi}\right). \tag{4.11}$$

where, $h_\alpha\left(\phi\right)=\phi_\alpha^2\left(3-2\phi_\alpha\right)+2\phi_\alpha\sum_{\beta<\gamma,(\beta,\gamma)\neq\alpha}\phi_\beta\phi_\gamma$. Since, the grand potential density $\Psi\left(T,\boldsymbol{\mu},\boldsymbol{\phi}\right)$, is the *Legendre transform* of the free energy density of the system $f\left(T,\boldsymbol{c},\boldsymbol{\phi}\right)$, and from their coupled relation $\dfrac{\partial\Psi\left(T,\boldsymbol{\mu},\boldsymbol{\phi}\right)}{\partial\mu_i}=-c_i$, it follows that,

$$c_i = \sum_{\alpha=1}^{N}c_i^\alpha\left(\boldsymbol{\mu},T\right)h_\alpha\left(\boldsymbol{\phi}\right). \tag{4.12}$$

[3]The development of this generalized model traces back to the original work of A.C and B.N [1, 2]. In part III, K.A. adapted this model to study the eutectoid transformation in binary Fe-C steel.

The evolution equation for the N phase-field variables can be written as,

$$\tau\epsilon\frac{\partial\phi_\alpha}{\partial t}=\epsilon\left(\nabla\cdot\frac{\partial\tilde{a}\left(\boldsymbol{\phi},\nabla\boldsymbol{\phi}\right)}{\partial\nabla\phi_\alpha}-\frac{\partial\tilde{a}\left(\boldsymbol{\phi},\nabla\boldsymbol{\phi}\right)}{\partial\phi_\alpha}\right)-\frac{1}{\epsilon}\frac{\partial\tilde{w}\left(\boldsymbol{\phi}\right)}{\partial\phi_\alpha}-\frac{\partial\Psi\left(T,\boldsymbol{\mu},\boldsymbol{\phi}\right)}{\partial\phi_\alpha}-\Lambda, \tag{4.13}$$

where Λ is the Lagrange parameter to maintain the constraint $\sum_{\alpha=1}^{N}\phi_\alpha=1$. $\tilde{a}\left(\boldsymbol{\phi},\nabla\boldsymbol{\phi}\right)$ represents the gradient energy density and has the form,

$$\tilde{a}\left(\boldsymbol{\phi},\nabla\boldsymbol{\phi}\right)=\sum_{\substack{\alpha,\beta=1\\(\alpha<\beta)}}^{N,N}\tilde{\sigma}_{\alpha\beta}|q_{\alpha\beta}|^2, \tag{4.14}$$

where $q_{\alpha\beta}=(\phi_\alpha\nabla\phi_\beta-\phi_\beta\nabla\phi_\alpha)$ is a normal vector to the $\alpha-\beta$ interface. The double obstacle potential $\tilde{w}\left(\boldsymbol{\phi}\right)$ which is previously described in [1, 54, 198] can be written as,

$$\tilde{w}\left(\boldsymbol{\phi}\right)=\frac{16}{\pi^2}\sum_{\substack{\alpha,\beta=1\\(\alpha<\beta)}}^{N,N}\tilde{\sigma}_{\alpha\beta}\phi_\alpha\phi_\beta, \tag{4.15}$$

where $\tilde{\sigma}_{\alpha\beta}$ is the surface energy. The parameter τ is written as $\frac{\sum_{\alpha<\beta}^{N,N}\tau_{\alpha\beta}\phi_\alpha\phi_\beta}{\sum_{\alpha<\beta}^{N,N}\phi_\alpha\phi_\beta}$, where $\tau_{\alpha\beta}$ is the relaxation constant of the $\alpha-\beta$ interface.

The concentration fields are obtained by a mass conservation equation for each of the $K-1$ independent concentration variables c_i. The evolution equation for the concentration fields can be derived as,

$$\frac{\partial c_i}{\partial t}=\nabla\cdot\left(\sum_{j=1}^{K-1}M_{ij}\left(\boldsymbol{\phi}\right)\nabla\mu_j\right). \tag{4.16}$$

$$M_{ij}\left(\boldsymbol{\phi}\right)=\sum_{\alpha=1}^{N}M_{ij}^{\alpha}g_\alpha\left(\boldsymbol{\phi}\right), \tag{4.17}$$

where each M_{ij}^{α} represents the mobility matrix, of the phase α, calculated by multiplying the diffusivity matrix with susceptibility matrix as,

$$M_{ij}^{\alpha}=D_{ik}^{\alpha}\frac{\partial c_k^{\alpha}\left(\boldsymbol{\mu},T\right)}{\partial\mu_j}. \tag{4.18}$$

In the above expression (written in Einstein notation for a shorter description), a repeated index implies sum over all the elements. Every M_{ij}^{α} value is weighed with respect to the phase fractions represented by $g_\alpha\left(\boldsymbol{\phi}\right)$ which gives the total mobility $M_{ij}\left(\boldsymbol{\phi}\right)$. The function $g_\alpha\left(\boldsymbol{\phi}\right)$ is in general not same as $h_\alpha\left(\boldsymbol{\phi}\right)$ which interpolates the grand potentials,

however, in the present description, I utilize the same. D_{ij}^{α} represent the inter-diffusivities in phase α and so on. Both the evolution equations require the information about the chemical potential $\boldsymbol{\mu}$. Two possibilities exist to determine the unknown chemical potential $\boldsymbol{\mu}$.

- The chemical potential $\boldsymbol{\mu}$ can be derived from the constraint relation in equation 4.12. The $K-1$ independent components μ_i are determined by simultaneously solving the $K-1$ constraints for each of the $K-1$ independent concentration variables c_i, from the given values of c_i and ϕ_α at a given grid point. A Newton iteration scheme can be used for solving the system of equations,

$$\left\{\mu_i^{n+1}\right\} = \{\mu_i^n\} - \left[\sum_{\alpha=1}^{N} h_\alpha\left(\boldsymbol{\phi}\right) \frac{\partial c_i^\alpha\left(\boldsymbol{\mu}^n, T\right)}{\partial \mu_j}\right]_{ij}^{-1} \left\{c_i - \sum_{\alpha=1}^{N} c_i^\alpha\left(\boldsymbol{\mu}^n, T\right) h_\alpha\left(\boldsymbol{\phi}\right)\right\}, \quad (4.19)$$

  where $\{\}$ represents a vector while $[]$ denotes a matrix.

- Alternatively, explicit evolution equations for all the $K-1$ independent chemical potentials, can be formulated by inserting the constraint equation 4.12 into the evolution equation for each of the concentration fields. For a general, multi-phase, multi-component system, the evolution equations for the components of the chemical potential $\boldsymbol{\mu}$ can be written in matrix form by,

$$\left\{\frac{\partial \mu_i}{\partial t}\right\} = \left[\sum_{\alpha=1}^{N} h_\alpha\left(\boldsymbol{\phi}\right) \frac{\partial c_i^\alpha\left(\boldsymbol{\mu}, T\right)}{\partial \mu_j}\right]_{ij}^{-1} \left\{\nabla \cdot \sum_{j=1}^{K-1} M_{ij}\left(\boldsymbol{\phi}\right) \nabla \mu_j - \sum_{\alpha=1}^{N} c_i^\alpha\left(\boldsymbol{\mu}, T\right) \frac{\partial h_\alpha\left(\boldsymbol{\phi}\right)}{\partial t}\right\}. \quad (4.20)$$

In the present work, an explicit formulation, as shown in equation 4.20 have been used for calculating $K-1$ independent chemical potentials.

The diffusion coefficient (D_i) that accounts for the transport of solute inside the phase volumes (D_i^α) and along the interphase interfaces $(D_i^{\alpha\beta})$ is given by:

$$D_i = \sum_{\alpha=1}^{N} D_i^\alpha \phi_\alpha + \frac{1}{\epsilon} \sum_{\alpha<\beta}^{N,N} D_i^{\alpha\beta} \phi_\alpha \phi_\beta. \quad (4.21)$$

As the relaxed (stable) interface $\phi\left(x\right)$ contour has a sinusoidal profile, the effective diffusion coefficient through the interface can be determined using the values of D_i^α (diffusivity of i^{th} component in phase volume) and $D_i^{\alpha\beta}$ (diffusivity of i^{th} component in

interphase interfaces)

$$\int_{\epsilon/2}^{-\epsilon/2} \phi_\alpha \phi_\beta dx = \int_{\epsilon/2}^{-\epsilon/2} \phi_\alpha \left(1 - \phi_\alpha\right) dx = \frac{\epsilon}{8}$$
$$\text{with } \phi_\alpha = \frac{1}{2}\left\{1 + \sin\left(\frac{\pi}{\epsilon}x\right)\right\} \tag{4.22}$$

On integrating equation 4.21 over the interfacial width (from $-\epsilon/2$ to $-\epsilon/2$), average diffusivity in the interphase interfaces is expressed as

$$D_i^{\text{interface}} = \left[D_i^\alpha \epsilon + \frac{1}{\epsilon} D_i^{\alpha\beta} \cdot \frac{\epsilon}{8}\right] . \frac{1}{\epsilon} = D_i^\alpha + \frac{D_i^{\alpha\beta}}{8\epsilon}. \tag{4.23}$$

4.2.2. Thermodynamic description

In order to describe the thermodynamics of the respective phases, one can approximate the variation of the grand-potential of the respective phases using a polynomial of second degree in the chemical potential. Without going into the details, I would like to state that such an approximation is the minimum requirement for fitting the Gibbs-Thomson coefficients of the respective interfaces. In the present investigation I am especially interested in the coupled growth of ferrite(α) and cementite(β) in austenite(γ). Hence, the Gibbs-Thomson coefficients of the $\alpha - \gamma$ and $\beta - \gamma$ interfaces are important parameters required for the correct description of the system. Also, since I am dealing with a binary system, I have only a single independent chemical potential μ, and one define the functions with only this chemical potential as the argument. I start by writing the grand-potential of a given phase as,

$$\Psi^\alpha\left(T, \mu\right) = A^\alpha\left(T\right)\mu^2 + B^\alpha\left(T\right)\mu + C^\alpha\left(T\right). \tag{4.24}$$

At the eutectoid temperature T_E, where the three phases(α, β, γ) are at equilibrium, once can fix the coefficients in the following manner,

$$A^\alpha\left(T_E\right) = \frac{1}{2}\left(\frac{\partial^2 \Psi^\alpha}{\partial \mu^2}\right)_{T_E, \mu_{eq}} \equiv \frac{-V_m}{\dfrac{\partial^2 G^\alpha}{\partial c^2}} \tag{4.25}$$

$$B^\alpha\left(T_E\right) = -c - 2A^\alpha \frac{\mu_{eq}}{V_m} \tag{4.26}$$

$$C^\alpha\left(T_E\right) = \frac{G^\alpha}{V_m} + A^\alpha\left(T_E\right)\left(\frac{\mu_{eq}}{V_m}\right)^2 \tag{4.27}$$

where V_m is the molar volume, G^α is the free energy of the phase at the eutectoid composition and the respective equilibrium temperature. The first derivative $\dfrac{\partial G^\alpha}{\partial c}$,

which is the chemical potential μ_{eq} and the second derivative of the free energy $\frac{\partial^2 G^\alpha}{\partial c^2}$, are also extracted from the thermodynamic functions of the respective phases derived from the CALPHAD database [3]. I point out that while the above procedure fixes the coefficients, A, B, C for austenite and ferrite, the calculation of corresponding values for the cementite phase, are not as generic. Theoretically, the free energy as a function of composition of the cementite phase is represented by a point (only). However, for phase-field calculations, I require information about the changes in free energy, at least for small differences in composition. The database I use for this calculation yields two free energy values corresponding to compositions on either side of the eutectoid composition (of cementite). One can utilize this information together with the chemical potential of the cementite phase in equilibrium with the austenite (at the eutectoid composition) to derive the free energy as a function of composition for the cementite phase (a parabola with a narrow opening). The grand-potential description is obtained by performing the Legendre transform of the free energy density which gives the grand-potential density (a wide-inverted parabola). It is worth mentioning that a limiting case (not applied here) could also be adopted for stoichiometric compounds (in general) by assuming the coefficient A of cementite to be zero. This is equivalent to assuming $\frac{\partial^2 f}{\partial c^2}$ as infinity. The coefficients B and C can thereafter be fixed using the information about the equilibrium chemical potential and the grand-potential both of which are thermodynamically defined for the stoichiometric compound as well[4].

To fit the information of the slopes of the equilibrium lines of the phase diagram, it is essential to describe the variation of the grand-potential as a function of temperature. One can achieve this through a linear interpolation of the coefficients of the grand-potential density functions. The properties at a chosen lower temperature of ferrite and austenite are fixed by utilizing the same procedure as in equation 4.27, however using the values of the free energy G^α, the chemical potential and the second derivative of the free energy with respect to concentration are derived from the thermodynamic functions in CALPHAD at the chosen temperature, and are computed at the respective phase concentrations at the eutectoid temperature. Due to unavailability of the chemical potential for cementite from the CALPHAD databases, the case of the cementite is treated differently. One can derive this information, using the equilibrium between the cementite and austenite and approximating the chemical potential and grand-potential from the value given for the austenite at the chosen temperature, as both these quantities must be equal for the two phases at equilibrium. The procedure suffices because the austenite-cementite equilibrium is relevant during coupled growth of the ferrite and the cementite phases from the austenite.

It is noteworthy that in the present work, I have not modeled the difference in diffusive mechanisms of the cementite phase. While it may not be completely appropriate for the case of eutectoid reaction in steels, yet it does not hamper the spirit of the present work

[4]The procedure of determining the coefficients namely A, B and C is outlined by K.A. However, the curve fitting technique described in the preceding paragraph was jointly conducted by S.S. and M.M.

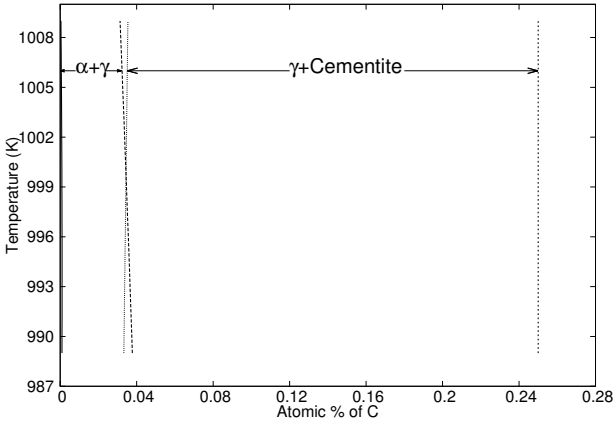

Figure 4.6.: Calculated phase diagram[5]

.

which is the comparison between phase-field simulations and a modified Jackson-Hunt theory. Therefore, in the present discussion, the set of parameters chosen for the diffusion of carbon in cementite are exemplary only for a possible eutectoid transformation.

4.2.3. Relation to sharp-interface limit

In this section I derive the relation between the simulation parameters and the corresponding quantities in the sharp interface limit. Two of these quantities are the Gibbs-Thomson coefficient and the slopes of the equilibrium co-existing lines. These relations can be derived from the Clausius-Clapeyron equation for the case of binary alloys which writes as,

$$\frac{\partial \mu}{\partial T} = \frac{\left(\frac{\partial \Psi^{\alpha}}{\partial T} - \frac{\partial \Psi^{\gamma}}{\partial T}\right)}{(c^{\alpha} - c^{\gamma})}. \tag{4.28}$$

[5]The C code to generate this phase diagram was originally developed by A.C. for eutectic alloys. This code was extended by K.A. to generate the illustrated phase diagram relevant for eutectoid transformation in binary Fe-C alloys.

Expanding $\frac{\partial \mu}{\partial T} = \frac{\partial \mu^{\alpha,\gamma}}{\partial c}\frac{\partial c^{\alpha,\gamma}}{\partial T}$ one can derive the slope of the equilibrium co-existence lines as,

$$m^{\alpha,\gamma} = \frac{\partial c^{\alpha,\gamma}}{\partial \mu}\frac{(c^{\alpha}-c^{\gamma})}{\left(\frac{\partial \Psi^{\alpha}}{\partial T}-\frac{\partial \Psi^{\gamma}}{\partial T}\right)} = \frac{-1}{2A^{\alpha,\gamma}}\frac{(c^{\alpha}-c^{\gamma})}{\left(\frac{\partial \Psi^{\alpha}}{\partial T}-\frac{\partial \Psi^{\gamma}}{\partial T}\right)}. \tag{4.29}$$

Similarly the Gibbs-Thomson coefficient $\Gamma_{\alpha\gamma}$ derives as;

$$\Gamma_{\alpha\gamma} = \frac{\tilde{\sigma}_{\alpha\gamma}}{\left(\frac{\partial \Psi^{\alpha}}{\partial T}-\frac{\partial \Psi^{\gamma}}{\partial T}\right)}, \tag{4.30}$$

where $\tilde{\sigma}_{\alpha\gamma}$ is the surface tension of the $\alpha-\gamma$ interface. Similar expressions for the Gibbs-Thomson coefficients of the cementite phase can be derived by replacing α with β in the preceding equations. Theoretically, the deviations of chemical potential or the concentrations due to curvature, would be non-existent for the cementite phase, by the virtue of the infinite values of $\frac{\partial^2 f}{\partial c^2}$. However, the approximate construction of the grand-potential densities allow small deviations in composition due to curvature effects, although of a much lower order as compared to the austenite and ferrite phases.

In my simulations, I set the conditions such that there is no interface kinetics in direct correlation to the conditions imposed in the theoretical analysis. We derive the same, by setting the interface relaxation coefficient $\tau_{(\alpha,\beta)\gamma}$ through a thin-interface analysis [2, 199] as,

$$\tau_{(\alpha,\beta)\gamma} = \frac{\left(c^{(\alpha,\beta)}-c^{\gamma}\right)^2}{D^{\gamma}\frac{\partial c^{\gamma}}{\partial \mu}}(M+F) \tag{4.31}$$

where $c^{(\alpha,\beta)}$ are the equilibrium concentrations of the phases at equilibrium at the eutectoid temperature and M, F are solvability integrals derived from the thin-interface analysis. The total sum of $M+F \approx 0.222$ which is used in the simulations. As can be seen from the nature of the phase diagram in Figure 4.6, the difference between these concentrations change a little with changing temperature. Hence, the assumption of using the values at the eutectoid temperature holds. I would like to state that the equation for the relaxation constant $\tau_{(\alpha,\beta)\gamma}$ used is strictly valid in cases pertaining to vanishing diffusivity in one of the phases, or for instances of equal diffusivities in both phases. In the former case, the relation must be used with the anti-trapping current which removes the chemical potential jump at the interface, arising out of artificial solute trapping as a consequence of choosing a thick interface.

The case when the diffusivities in both the phases is arbitrary, the problem is not as trivial. It is to be noted that the whole class of problems which falls in the category of

two-phase transport through a complex structure inherently exhibit thin-interface effects for stationary/moving interfaces. Despite some recent progress, so far no method has been found to completely eliminate thin-interface effects in the case of arbitrary diffusion coefficients in the two phases with a non-stationary interface [200–203] in a closed form manner. One of the principal reasons for non-closure of the problem, is that the artificial discontinuous jump effects (arising out of arbitrary diffusivities) are independent of the velocity of the interface. This implies that such effects cannot be removed through the imposition of an anti-trapping current that has been previously used for removing the artificial solute trapping effects in one-sided diffusion problems. While few hints to the solution by the introduction of tensorial mobilities [201] and through the usage of artificial parameter χ (related to diffusive current in solid) [204] are present, a closed form solution is still in the process of being worked out. This in all certainty is not the highlight or aim of the present work[6].

The reason which allows us to take the liberty of overlooking these defects and derive meaningful results, is that the interface width used in the present problem is of a very small magnitude. It is worth noting that the interface width is proportional to the capillary length of the phases and in the present formulation, scales inversely with the factor $\frac{\partial^2 f}{\partial c^2}$. Apparently, while the capillary length of the phases, austenite and ferrite are close to each other, the case of cementite is very restrictive to the choice of the interface width. By deriving leverage out of the fact that the thin-interface defects scale with the interface width, a small choice of the interface width in present simulations allows us to limit the magnitude of the thin-interface defects, and facilitates reasonably quantitative results.

In order to derive the relaxation constant, once can utilize the mobility of the austenite and assume that even though the gradients of the chemical potential exist in the solid, the principal driving force is still due to the gradient of the chemical potential in the austenite. In the absence of a closed form solution, this seems like a reasonable choice. I substantiate my claim in the following sections, that the errors due to this assumption, do not seem to affect the quantitative aspects of the present results.

[6]The preceding paragraph, although written in words of K.A. is originally based on the views of A.C.

Part III.

Phase-field modeling of eutectoid transformation in Fe-C steels

5. Comparison of simulated eutectoid growth rate with theory in volume diffusion-controlled regime

In the following chapter, I investigate the lamellar growth of pearlite at the expense of austenite during the eutectoid transformation in steel. To begin with, I extend the Jackson–Hunt-type calculation (previously used to analyze eutectic transformation) to eutectoid transformation by accounting for diffusion in all the phases. This is followed by a comparison of the numerically simulated growth rate with the extended theory. This chapter was published in [5].

5.1. Theoretical analysis of coupled growth

I consider the diffusion of the components A and B ahead of the planar eutectoid front. For calculating the concentration fields ahead of the growth front in question, one can make the following Fourier series expansion for c_A and c_B,

$$c_X^{\gamma} = \sum_{n=-\infty}^{\infty} X_n e^{ik_n x - q_n z} + (c_X^{\infty})_{\gamma}\,, \qquad X = A, B \tag{5.1}$$

where γ is the austenite phase. In the respective growing phases (α and β) the concentration fields can be respectively written as,

$$c_X^{\nu} = \sum_{n=-\infty}^{\infty} X_n e^{ik_n x + q_n z} + (c_X^{\infty})_{\nu}\,, \qquad X = A, B \quad \nu = \alpha, \beta. \tag{5.2}$$

An elaborate description of the terms involved in the above expression and derivation from a stationary diffusion equation has been described in detail in the previous work on eutectic growth [205]. In the field under consideration, the growth front is assumed to be at $z = 0$. Further, $z > 0$ depicts austenite phase where exponential profiles for the concentrations of components A and B exist. For $z < 0$, the composition profile in pearlite (for ferrite and cementite phases) have similar exponential profiles. Therefore, to account for the symmetry across the interface, I change the sign of the exponent $e^{-q_n z}$ to $e^{q_n z}$ when treating the concentration profiles in ferrite and cementite phases ($\forall z < 0$).

In the Jackson-Hunt analysis for the calculation of diffusion field in liquid and solid, the Stefan's condition at $\nu - \gamma$ interface, which expresses mass-conservation upon the phase transformation reads as

$$D^{\nu}\partial_n c_X^{\nu}|_{z=0} - D^{\gamma}\partial_n c_X^{\gamma}|_{z=0} = v_n \Delta c_X^{\nu}, \qquad \nu = \alpha, \beta \tag{5.3}$$

where $\partial_n c_X^{\nu}$ denotes the partial derivative of c_X^{ν} in the direction normal to the interface. The quantity v_n is the normal velocity of the interface (positive for a growing front) and $\Delta c_X^{\nu} = c_X^{\gamma} - c_X^{\nu}$. D^{γ} and D^{ν} are chemical diffusion coefficients for bulk and growing phases respectively. For using the Stefan condition, I take the derivative of c_X^{ν} with respect to the 'z' coordinate

$$\partial_z c_X^{\nu} \mid_{z=0} = \sum_{n=-\infty}^{\infty} q_n X_n e^{ik_n x} \qquad \nu = \alpha, \beta \tag{5.4}$$

for the growing phases and

$$\partial_z c_X^{\gamma} \mid_{z=0} = \sum_{n=-\infty}^{\infty} -q_n X_n e^{ik_n x}, \tag{5.5}$$

for the austenite phase. Integration across one lamella period (lamellar spacing) λ gives,

$$q_n X_n^{\alpha} D^{\alpha} \eta_{\alpha} \lambda + q_n X_n^{\beta} D^{\beta} \eta_{\beta} \lambda + q_n X_n^{\gamma} D^{\gamma} \lambda = \sum_{j=0}^{M-1} \int_{x_j \lambda}^{x_{j+1} \lambda} v_n \Delta c_X^{\nu_j} e^{-ik_n x} dx. \tag{5.6}$$

where, M denotes the number of lamellae and η_{α} and η_{β} are the respective phase volume fractions. In the above equation, there are three sets of unknowns X_n^{α}, X_n^{β} and X_n^{γ} in contrast to the classical Jackson-Hunt type analysis with vanishing diffusivity in the solid, where X_n^{γ} remains the only unknown, and is thereby fixed by the property of orthogonality of the respective modes. In the present situation, a relation among the Fourier coefficients is needed, to fix the respective unknowns. One can achieve these relations by arguing that the constitutional undercooling can be derived equivalently by using either the shifts in the equilibrium concentrations of the bulk or the growing phases. Hence, the resultant shift in the average concentration in the γ phase and the corresponding shift in the α and β phases must be constrained by the relation,

$$m_X^{\alpha}(\langle c_X^{\alpha} \rangle - c_{X,E}^{\alpha}) = m_X^{\alpha,\gamma}(\langle c_X^{\gamma} \rangle - c_{X,E}^{\gamma}) \tag{5.7}$$

$$m_X^{\beta}(\langle c_X^{\beta} \rangle - c_{X,E}^{\beta}) = m_X^{\beta,\gamma}(\langle c_X^{\gamma} \rangle - c_{X,E}^{\gamma}) \tag{5.8}$$

where $\langle c_X^{\alpha} \rangle$, $\langle c_X^{\beta} \rangle$ and $\langle c_X^{\gamma} \rangle$ denote the average phase concentrations at the interface, while $c_{X,E}^{\alpha}$, $c_{X,E}^{\beta}$ and $c_{X,E}^{\gamma}$ are the eutectoid compositions. m_X^{α} and m_X^{β} represent the slopes (with respect to the concentration of component 'X') of the α and β phase in equilibrium with austenite. Similarly, $m_X^{\alpha,\gamma}$ and $m_X^{\beta,\gamma}$ represent the slopes of the co-existence lines of the austenite phase in equilibrium with α and β phases respectively.

While such an equation certainly has multiple solutions, I invoke the following assumption,

$$m_X^{\alpha} X_n^{\alpha} = m_X^{\alpha,\gamma} X_n^{\gamma} \tag{5.9}$$

$$m_X^{\beta} X_n^{\beta} = m_X^{\beta,\gamma} X_n^{\gamma} \tag{5.10}$$

which satisfies the given property. Substituting the preceding condition in equation 5.6 yields,

$$\begin{aligned} q_n X_n^{\gamma} \delta_{nm} \lambda \left[\frac{D^{\alpha}}{D^{\gamma}} \frac{m_X^{\alpha,\gamma}}{m_X^{\alpha}} \eta_{\alpha} + \frac{D^{\beta}}{D^{\gamma}} \frac{m_X^{\beta,\gamma}}{m_X^{\beta}} \eta_{\beta} + 1 \right] &= \sum_{j=0}^{M-1} \int_{x_j \lambda}^{x_{j+1}\lambda} \frac{v_n}{D^{\gamma}} \Delta c_X^{\nu_j} e^{-ik_n x} dx \\ &= \frac{2}{l} \sum_{j=0}^{M-1} \int_{x_j \lambda}^{x_{j+1}\lambda} e^{-ik_n x} \Delta c_X^{\nu_j} dx \end{aligned} \tag{5.11}$$

and hence, I rearrange to

$$\begin{aligned} X_n^{\gamma} = \frac{4}{l q_n \lambda k_n \left[\frac{D^{\alpha}}{D^{\gamma}} \frac{m_X^{\alpha,\gamma}}{m_X^{\alpha}} \eta_{\alpha} + \frac{D^{\beta}}{D^{\gamma}} \frac{m_X^{\beta,\gamma}}{m_X^{\beta}} \eta_{\beta} + 1 \right]} \cdot \\ \sum_{j=0}^{M-1} \Delta c_X^{\nu_j} e^{-ik_n \lambda (x_{j+1} + x_j)/2} \sin\left[k_n \lambda \left(x_{j+1} - x_j\right)/2\right] \end{aligned} \tag{5.12}$$

where ν_j represents the name of one of the growing phases (α, β) occurring in the sequence of M lamellae $(\nu_0, \nu_1, \nu_2 \ldots \nu_{M-1})$ periodically arranged with a repeat distance (lamellar spacing) λ. The symbol l appearing in the denominator represents the characteristic length scale of the concentration boundary layer. By considering the negative summation indices, one can formulate real and imaginary combinations of these coefficients,

$$\begin{aligned} X_n^{\gamma} + X_{-n}^{\gamma} &= \frac{8}{l q_n \lambda k_n \rho} \sum_{j=0}^{M-1} \Delta c_X^{\nu_j} \cos\left[k_n \lambda \left(x_{j+1} + x_j\right)/2\right] \sin\left[k_n \lambda \left(x_{j+1} - x_j\right)/2\right] \\ i\left(X_n^{\gamma} - X_{-n}^{\gamma}\right) &= \frac{8}{l q_n \lambda k_n \rho} \sum_{j=0}^{M-1} \Delta c_X^{\nu_j} \sin\left[k_n \lambda \left(x_{j+1} + x_j\right)/2\right] \sin\left[k_n \lambda \left(x_{j+1} - x_j\right)/2\right] \end{aligned} \tag{5.13}$$

where,

$$\rho = \frac{D^{\alpha}}{D^{\gamma}} \frac{m_X^{\alpha,\gamma}}{m_X^{\alpha}} \eta_{\alpha} + \frac{D^{\beta}}{D^{\gamma}} \frac{m_X^{\beta,\gamma}}{m_X^{\beta}} \eta_{\beta} + 1 \tag{5.14}$$

Therefore, equation 5.1 can be rewritten as,

$$\begin{aligned} c_X^\gamma = &\left(c_X^\infty\right)_\gamma + \frac{X_0^\gamma}{\rho} \\ &+ \frac{1}{\rho}\sum_{j=0}^{M-1}\sum_{n=1}^{\infty}\frac{8}{lq_n\lambda k_n}\cos\left[k_n\lambda\left(x_{j+1}+x_j\right)/2\right]\sin\left[k_n\lambda\left(x_{j+1}-x_j\right)/2\right]\cos\left(k_n x\right) \\ &+ \frac{1}{\rho}\sum_{j=0}^{M-1}\sum_{n=1}^{\infty}\frac{8}{lq_n\lambda k_n}\sin\left[k_n\lambda\left(x_{j+1}+x_j\right)/2\right]\sin\left[k_n\lambda\left(x_{j+1}-x_j\right)/2\right]\sin\left(k_n x\right) \end{aligned} \tag{5.15}$$

The general expression for the mean concentration $\langle c_X^\gamma\rangle_m$ ahead of the mth phase of the phase sequence can be calculated to yield

$$\begin{aligned} \langle c_X^\gamma\rangle_m = &\frac{1}{\left(x_{m+1}-x_m\right)\lambda}\int_{x_m\lambda}^{x_{m+1}\lambda} c_X^\gamma dx \\ = &\left(c_X^\infty\right)_\gamma + \frac{X_0^\gamma}{\rho} + \frac{1}{\left(x_{m+1}-x_m\right)\rho}\sum_{n=1}^{\infty}\sum_{j=0}^{M-1}\left\{\frac{16}{\lambda^2 k_n^2 l q_n}\Delta c_X^{\nu_j}\right. \\ &\left.\times\sin\left[\pi n\left(x_{m+1}-x_m\right)\right]\sin\left[\pi n\left(x_{j+1}-x_j\right)\right]\times\cos\left[\pi n\left(x_{m+1}+x_m-x_{j+1}-x_j\right)\right]\right\} \end{aligned} \tag{5.16}$$

For the binary eutectoid system with phases $\alpha,\ \beta,$ and γ, one can derive the average concentrations of the components A, B by setting, $x_0=0,\ x_1=\eta_\alpha,\ x_2=1$ and applying equation 5.16

$$\begin{aligned} \langle c_X^\gamma\rangle_\alpha &= \left(c_X^\infty\right)_\gamma + \frac{X_0^\gamma}{\rho} + \frac{1}{\eta_\alpha\rho}\sum_{n=1}^{\infty}\left\{\frac{16}{\lambda^2 k_n^2 l q_n}\left(\Delta c_X^\alpha - \Delta c_X^\beta\right)\times\sin^2\left(\pi n\eta_\alpha\right)\right\} \\ &\cong \left(c_X^\infty\right)_\gamma + \frac{X_0^\gamma}{\rho} + \frac{2\lambda}{\eta_\alpha\rho l}\mathcal{P}\left(\eta_\alpha\right)\Delta c_X \end{aligned} \tag{5.17}$$

$$\langle c_X^\gamma\rangle_\beta = \left(c_X^\infty\right)_\gamma + \frac{X_0^\gamma}{\rho} - \frac{2\lambda}{\left(1-\eta_\alpha\right)\rho l}\mathcal{P}\left(1-\eta_\alpha\right)\Delta c_X \tag{5.18}$$

with $k_n = 2\pi n/\lambda$, $q_n \approx k_n$, $\lambda/l \ll 1$, $\Delta c_X = \Delta c_X^\alpha - \Delta c_X^\beta$ and the dimensionless function

$$\mathcal{P}\left(\eta\right) = \sum_{n=1}^{\infty}\frac{1}{\left(\pi n\right)^3}\sin^2\left(\pi n\eta\right) \tag{5.19}$$

which has the property $\mathcal{P}\left(\eta\right) = \mathcal{P}\left(1-\eta\right) = \mathcal{P}\left(\eta-1\right)$

Incorporating the Gibbs-Thomson effect and using the relation $l = 2D^\gamma/v$ leads to,

$$\Delta T_\alpha = -m_B^{\alpha,\gamma}B_0^\gamma - \frac{\lambda v}{\eta_\alpha D^\gamma\rho}\mathcal{P}\left(\eta_\alpha\right)m_B^{\alpha,\gamma}\Delta c_B + \Gamma_\alpha\langle\kappa\rangle_\alpha \tag{5.20}$$

$$\Delta T_\beta = -m_A^{\beta,\gamma} A_0^\gamma - \frac{\lambda v}{\eta_\beta D^\gamma \rho} \mathcal{P}\left(\eta_\beta\right) m_A^{\beta,\gamma} \Delta c_A + \Gamma_\beta \langle\kappa\rangle_\beta \tag{5.21}$$

where $\langle\kappa\rangle_\alpha = 2\sin\theta_{\alpha\beta}/\left(\eta_\alpha\lambda\right)$, $\langle\kappa\rangle_\beta = 2\sin\theta_{\beta\alpha}/\left(\eta_\beta\lambda\right)$, $\Gamma_\alpha = \tilde{\sigma}_{\alpha\gamma} T_E/L_\alpha$ and $\Gamma_\beta = \tilde{\sigma}_{\beta\gamma} T_E/L_\beta$. Additionally, for a binary alloy, the coefficients follow the condition, $B_0^\gamma = -A_0^\gamma$. The global front undercooling is determined using the assumption of equal interface undercooling $\Delta T_\alpha = \Delta T_\beta = \Delta T$. For a constant undercooling, I deduce the relation between the growth velocity 'v' and lamellar width 'λ' by eliminating the unknown amplitude A_0^γ (orB_0^γ) as,

$$v = \frac{\Delta T - \dfrac{2T_E}{\lambda\left(m_A^{\beta,\gamma} + m_B^{\alpha,\gamma}\right)}\left[\dfrac{m_B^{\alpha,\gamma}\tilde{\sigma}_{\beta\gamma}\sin\theta_{\beta\alpha}}{\eta_\beta L_\beta} + \dfrac{m_A^{\beta,\gamma}\tilde{\sigma}_{\alpha\gamma}\sin\theta_{\alpha\beta}}{\eta_\alpha L_\alpha}\right]}{-\dfrac{\lambda}{D^\gamma\rho}\left(\dfrac{m_A^{\beta,\gamma} m_B^{\alpha,\gamma}}{m_A^{\beta,\gamma} + m_B^{\alpha,\gamma}}\right)\left[\dfrac{\mathcal{P}\left(\eta_\alpha\right)\Delta c_B}{\eta_\alpha} + \dfrac{\mathcal{P}\left(\eta_\beta\right)\Delta c_A}{\eta_\beta}\right]}. \tag{5.22}$$

It is worth clarifying that in the derived expression for binary eutectoids above, the growing phases α and β posses slopes with opposite signs for the same component. $m_A^{\beta,\gamma}$ and $m_B^{\alpha,\gamma}$ denote the slopes of the phases β and α respectively with respect to the minority component in each phase. Hence, they will always be of the same sign. Therefore, for eutectoid systems, the denominator $m_A^{\beta,\gamma} + m_B^{\alpha,\gamma}$, is non-vanishing. Further, it is important to point the difference of the preceding expression with respect to the relations for the velocity derived for eutectic solidification in absence of diffusion in solid-phases [4, 205]. The velocity differs by the factor ρ, which depends on the ratio of the diffusivities in the growing phases and the bulk phase, together with the ratio of the slopes of the respective phase-coexistence lines.

5.2. Comparison between theory and simulation

In this section, I compare the growth velocity of pearlite obtained from phase-field simulation with the analytical results in the two regimes: diffusion in austenite (only) and diffusion in austenite as well as ferrite. The simulation set-up comprises of a bounding box with periodic boundary conditions in the transverse direction, while no flux boundary conditions are used in the growth direction. The bounding box width in the transverse direction directly controls the lamellar spacing λ such that the pearlitic composition is retained (88% ferrite and 12% cementite). The chemical potential in the bounding box is initialized with the equilibrium chemical potential for eutectoid transformation. The box width in the growth direction is chosen 10 times larger than the lamellar width such that the chemical potential gradient in bulk remains uniform at successive simulation time-steps. In order to completely rule out the possibility of non-uniformity of chemical potential in bulk phase, the simulation is carried in a moving frame (also known as shifting-box simulation). In the present simulations, the domain is shifted in the growth direction (upwards) by adding a row of grid-point at the top of domain and discarding off

Table 5.1.: Parameters used for analytical calculation and for sharp-interface theory

Symbol	Value	Units
T_E	999	K
ΔT	10	K
$\sigma_{\alpha\gamma} = \sigma_{\beta\gamma} = \sigma_{\alpha\beta}$	0.49	J/m^2
$D^{\alpha} = D^{\beta}$	2×10^{-9}	m^2/s
D^{γ}	1×10^{-9}	m^2/s
$A^{\alpha,\gamma} = A^{\beta,\gamma}$	$-1.015385 \times 10^{-11}$	m^3/J
$A^{\alpha,\beta}$	$-1.184616 \times 10^{-12}$	m^3/J
$A^{\beta,\alpha}$	-1.9×10^{-14}	m^3/J
c_A^{α}	8.85×10^{-4}	-
c_A^{β}	0.25	-
c_A^{γ}	0.034433	-
c_B^{α}	0.999115	-
c_B^{β}	0.75	-
c_B^{γ}	0.965567	-
η_{α}	0.88	-
η_{β}	0.12	-
$\theta_{\alpha\beta} = \theta_{\beta\alpha}$	30°	degrees
$\tau_{\alpha\gamma}$ (calculated)	1.724027×10^8	Js/m^4
$\tau_{\beta\gamma}$ (calculated)	7.118288×10^9	Js/m^4

a row of grid-points at the bottom, every time the advancing lamellar front fills up 10% of the simulation box. Further, I have also ensured that the 10% of the box, comprising of the growing phases, have sufficient number of cells to describe the diffusional field. Although, one cannot claim to be error proof, a good match with analytical results, confirms, that the deviations are not large enough to influence the results obtained. To find the co-operative lamellar growth rate, the previously discarded grid-points are aggregated back and the position of advancing interface is determined by finding the position of the contour line $\phi_{\alpha} - \phi_{\beta} = 0$ through a linear interpolation of the neighboring values (where the sign of $\phi_{\alpha} - \phi_{\beta}$ changes). In the present context, α and β denote any two phases, between which the interface is to be isolated.

The rate of change of the position of the interface in transverse direction is plotted as a function of time, and the simulation is run until there is no more change in the velocity of the interface, which indicates the steady-state has been attained. The procedure described above is repeated to calculate the steady state velocities for different lamellar widths 'λ' and plotted for comparison with analytical results as shown in Figure 5.2.

The parameters used for analytical calculation of the lamellar growth velocity as well as for sharp-interface theory as summarized in Table 5.1. The phase profile obtained from the phase-field simulation for the two cases: diffusion in austenite (only) and diffusion in

austenite as well as ferrite are shown in Figure 5.1(a) and Figure 5.1(b) respectively. The

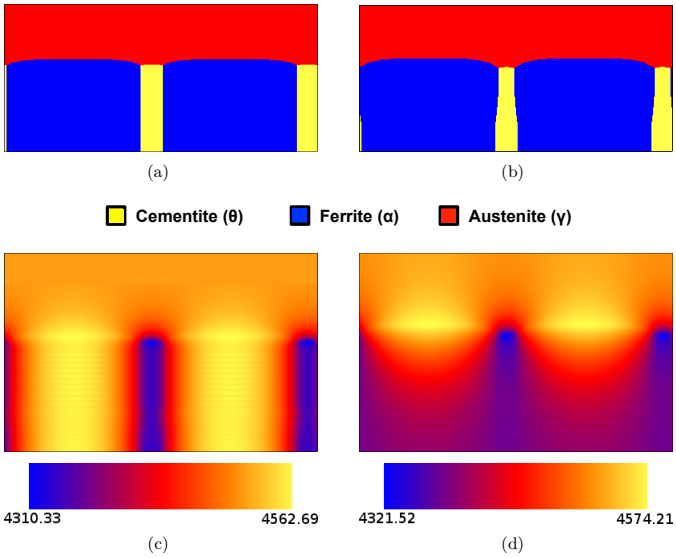

Figure 5.1.: Phase patterns (austenite in red, ferrite in blue and cementite in yellow) and chemical potentials plotted for corresponding cases: (a) and (c) Diffusion in austenite (only) and (b) and (d) Diffusion in austenite as well as ferrite. It is to be noted that the pictures above are merely snapshots depicting the region of interest and not the entire simulation box itself. The pearlite lamella width is 200 μm which is half of the illustrated box-length.

corresponding plots for chemical potential are shown in Figure 5.1(d) and Figure 5.1(e). It is to be noted that the phase-field simulation pictures shown in Figure 5.1 are merely snapshots of the region of interest and do not represent the entire simulation box. The growth velocities of pearlite evolving in austenite at an undercooling of 10K in both the regimes are plotted in Figure 5.2. I observe a reasonable overlap of analytically predicted growth velocity with phase-field results in absence of diffusion in ferrite. However, a small deviation is observed near the critical lamellar spacing when diffusion in ferrite is also accounted for along with diffusion in austenite. In this case, pronounced tapering of cementite near the growth front due to diffusion in ferrite, is observed. It is noteworthy,

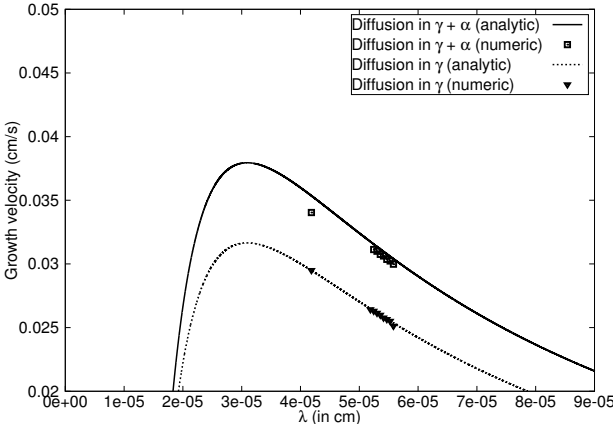

Figure 5.2.: Comparison of pearlitic growth front velocities as a function of lamellar spacing at constant undercooling ($\Delta T = 10K$) derived from a Jackson-Hunt-type calculation with phase-field results in respective diffusion regimes[2].

that such a taper[1] causes a modification of the triple point orientation with respect to the growth direction, and thereby the triple point angles assumed in the analytical derivations differs from those resulting in the simulations. This indeed causes modifications in the velocities near to the critical spacing and the critical spacing itself, which is also reflected in my simulations. However, for spacings further ahead, where the capillary term is less dominant with respect to the solutal effect, the agreement is better. Further, as already shown in previous works [43], there exists a difference between theoretical analysis of the Jackson-Hunt type and quantitative phase-field simulations, which arises because of the inherent assumptions used in the analytical derivations.

[2]The C code to generate the analytical plot was originally developed by A.C. for eutectic alloys. This code was extended by K.A. to generate the illustrated plot relevant for eutectoid transformation in binary Fe-C alloys.

[1]A similar set of simulations using the multiphase-field model [1] was conducted by C.Q. (without utilizing the grand-potential formulation). Although that work is unpublished, those simulations (a separate study) facilitated a direct assessment of the effectiveness of grand-potential model (used in the present studies) by serving as a comparable case. Conceptually, such a comparison helped K.A. in comprehending the role of interfacial excess energies. This line written in words of K.A. is essentially based on a discussion with C.Q.

5.3. Discussion and outlook

In the present chapter, I generalized the Jackson-Hunt analysis in order to incorporate diffusion in the growing phases, in addition to the diffusion in the bulk. The results of the analysis predict that the growth front velocities change by a factor ρ, with respect to the case where diffusivity is absent in the growing phases. Phase-field simulations, conducted with a thermodynamically consistent model, confirm the theoretical predictions fairly well. In addition, the simulations predict the morphology of the growth front showing a tapering of cementite in the direction of growth.

It is worth clarifying that the present work does not aim to represent the eutectoid transformation in Fe-C systems, *in totality*. These studies are limited to *only* a part of the entire eutectoid transformation phenomena, which is to analytically and numerically investigate the influence of diffusion in the growing phases, on the lamellar front velocity, which has been adequately achieved through my results. The presence of a stoichiometric phase like cementite imposes a limitation on the choice of length scale and therefore the interface width, thereby limiting the thin-interface defects arising due to having arbitrary diffusivities in all phases. This argument is further accentuated by a good agreement of analytical and numerical results as plotted in figure 5.2. Further, this near-overlap also suggest that the aim of the present work has been adequately accomplished. Thus, the present phase-field simulations decompose the effect of dual-diffusion mode (in bulk as well as growing phases), in isolation i.e. without considering additional effects for e.g. the lattice strains [97] which influence the growth morphology.

The complete problem of eutectoid transformation however, is complicated and a precise description is not the aim of the present work. The additional ingredients, include the contribution from grain-boundary which is an interesting direction for future research. Therefore, for comparison with experiments and particularly, to present a detailed argumentation with respect to the previous findings [94, 206] based on the results of this article would not be meaningful. To arrive at a reasonable overlap between simulations and experiments, it is necessary to consider the combined influence of bulk and grain-boundary diffusion together with transformation strains in the present phase-field model.

It will also be intriguing to address the faster kinetics of re-austenisation or pearlite dissolution (as compared to pearlite growth) by deriving and transferring ideas from the present work. To this end, studies need to be conducted to establish the exact mechanism and primary diffusion regime that governs the kinetics of such transformations. Low undercooling and presence of preexisting cementite particles in austenite, alter the pearlite growth morphology from lamellar to spheroidized widely known as “divorced pearlite” [196]. The phenomena is addressed in detail in the following chapters to gain further insights on spherodizing behavior or non-cooperative growth of pearlite during widely used annealing treatment of steel.

6. Non-cooperative eutectoid transformation: symmetric arrangement of preexisting cementite

In the present chapter, the simulation results concerning the lamellar to divorced eutectoid transition and the concurrent growth and coarsening regime are discussed. In particular, the influence of undercooling and interparticle spacing is explored as the transformation proceeds from a symmetrical arrangement of preexisting cementite (θ). This chapter was published in [6].

6.1. Lamellar to Divorced transition

As I am primarily interested in amending the criteria which determines whether the eutectoid transformation front evolves by a cooperative (lamellar growth, which leads to the formation of pearlite) or a non-cooperative mechanism (resulting in divorced eutectoid), I use the same input parameters (volume diffusion constants and interfacial energies) for the present phase-field simulations that was used in chapter 5 to simulate a pearlitic morphology. In order to account for the role of diffusion of carbon along the transformation front simultaneously, the interface diffusion constant is assumed to be 1000 times greater than volume diffusion constant in ferrite. The interface relaxation coefficient is derived from a thin-interface analysis which is described elsewhere [2, 199].

The temporal evolution of austenite, ferrite and cementite phases is studied, which is governed by the initial particle spacing at intercritical temperature and the undercooling below the eutectoid temperature (A_1). The simulation domain width in the transverse direction directly controls the spacing (represented by λ) while the radius of the particles is kept same for consistency of the numerical results. In order to compare the present phase-field results with the classical theories, which introduce a criteria for lamellar to divorced transition based on experimental findings [190, 196], I limit the present discussion to a symmetric arrangement of preexisting cementite particles which are embedded in an austenite matrix. The undercooling below the eutectoid temperature (ΔT) as well the particle spacing (λ) is varied to study their effect on the resulting microstructure.

Figure 6.1(a) shows the dependence of undercooling and particle spacing in stimulating a transition from lamellar to divorced morphology. It is noteworthy, that the numerical

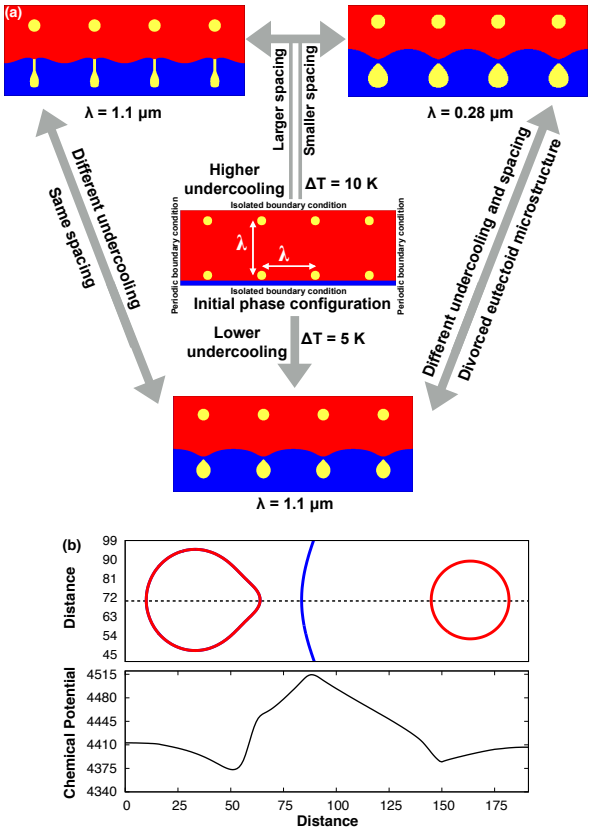

Figure 6.1.: (a) Numerically simulated microstructures at two different undercoolings below the eutectoid temperature ($\Delta T = 5$ and 10 K) and particle spacing ($\lambda = 0.28$ and $1.1\,\mu$m) starting from the same initial arrangement of the phases. The diagram shows that a cooperative growth regime is favored at higher undercooling and spacing leading to the formation of pearlitic lamellae. At lower undercoolings and smaller particle spacings, a non-cooperative mechanism predominates which results in the formation of a divorced eutectoid microstructure. (b) 1-D chemical potential profile for $\Delta T = 5$K and $\lambda = 0.58\,\mu$m plotted along the dashed line connecting the center of both the cementite particles. The profile shows that the carbon partitioned at the α/γ transformation front is incorporated by both the particles which results in non-cooperative eutectoid transformation.

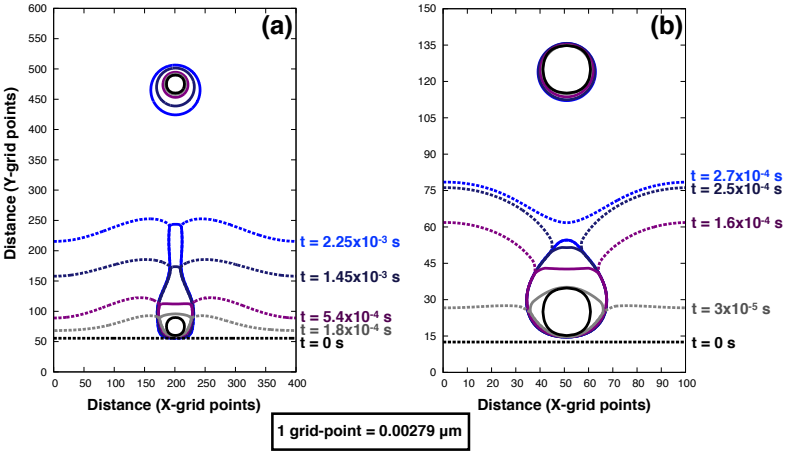

Figure 6.2.: Temporal evolution of the isolevels $\phi_\alpha = 0.5$ (dashed lines representing α/γ interface) and $\phi_\theta = 0.5$ (solid lines representing θ/γ and θ/α interfaces) for the (a) cooperative (resulting in pearlitic lamella) and (b) non-cooperative (resulting in divorced eutectoid) regimes. The pulling-away of the advancing ferrite-austenite interface is evident from the numerically simulated isolevels shown in (b). A comparison of the temporal evolution of the isolines in (a) and (b) indicate that the initial particle spacing 'λ' (number of grid-points along x-axis) governs the switch between both the evolution regimes (for constant undercooling $\Delta T = 10K$).

results accentuate the experimental findings which emphasize a greater tendency of the ferrite-austenite interface to pull away from cementite particles at low undercooling and small spacing. On the contrary, at larger spacing and higher undercooling, a cooperative growth regime is favored which results in the formation of pearlitic lamellae. On analyzing the simulated chemical potential profile in 1-D as shown in Figure 6.1(b), it is apparent that a divorced morphology forms due to the incorporation of partitioned carbon (at the advancing α/γ transformation front) into the existing cementite particles. Thus, a near overlap of the present simulation results with the existing theory demonstrate the general capability of phase-field method in capturing the topological changes during eutectoid transformation.

Figure 6.2[1] compares the temporal evolution of the numerically simulated isolines corresponding to interphase interfaces for a lamellar growth [Figure 6.2(a)] and divorced

[1]The plot showing the temporal evolution was generated by K.A. on the advise of R.M.

eutectoid [Figure 6.2(b)], starting from a symmetric arrangement of cementite particles. As the undercooling is constant for both the cases (ΔT = 10K), the evolution mode (co-operative or non-cooperative) is determined by the initial particle spacing 'λ' (represented by X-axes in Figure 6.2). At a lower value of 'λ' (0.27 μm), the α/γ interface pulls-away from θ, more commonly known as, the non-cooperative growth. However, at a larger value of 'λ' (1.11 μm), the growing phases, α and θ maintain a common transformation front, by evolving cooperatively.

6.2. Concurrent growth and coarsening

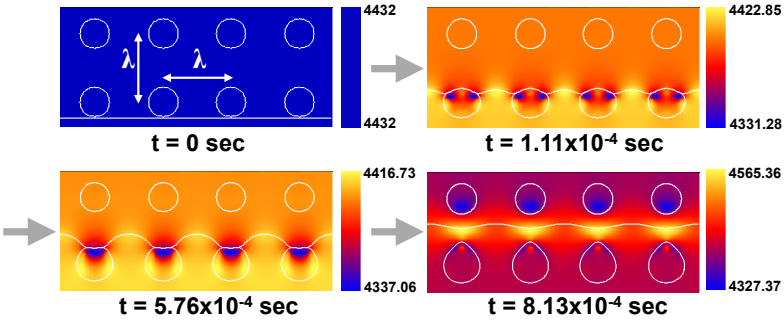

Figure 6.3.: Temporal evolution of the phase contours which are plotted over the corresponding chemical potential maps during concurrent growth and coarsening regime ($\Delta T = 7.5$ K and $\lambda = 0.294\ \mu m$). Coarsening can be observed clearly in Figure 6.4.

The most phenomenal finding of the present numerical studies is the isolation of concurrent growth and coarsening regime during eutectoid transformation. Figure 6.3 shows the temporal evolution of phase contours which are overlaid on the chemical potential map, when the initial cementite spacing is reduced to 0.294 μm at an undercooling of 5 K below the A_1 (eutectoid) temperature. An intermittent coarsening regime sets in before the pulling away of the α/γ interface from cementite particles. In order to provide a detailed exposition of this newly identified regime (which is not clearly visible in Figure 6.3), I plot both the phase contours separately [in Figure 6.4(a)] as well as the 1-D chemical potential profile along the dashed-line [in Figure 6.4(b)] for different simulation time-steps. Depending on the initial distance from the ferrite-austenite transformation front, the cementite particles are labeled as 1 and 2. On comparing the 1-D chemical potential profiles for two different simulation time-steps (t_1 and t_2), I find that a change in the carbon redistribution mechanism is stimulated which leads to coarsening of particles

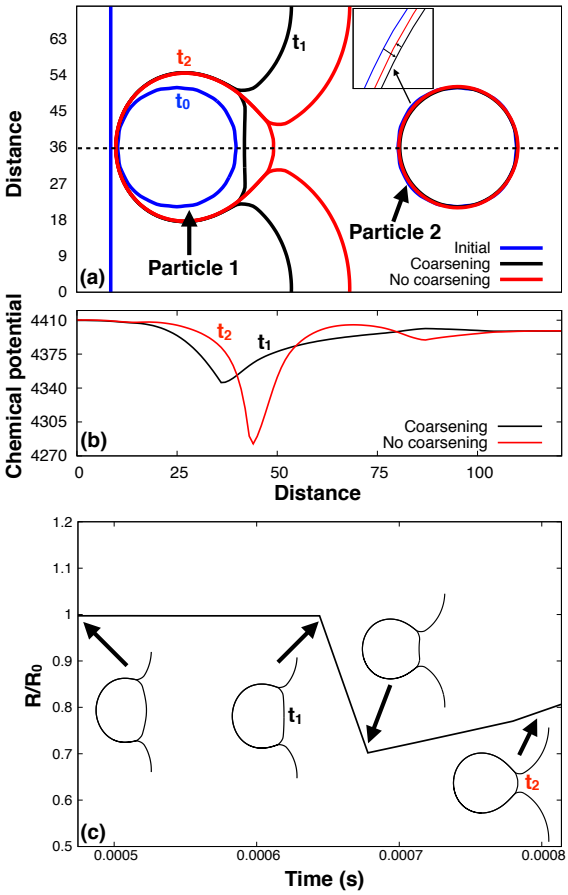

Figure 6.4.: (a) Phase contours showing the subsequent shrinkage and growth of particle 2 as the α/γ front advances. (b) 1-D chemical potential profiles plotted along the dashed line in (a) which shows a deviation in the carbon redistribution mechanism during temporal evolution (as seen at $t_1 = 6.44\times10^{-4}$ seconds and $t_2 = 7.79\times10^{-4}$ seconds). (c) Temporal evolution of the scaled radius (R/R_0) of particle 2 illustrating sharp deviations in the trend. The corresponding contours of particle 1 are also plotted along side at different time-steps which explains how the temporal change in curvature of θ/γ interface of particle 1 results in the onset of growth and coarsening regimes respectively.

prior to the divorce from the growth front.

To begin with, the α/γ transformation front advances and forms an interface with the adjacent cementite particle 1. As a result of this interaction, particle 1 starts to grow due to the incorporation of partitioned carbon primarily via the interface (transformation front) diffusion flux. It is noteworthy, that the particle 1 which shares a common interface with ferrite experiences a greater influx of partitioned carbon as compared to particle 2, since the interface diffusivity is assumed to be 1000 times faster than the diffusion in austenite in all the present cases. As the diffusion fields of both the cementite particles overlap, particle 1 grows while the particle 2 shrinks, as shown in Figures 6.4(a) and 6.4(c). At this stage, the driving force for coarsening predominates over the growth. The same is also reflected [Figure 6.4(a)] by a temporal increase in the curvature of θ/γ interface of particle 1 which slowly approaches infinity and subsequently curves inwards. An advancement of α/γ transformation front towards particle 2 causes a shift in the carbon redistribution mechanism again; the driving force for cementite growth exceeds coarsening. I attribute this to a reduction in the distance between α/γ transformation front and particle 2, which makes the incorporation of partitioned carbon feasible at smaller distances via bulk diffusion flux. As a result, the chemical potential near the advancing α/γ front ascends leading to the growth of particle 2. This change in the carbon redistribution mechanism which results in predominance of growth over a coarsening regime is evident from the 1-D plot shown in Figure 6.4(b) [2].

It is worth clarifying that the “concurrent growth and coarsening" regime (denoted by ‘C’) reported in the present work principally differs from the particle coarsening in alloys which has been extensively reported in the literature [207–211]. Although, the reported regime ‘C’ does involve curvature driven coarsening of particles, the primary difference with the phenomena of conventional coarsening is attributed to the energetics of $\alpha/\theta/\gamma$ phase triple-junction which determines if the transformation proceeds by a cooperative (to yield lamellar pearlite) or by a non-cooperative regime (yielding divorced eutectoid). Further, the accompanying eutectoid transformation modifies the effective curvature of θ/γ interface of particle ‘A’ which increases the rate of coarsening as depicted by a decline in normalized radius of particle ’B’ shown in Figure 6.4(b). It can be argued that the reported regime holds a close resemblance with the discontinuous coarsening of grain boundary precipitates which could result in the formation of precipitate free zone (PFZ) along prior austenite grain boundaries [212]. However, on a careful examination, it is apparent that the physics of temporally evolving interphase interfaces which is reported in the present study is not only different, but also more complex when compared to the grain boundary interfaces involved in discontinuous coarsening [3].

[2] The preceding paragraph written by K.A. is based upon a discussion with T.M., R.M. and B.N. which facilitated in speedy interpretation of results.

[3] This paragraph written in the words of K.A. is based upon a discussion with R.M.

6.3. Lamellar-Divorced-Coarsening map (LDC)

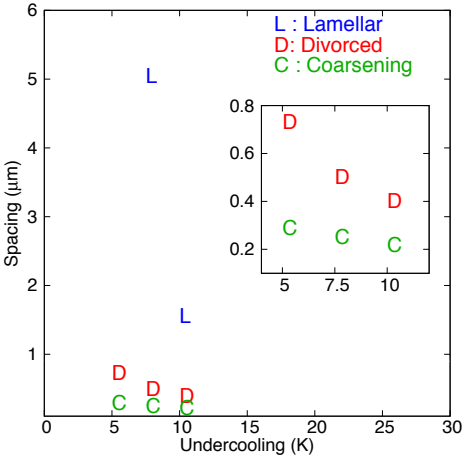

Figure 6.5.: A morphological transition map showing the predominance of lamellar (L), divorced (D) and concurrent growth and coarsening (C) modes during the eutectoid transformation in Fe-C alloy system. The initial spacing between the cementite particles (at the intercritical temperature) as well as the undercooling below the A_1 temperature govern the switching among the three numerically simulated modes.

Having numerically simulated and comprehended the ipseity of the concurrent growth and coarsening regime which precedes the non-cooperative eutectoid transformation, I construct a Lamellar-Divorced-Coarsening (LDC) transition map as shown in Figure 6.5 to summarize the parametric study. The LDC transition map generated by conducting phase-field simulations for three different undercoolings (5, 7.5 and 10 K) below the eutectoid temperature and initial particle spacings predicts the morphology that is favored for a given set of initial conditions during an isothermal transformation. In a nut-shell, the most significant contribution of the work presented in the current letter is the addition of an alphabet 'C' (acronym for concurrent growth and coarsening regime which is favored at smaller spacing and lower undercooling) to the classical Lamellar-Divorced (LD) map [99, 196]. Further, the present numerical findings are also in complete agreement with the existing theory for the divorced to lamellar morphological transition; lamellar morphology being more favorable at large spacings and high undercooling.

6.4. Discussion and outlook

The spacing of the cementite particles embedded in the austenite matrix as well as undercooling below the eutectoid temperature entirely determines the final microstructure. An in-depth phase-field study of the isothermal transformation presented in this chapter, aids in selection of parameters to tailor the eutectoid microstructure appropriately. The present approach also captures the important transition between lamellar and divorced morphologies and sheds light on the change in carbon redistribution mechanism which is primarily governed by initial configuration of the phases. The concurrent growth and coarsening regime is identified for the first time which may be fundamentally difficult to isolate in experiments. Thus, the present numerical studies provide new insights into the transformation mechanism and amend the classical model of eutectoid transformation.

In the following chapters, a detailed study on the influence of asymmetrical arrangement of cementite particles on the final eutectoid morphologies is presented. Large-scale numerical studies of the divorced eutectoid transformation for a random distribution of particles is also conducted to facilitate a direct comparison with the experimental microstructures.

7. Mixed cementite morphologies

The influence of curvature-driven coarsening is more pronounced, as the transformation proceeds from a random spatial arrangement of θ particles. In the following chapter, I report a detailed parametric study of the non-cooperative eutectoid transformation, which proceeds from random arrangement of preexisting θ particles. This chapter was published in [7].

7.1. Amending the governing criteria

The multiphase-field model that is used to study the non-cooperative evolution in Fe-C binary alloys is already discussed in an earlier chapter of this thesis. The reader is referred to previous studies [2, 5, 6, 215, 216] for a detailed description.

In the present section, I investigate the influence of introducing a third particle at an equivalent spacing ($\lambda = 0.252\mu$m), on the coarsening kinetics, starting from a symmetrical arrangement of cementite. In Figure 7.1, I plot the numerically simulated coarsening rate of the boxed particle (second from left), as the transformation proceeds, starting from a symmetric arrangement of 2 and 3 θ particles respectively. During the early stages of transformation, the coarsening rates observed in both the cases are identical. As the α/γ transformation front evolves non-cooperatively, the second particle shrinks due to the onset of a curvature-driven coarsening regime, discussed previously [6]. By virtue of a decrease in the effective curvature, the shrinking rate of the second particle is accelerated by the soft-impingement (overlap of the carbon concentration field with the third particle). Apparently, the accelerated coarsening regime that I report in the present study is dependent on the distribution of θ, ahead of the advancing transformation front and not feasible unless 3 or more preexisting particles are considered for numerical studies.

In Figure 7.2(a), I plot the phase isolevels at representative time-steps, as the eutectoid transformation proceeds from a preexisting symmetric arrangement of 3 θ particles. As the α/γ transformation front temporally advances, concurrent shrinking of the second and ripening of the third particle is observed. Meanwhile, the α/γ transformation front continues to evolve non-cooperatively by pulling away from the first θ particle. The chemical potential profile (1D) as plotted along the dotted line in Figure 7.2(b), suggests a strong carbon diffusion flux, originating from the center of second particle. The transport of carbon by volume diffusion towards particles on either side provides a

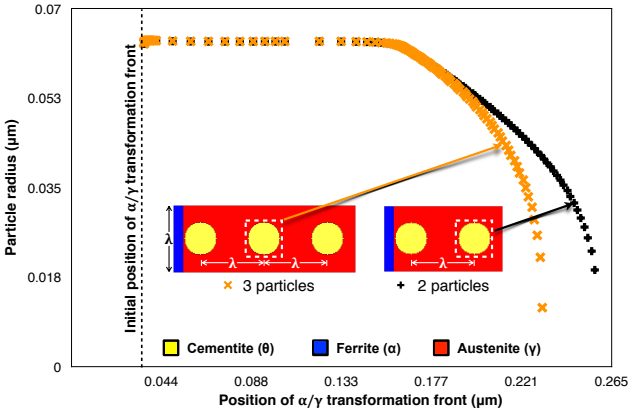

Figure 7.1.: Comparison of the numerically simulated coarsening rate of the boxed cementite during an isothermal eutectoid transformation ($\Delta T = 7.5K$) starting from a symmetrical arrangement of 2 and 3 preexisting particles ($\lambda = 0.252\,\mu m$).

plausible mechanism for an observed overlap of non-cooperative and coarsening regimes. A closer examination of the temporal change in radius of the third particle (Figure 7.2(c)) suggests that the non-cooperative and coarsening regimes overlap in the early stages i.e. as the second particle shrinks, and in succession, once it disappears.

7.2. Simulation parameters

The simulation parameters used for the present study are summarized in Table 8.1, in their dimensional form. Since, I am primarily interested in generic features of non-cooperative eutectoid transformation, the reported times are normalized by ${l_0}^2/D^{\gamma}$, where $l_0 = \sigma/(RT/v_m)$ is the capillary length.

The size of the computational domain is chosen to be 433×500 grid points, where the grid spacings in the x and y directions (Δx and Δy) are equal to the lattice constant ($0.0042\,\mu m$). Hence, the size of the domain is estimated to be $1.81\,\mu m \times 2.10\,\mu m$. The initial condition, which comprises of a random distribution of preexisting cementite (θ) particles embedded in austenite (γ), is constructed using an algorithm which fills the numerical domain with spheres of diameter 'd_0'. By varying λ_{min} (the shortest distance between the two neighboring particles), I generate different particle distributions. A thin layer of ferrite (α) is embedded at the bottom of the numerical domain. No-flux and periodic boundary conditions are imposed along the top-bottom (along the α/γ growth

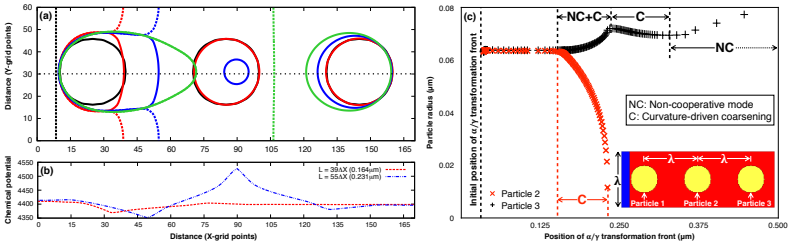

Figure 7.2.: (a) Temporal evolution of the isolevels $\phi_\alpha = 0.5$ (dashed lines representing the α/γ interface) and $\phi_\theta = 0.5$ (solid lines representing θ/γ and θ/α interfaces) during the isothermal eutectoid transformation ($\Delta T = 7.5K$), which starts from a symmetrical arrangement of 3 cementite particles ($\lambda = 0.252\ \mu m$). (b) 1-D chemical potential profile plotted at two representative time-steps along the dotted-line in Figure 7.2(a) that connect the centers of the 3 cementite particles. During the early stages, the carbon partitioned at α/γ transformation front is incorporated in all the particles. As the α/γ transformation front advances, larger amount of carbon partitions preferably at the θ/γ interface of the second particle, which results in accelerated curvature-driven coarsening. (c) Comparison between the coarsening rate of the second and third particle, as the α/γ transformation front advance towards right-hand side of the computational domain.

direction) and left-right (perpendicular to the α/γ advancing transformation front) edges of the numerical domain, respectively.

7.3. Influence of minimum interparticle spacing (λ_{min})

Figure 7.3[1] illustrate the temporal evolution of eutectoid phases during an isothermal transformation ($\Delta T = 7.5$ K), starting from three different λ_{min}. As the transformation proceeds, the preexisting θ particles, ahead of the advancing α/γ transformation front grow or shrink, depending upon the local carbon redistribution mechanism. As the advancing α/γ transformation front sweeps across the computational domain, the local carbon redistribution is strongly influenced by the energetics of the $\alpha/\theta/\gamma$ phase tri-junction as well as soft impingement, causing temporal shifts between non-cooperative and coarsening regimes. I prefer to call such an apparent overlap between the observed curvature-driven particle coarsening and pulling away of the advancing α/γ transformation front from

[1]The numerical simulation jobs (submitted on computer cluster by K.A) were jointly administered by all the co-authors. T.M. ensured timely re-spawn of computational jobs. The illustrated plot was prepared by K.A.

Table 7.1.: Numerical parameters used for the phase-field simulation of eutectoid transformation starting from a random distribution of cementite particles ('λ_{min}' denotes minimum interparticle distance) with an initial diameter 'd_0'. T_E denotes the eutectoid transformation temperature of a binary Fe-C alloy, ΔT, the undercooling (below the A_1 temperature) and σ, surface energies (pairwise). D^{α}, D^{θ} and D^{γ} represents volume diffusivity in ferrite (α), cementite (θ) and austenite (γ), whereas $D^{\alpha\gamma}$, $D^{\alpha\theta}$ and $D^{\theta\gamma}$ represent diffusivity along the corresponding transformation fronts.

Symbol	Value	Units
T_E	999	K
ΔT	5, 7.5, 10	K
$\sigma_{\alpha\gamma} = \sigma_{\theta\gamma} = \sigma_{\alpha\theta}$	0.49	J/m^2
$D^{\alpha} = D^{\theta}$	2×10^{-9}	m^2/s
D^{γ}	1×10^{-9}	m^2/s
$D^{\alpha\gamma} = D^{\alpha\theta} = D^{\theta\gamma}$	$1000D^{\alpha}$	m^2/s
λ_{min}	0.21, 0.252, 0.315	μm
d_0	0.063	μm

θ as a mixed-mode regime. Due to a complete disappearance of θ particles ahead of the growth front as the transformation approaches completion, onset of the cooperative growth mode is observed. The distinct reversal in the carbon redistribution mechanism is indicated by the evolution of non-spheroidized θ particles in all the three test cases, as the advancing α/γ transformation front traverses across to reach the upper edge of the computational domain.

The particle size distribution that are plotted at representative time steps in Figure 7.4, reveal interesting trends. Starting from a smaller initial interparticle spacing ($\lambda_{min} = 0.21\,\mu$m), a particle size distribution with two well defined peaks is obtained during the early stages of the transformation. As the transformation proceeds, the difference between the two peak values reduce and ultimately, they merge forming a unique peak, as the advancing α/γ front reaches the upper edge of the numerical domain. A temporal shift of the peak value towards right is also observed. A similar trend is observed, if the initial interparticle spacing is chosen slightly larger ($\lambda_{min} = 0.252\,\mu$m), as shown in Figure 7.4(b). On further increasing the initial interparticle spacing to $0.315\,\mu$m, a size distribution with two well-defined peaks of equal height are obtained during the final stages of transformation, as shown in Figure 7.4(c). The final θ size distribution in the transformed microstructure, simulated by choosing three different values of λ_{min} ($0.210, 0.252$ and $0.315\,\mu$m) are plotted in Figure 7.5. The multimodal size distribution obtained for larger value of λ_{min} ($0.315\,\mu$m) indicate an overlap of cooperative, non-cooperative and coarsening regimes, as the eutectoid transformation proceeds.

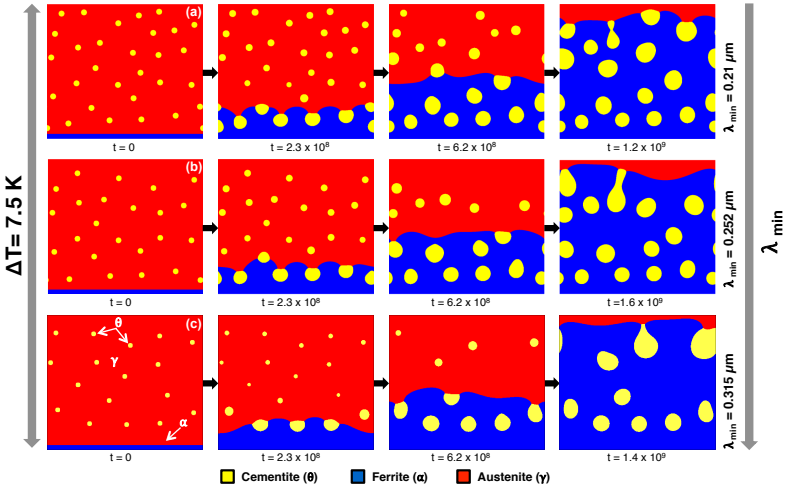

Figure 7.3.: Phase-field simulations illustrating the temporal evolution of the eutectoid phases during an isothermal transformation at an undercooling of 7.5 K below the A_1 temperature. The initial condition comprises of a thin ferritic (α) layer and random distribution of θ particles , embedded in the γ matrix at minimum interparticle spacings (λ_{min}) of (a) 0.21 μm (b) 0.252 μm and (c) 0.315 μm.

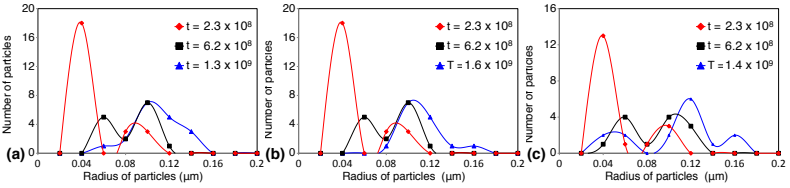

Figure 7.4.: Temporal evolution of the corresponding size distribution of θ particles, plotted at representative times for three different minimum interparticle spacings (λ_{min}) of (a) 0.21 μm (b) 0.252 μm and (c) 0.315 μm. The plots suggest that a bimodal size distribution is favorable at larger λ_{min}.

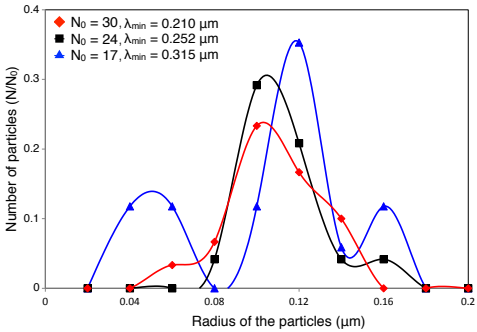

Figure 7.5.: Normalized size distribution of θ particles in the transformed microstructure, starting from different λ_{min}. A multimodal size distribution of θ particles in the final microstructure is obtained if $\lambda_{min} = 0.315\,\mu$m (where $N_0 = 17$ denote the number of particles at the start of transformation). On the contrary, unique size distribution peaks are obtained at lower λ_{min}. The above plots are generated by analyzing the isothermally transformed eutectoid microstructures at an undercooling of 7.5 K.

7.4. Influence of arrangement

The classical theory of non-cooperative eutectoid transformation [99, 190, 196] states that the transition from cooperative to non-cooperative evolution of the α/γ front, during an isothermal eutectoid transformation is governed by interparticle spacing and undercooling (below A_1 temperature). However, the onset of curvature-driven coarsening regime, which is discussed in my earlier work [6], necessitates an extension of the proposed criteria. From a technological perspective, it needs to be ascertained, if there are any other factors apart from interparticle spacing and undercooling that may influence the evolution kinetics as well as the θ size distribution in the transformed microstructure.

In the present section, I numerically simulate and analyze the temporal evolution of the eutectoid microstructure, starting from three different preexisting arrangements of θ particles. In order to decompose the influence of different initial arrangement of θ on the complex spatial and temporal evolution pathways, I assume the same initial interparticle spacing ($0.315\,\mu$m) and undercooling ($\Delta T = 7.5$ K below A_1 temperature), for the three numerical test cases. According to the established theories [99, 190, 196], the carbon redistribution mechanism during the temporal evolution is determined by the configuration of preexisting θ particles ahead of the advancing transformation front. As shown in Figure 7.6(a), the number of θ particles ahead of the α/γ front decrease as the transformation proceeds due to curvature-driven coarsening. A comparison of simulated

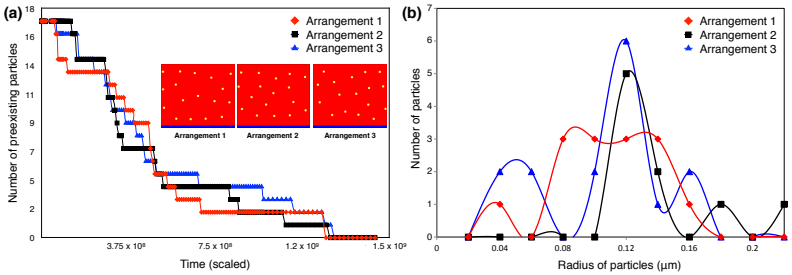

Figure 7.6.: Phase-field simulations of isothermal eutectoid transformation ($\Delta T = 7.5$ K) are conducted starting from different initial arrangements of θ particles (embedded in γ) but same λ_{min} (0.315 μm). (a) Plot showing the temporal decrease in the number of preexisting θ particles, as the transformation proceeds from three different initial arrangements. (b) Corresponding size distributions of θ in the transformed microstructure.

trends suggest that the time elapsed before the number of preexisting particle falls to zero, is equal for the three arrangements. However, as the particle depletion trends do not overlap, it can be argued that the spatial arrangement and size of θ particles in the transformed microstructure may depend of their preexisting configuration.

My present assertion is validated by comparing the θ size distribution in the transformed microstructure for the three numerical test cases, as shown in Figure 7.6(b). For arrangement 1, the size distribution comprise of two equivalent peaks. However, a bimodal and a trimodal size distribution is obtained for the transformations starting from arrangements 2 and 3, respectively. Thus, the present numerical results suggest that the preexisting arrangement of θ particles in γ influence the intermittent carbon redistribution that ultimately results in variable size distribution profiles in the transformed microstructures.

7.5. Influence of undercooling - A revisit

The influence of undercooling in facilitating a transition from the non-cooperative mode (resulting in divorced eutectoid) to cooperative (formation of pearlitic lamellae) is well-known [6, 99, 190, 196]. In my ongoing quest to generalize the governing criteria of non-cooperative eutectoid transformation for a random distribution of preexisting θ particles, I numerically re-investigate the influence of undercooling on the mechanism, by which, the advancing α/γ transformation front evolves. In Figure 7.7(a)-(c), I show the representative microstructures simulated at three different undercoolings (ΔT = 5, 7.5 and 10 K, below

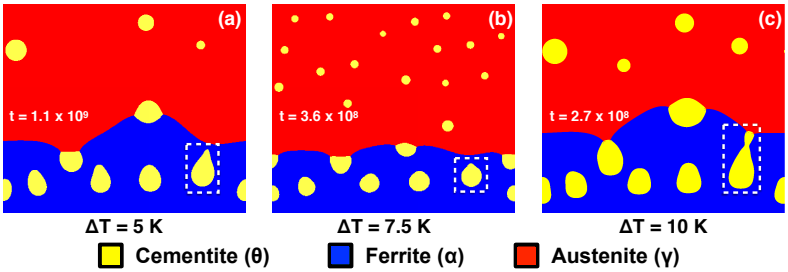

Figure 7.7.: The representative microstructures (taken at different times) depict the influence of increasing the undercooling on the eutectoid transformation mode, starting from equal minimum interparticle spacing ($\lambda_{min} = 0.21\ \mu$m) and identical arrangement of θ. (a) At $\Delta T = 5$ K, the advancing α/γ transformation front evolves non-cooperatively and divorces the boxed particle. (b) A similar transformation mode is observed for $\Delta T = 7.5$ K, however, the boxed particle is more rounded as compared to Figure 7.7(a). (c) At $\Delta T = 10$K, the boxed θ particle evolves cooperatively with the α/γ front. A careful analysis of the representative microstructures (taken at different times) reveal that the mode of transformation is implicitly related to undercooling as well as number of preexisting particles ahead of the growth front, at a given time.

A_1 temperature). The initial configuration of eutectoid phases ($\lambda_{min} = 0.21\ \mu$m) are assumed to be identical for the three numerical test cases. On comparing the simulated microstructures, it is apparent that the advancing α/γ transformation front pulls away from the interface of the boxed θ particle and the divorce eventually occurs, if the undercooling is small ($\Delta T = 5$ K). The morphology of the divorced cementite particle, illustrated by the white box in Figure 7.7(a), is found to be tapered along the path of advancing α/γ transformation front. The curvature-driven coarsening, which results in a steep decline of preexisting particles implicitly regulates the temporally evolving carbon redistribution mechanism ahead of the growth front. Given the concurrent formation of 'cementite-free' patches ahead of the growth front as well as a non-spherical morphology of the boxed particle, I am convinced that the cooperative regime, although for an infinitesimal duration, must have set in at an intermittent stage.

At a larger undercooling ($\Delta T = 10$K), the boxed particle evolves cooperatively (Figure 7.7(c)). On the contrary, the boxed cementite particle that is divorced by the advancing α/γ front appears to be comparatively, more spheroidized, as the transformation proceeds at $\Delta T = 7.5$ K (Figure 7.7(b)). At this point, it is worth noting that the velocity of the advancing α/γ transformation front, which is directly proportional to ΔT, determines the transformation time. As the extent of particle coarsening is dependent on the transformation time, I attribute the reason for an observed non-cooperative evolution

mode to be the higher density of preexisting particles, ahead of the advancing α/γ transformation front[2].

The temporal evolution of θ volume fraction, plotted in Figure 7.8 at different undercoolings (5, 7.5 and 10 K), provides a fair idea of the average carbon partitioning rate A

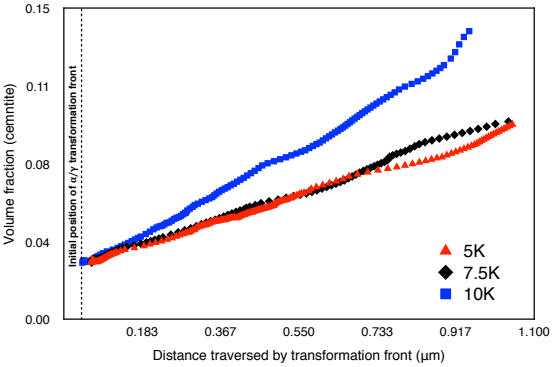

Figure 7.8.: Comparison of the temporally evolving cementite volume fraction during an isothermal eutectoid transformation at three different undercoolings ($\Delta T = 5, 7.5$ and 10 K). The initial configuration of eutectoid phases is chosen to be identical for the three test cases. ($\lambda_{min} = 0.315\ \mu$m).

larger amount of carbon partitioning observed at $\Delta T = 10$ K suggest that the particle fineness in the transformed microstructure is inversely related to undercooling.

7.6. Discussion and outlook

An extension of the governing criteria that controls the transition between cooperative, non-cooperative and coarsening regimes during the eutectoid transformation, starting from a random distribution of preexisting cementite particles, is proposed. A bimodal size distribution of cementite that is obtained by numerically post-processing the simulated microstructure, is in general agreement with the previous experimental findings [197, 213]. By conducting a systematic parametric study, I demonstrate that a multimodal size distribution in the transformed microstructure is essentially, an inherent characteristic of a eutectoid transformation that proceeds in the mixed-mode. The complex nature of the eutectoid transformation is depicted by the overlapping modes that have been

[2]The preceding paragraph written by K.A. is based upon a discussion with T.M., R.M. and B.N. which facilitated speedy interpretation of results.

numerically simulated for the first time. Further, by conducting an extensive parametric study, I explain the mechanisms by which mixed θ morphologies (spheroidal as well as non-spheroidal), evolve. I believe that the in-depth analysis of the influence of arrangement and spacing of preexisting θ as well as undercooling that has been reported in the present study, will aid in selection of parameters to tailor the eutectoid microstructure, appropriately.

It is worth mentioning that the influence of prior austenite grain boundaries on the transformed microstructure need to be investigated. A detailed study is presented in the next chapter. Although, the present numerical study provides valuable insights into the rich behavior that is exhibited during the eutectoid transformation in binary Fe–C alloy, the applied phase-field method needs to be extended to account for the diffusion of substitutional alloying elements.

8. Mechanisms of non-cooperative eutectoid transformation in polycrystalline austenite

In this final chapter of Part A, I investigate the influence of preexisting asymmetric arrangement of θ, prior γ grain boundaries and morphology of α layers on the temporal evolution of the divorced eutectoid microstructure. A reasonable agreement between the numerically simulated and experimental microstructures is also established. This chapter was published in [8].

8.1. Influence of Arrangement

As the generic features of non-cooperative eutectoid transformation is of primary interest, the reported times are normalized by ${l_0}^2/D^\gamma$, where $l_0 = \sigma/\left(RT/v_m\right)$ is the capillary length and D^γ is the diffusivity in austenite (γ). T, R and v_m denote transformation temperature, universal gas constant and the molar volume respectively. The numerical parameters used in the reported simulations are listed in Table 8.1.

8.1.1. Divorced-Coarsening transition in asymmetric arrangement

According to the classical theory of non-cooperative eutectoid transformation [196], interparticle spacing (λ) and undercooling (below A_1 temperature) determine whether transformation proceeds in a cooperative manner or the advancing α/γ front divorce the θ particles. In the present section, I build upon the results reported in chapter 6 and extend the numerical studies to investigate the influence of preexisting arrangement of θ particles on the non-cooperative evolution of the α/γ transformation front.

In Figure 8.1(a), one can compare the coarsening kinetics, as the transformation proceeds from a preexisting symmetric and asymmetric arrangements of two θ particles. The evolution of the chemical potential and phase contours at representative times are shown for the two cases in Figure 8.1(b) and 8.1c, respectively. It is observed that the boxed particle (shown by the schematic diagram in Figure 8.1(a)) when placed at the symmetric position, shrinks at a faster rate, as compared to the latter. One may argue that the coarsening kinetics is expected to be much faster for the case of asymmetric arrangement,

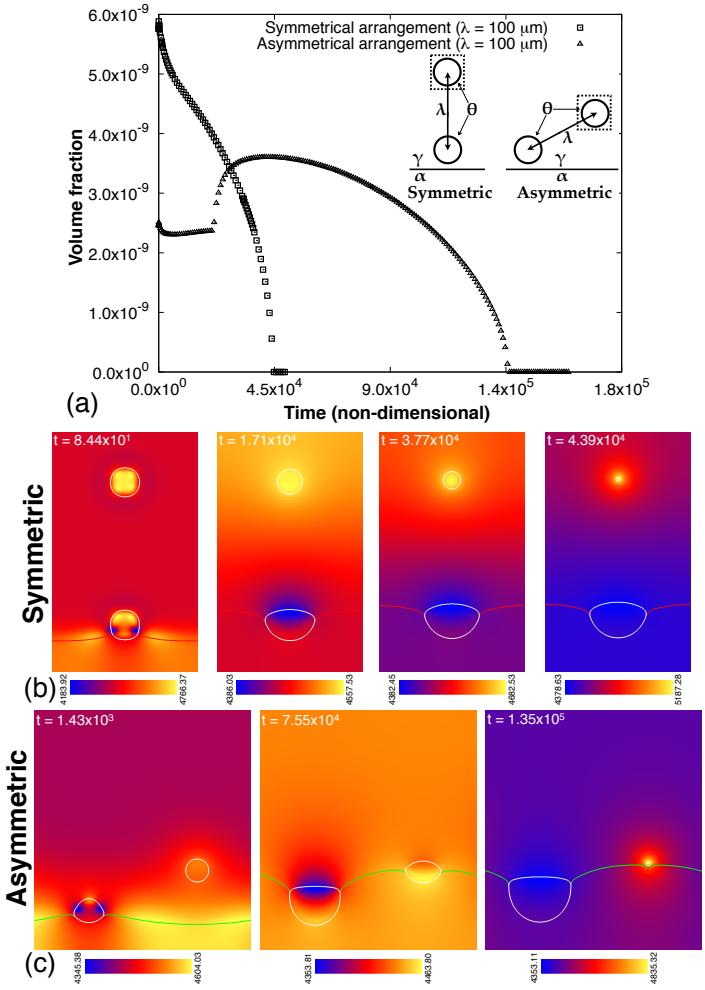

Figure 8.1.: (a) Temporal change in the volume fraction of the boxed θ particle, as the α/γ transformation front advances starting from a two different arrangements (symmetric and asymmetric). Corresponding evolution of the phase contours plotted over the chemical potential maps, as the transformation proceeds from (b) symmetric and (c) asymmetric arrangements.

rather than the symmetric due to assistance from α/γ interface diffusive flux (which is stronger than the volume diffusion flux) during the intermediate stages of the eutectoid transformation, as seen in Figure 8.1(c) (at $t = 7.55 \times 10^{-4}$). On the contrary, as the transformation proceeds from a symmetric arrangement, due to geometric considerations and the chosen value of λ, the advancing α/γ front does not get a chance to form an interface with the shrinking θ particle, as clearly seen in the temporally evolving phase contours in Figure 8.1(b). Therefore, any assistance from α/γ interface diffusion can be completely ruled out. Apparently, the question arises: In spite of availability of a faster diffusion path along the α/γ interface, why is the coarsening rate slower when the isothermal eutectoid transformation proceeds from an asymmetric arrangement of preexisting θ particles? The answer lies in analyzing the difference between the mean curvatures of the two θ particles for the respective cases. Once the advancing α/γ front forms an interface with the asymmetrically placed θ particle, it continues to shrink in a *lenticular* morphology. This essentially means that the curvature difference between the θ/γ or θ/α interfaces of the two particles depreciate, thereby, slowing down the curvature-driven coarsening rate. On the contrary, when the eutectoid transformation proceeds from a symmetric arrangement, the temporally shrinking particle retains the spheroidal morphology. On analyzing the temporal evolution of phases for both the cases (symmetric and asymmetric arrangements), it is apparent that the difference in curvatures of θ/γ or θ/α interfaces of the two particles are greater when the shrinking particle retains the spheroidal morphology i.e. when symmetrically located with respect to the θ particle closer to α/γ front.

Figure 8.2 shows the influence of interparticle spacing (λ) as the eutectoid transformation proceeds isothermally from asymmetric arrangement of preexisting θ particles (undercooling, $\Delta T = 10$K below A_1 temperature). The results of the numerical simulations are illustrated for two different interparticle spacings ($\lambda_{co} = 0.26\,\mu m$ and $\lambda_d = 0.57\,\mu m$). Starting from the initial configuration of phases. which comprise of asymmetrically arranged particles, the α/γ transformation front advances to form an interface with the θ phase. When the chosen λ is small ($\lambda_{co} = 0.26\,\mu m$), the particles nearer to the preexisting α/γ transformation front (at odd positions), ripen while the ones farther (even position), shrink. As the eutectoid transformation proceeds, the θ particles at even positions shrink and ultimately, dissolve. On analyzing the simulated chemical potential profile, one can observe the carbon diffusion flux along the α/γ transformation front, directed towards the θ particles that are located at odd position positions. However, if the λ is increased ($\lambda_d = 0.57\,\mu m$), coarsening of θ is less pronounced and the transformation proceeds predominantly, in the non-cooperative mode. For even larger λ, curvature-driven coarsening of θ is not observed. It is worth noting that the criterion of divorced-coarsening transition regime reported earlier holds for the case of asymmetric arrangements as well. However, the rate of coarsening, which influences the final microstructure, is dependent on the relative arrangement of preexisting θ particles.

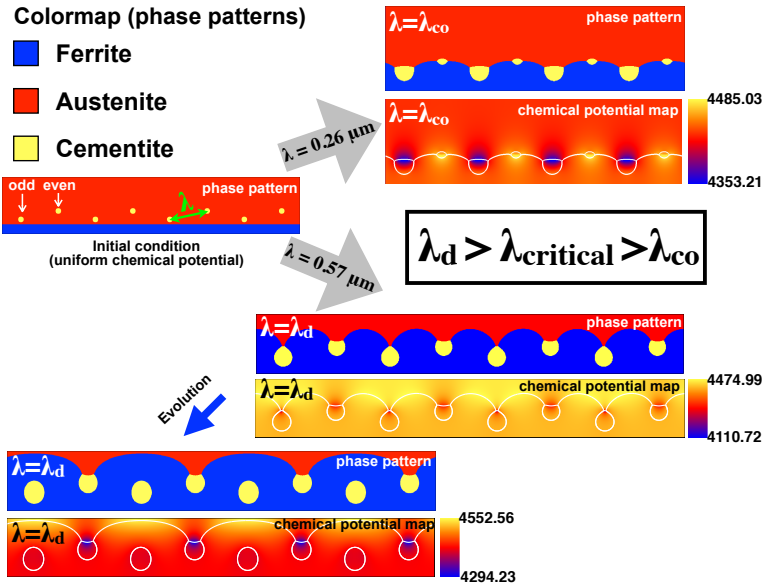

Figure 8.2.: Phase-field simulations showing the influence of λ as the eutectoid transformation proceeds isothermally from a preexisting asymmetric arrangement of θ particles ($\Delta T = 10$K). The phase contours are plotted on the corresponding chemical potential maps. At smaller λ ($\lambda_{co} = 0.26\,\mu m$), onset of curvature-driven coarsening result in dissolution of θ particle, marked at even positions. However, at larger λ ($\lambda_d = 0.57\,\mu m$), the eutectoid transformation predominantly proceeds in non-cooperative mode.

8.1.2. Mixed transformation products

It is typical to observe the non-spherical θ particles co-existing with the spherical/well-rounded ones in a transformed eutectoid microstructure. As the presence of non-spheroidized θ has an adverse effect on the machinability of steel, it is essential to establish the conditions of growth and process parameters which prevent the formation of non-spheroidized counterparts.

In Figure 8.3, I present the phase-field simulation results to demonstrate the influence of preexisting θ particle in bringing about a shift from co-operative to non-cooperative evolution mode. For the case of single-layered arrangement, the preexisting particles that

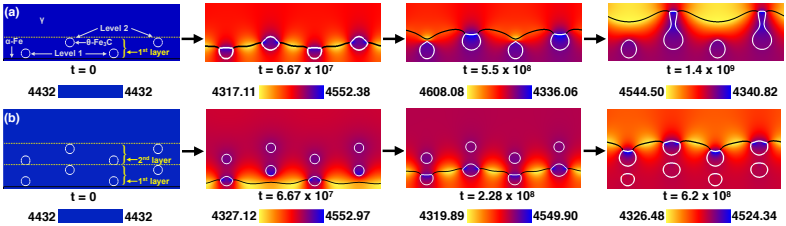

Figure 8.3.: Temporal evolution of phase isolines ($\phi = 0.5$) and the corresponding chemical potential map for an asymmetric (a) single-layered and (b) bi-layered arrangement of θ particles (initial spacing, $\lambda = 0.84\mu m$), during an isothermal eutectoid transformation (undercooling, $\Delta T = 7.5$K). The isolines plotted over the chemical potential map illustrate the corresponding sharp interfaces of the phases. Black lines correspond to α/γ interface while the white lines represent θ/α and θ/γ interfaces.

are nearer to the α/γ transformation front, evolve non-cooperatively yielding a divorced eutectoid morphology. As the transformation front temporally evolves to form an interface with the farther set of particles, it pulls away and divorces the θ particles in Level 1, as illustrated in the in Figure 8.3(a). Owing to an absence of any θ particles ahead of the growth front, the transformation proceeds further in a cooperative mode. The apparent shift in the transformation mode (i.e. cooperative to non-cooperative) results in the evolution of lamellar/non-spheroidized eutectoid morphology (at t $= 5.01 \times 10^{-3}$s). On the contrary, when the transformation starts with a bi-layered arrangement of preexisting θ particles (shown in Figure 8.3(b)), a shift in the carbon redistribution mechanism is not observed. The temporally advancing α/γ transformation front continues to pull-away from the θ particles in Level 2 (in the first layer), which ultimately result in the formation of divorced eutectoid. Apparently, the present simulations suggest that the presence of preexisting θ particles ahead of the growth front (in second layer) favor the non-cooperative evolution of the growth front.

8.2. Non-cooperative eutectoid transformation in polycrystalline austenite

8.2.1. Influence of preexisting α thickness ($\mathcal{L}$) and configuration of θ particles

Polycrystalline γ is modeled as an array of four hexagonal grains in a two-dimensional simulation domain with periodic boundary conditions. As the preexisting γ grains are

chosen to be equiaxed and of the same size, the ratio of the width (N_x grid-points) and height (N_y grid-points) of the numerical domain is restricted to $\sqrt{3}:2$. This implies that a circle of radius 'r' which circumscribes the central grain relate to the numerical domain width as, $N_x = 3r$ (or $N_y = 2\sqrt{3}r$). For the present simulations, a computational box size of 500×433 grid-points is chosen, where the grid-spacings in the x and y directions (Δx and Δy respectively) are equal to 0.0042 μm. Therefore, the present choice of numerical domain size implies a γ grain size ($2r$) that is equal to 1.2 μm. The four γ grains in consideration are assigned distinct phase-fields and uniform equilibrium composition that is derived from the phase diagram. A spatial distribution of 'N_0' spherical θ particles (initial radii equal to 8 grid-points) is algorithmically generated by using a numerical pre-processing technique. The minimum distance between two particles is constrained to be greater than $\lambda_{min} \pm \xi$ grid-points, where λ_{min} is the minimum inter-particle spacing and ξ is a random noise between 0 and 10 grid-points. The pre-processing algorithm iteratively fills the spherical particles inside the domain as per the imposed minimum inter-particle spacing (λ_{min}) criteria. Following every successful incorporation of a new particle in the numerical domain, the algorithm performs a number of iterations (lesser than the predefined maximum designated by i_{max}) to search for a suitable coordinate of the next particle that is to be added. For a limiting case, when the introduction of new particles is no longer possible for the chosen i_{max}, the iteration exits. The maximum possible number of iterations (i_{max}) following every successful particle filling is chosen to be high enough to ensure that the algorithmically generated particle distribution is homogeneous. Finally, a layer of α (of uniform thickness '$\mathcal{L}$') is placed along the γ grain boundaries and a parametric study is conducted by varying the simulation parameters as shown in Table 8.1.

Figures 8.4(a)-(e) and 8.4(f)-(j) show the temporal evolution of eutectoid phases staring from a polycrystalline configuration that is described above, for two different α layer thicknesses, $\mathcal{L} = 0.0336$ and 0.1 μm, respectively. Assuming other simulation parameters to be constant, numerical simulations are also carried out for intermittent thicknesses (0.0504 and 0.084 μm), to study the influence of initial grain boundary α layer thickness on the evolving as well as final eutectoid morphologies, in detail. It is observed that for a thickness of 0.0336 μm, the α layer that are in contact with cementite particle, pinch-off during the early stage of transformation and forms an island morphology to minimize the surface energy (Figure 8.4(b)). Once the pinching-off stops, the α/γ begins to temporally advance (Figure 8.4(c)), in a predominantly non-cooperative mode. In the time elapsed (during the α layer pinch-off), the count of preexisting θ particles plummets down as a result of curvature driven coarsening (the phenomena is discussed in the detail in previous chapters) which subsequently, lead to a cooperative growth of the α/γ front during the final stages of eutectoid transformation (Figure 8.4(e)). It is noteworthy that the α pinching-off is not observed, if the initial α layer thickness is assumed to larger (Figure 8.4(f)-(g)). By conducting a parameter study, it is observed that the coarsening of the preexisting θ particles is comparatively less, if $\mathcal{L} > 0.0336\,\mu m$. Apparently, the numerical simulations suggest that the pinching-off of grain boundary α-layer is strongly dependent on the surface energies and ceases once the equilibrium phase triple-junction

Table 8.1.: Numerical parameters used for the phase-field simulation of eutectoid transformation starting from polycrystalline γ ('r' denotes grain radii) containing random distribution of θ particles ('λ_{min}' denotes minimum inter-particle distance) and grain boundary α layers (of uniform thickness '$\mathcal{L}$'). T_E denotes the eutectoid transformation temperature of a binary Fe-C alloy, ΔT, the undercooling (below the eutectoid temperature) and σ, surface energies (pairwise). D^{α}, D^{θ} and D^{γ} represents volume diffusivity in ferrite (α), cementite (θ) and austenite (γ), whereas $D^{\alpha\gamma}$, $D^{\alpha\theta}$ and $D^{\theta\gamma}$ represent diffusivites along the corresponding transformation fronts.

Symbol	Value	Units
T_E	999	K
ΔT	7.5	K
$\sigma_{\alpha\gamma} = \sigma_{\theta\gamma} = \sigma_{\alpha\theta}$	0.49	J/m^2
$D^{\alpha} = D^{\theta}$	2×10^{-9}	m^2/s
D^{γ}	1×10^{-9}	m^2/s
$D^{\alpha\gamma} = D^{\alpha\theta} = D^{\theta\gamma}$	$1000D^{\alpha}$	m^2/s
$\mathcal{L}$	0.1, 0.084, 0.0504, 0.0336	μm
λ_{min}	0.075, 0.084, 0.105, 0.147	μm
r	1.2	μm

angles develop.

The temporal evolution of θ volume fraction is plotted in Figure 8.5(a) starting from different initial thicknesses ($\mathcal{L}$) of grain boundary α layers. A significant deviation in the carbon redistribution mechanism is observed for the case of $\mathcal{L} = 0.0336$ μm, during the early stages of eutectoid transformation. Such a deviation can be attributed to curvature-driven coarsening regime, that is active during the α layer pinch-off (in early stages of eutectoid transformation) and causes a net carbon diffusion flux from the θ particles located near the grain center towards the α/γ front as they start advancing from the prior γ grain boundaries. Unarguably, for the case pertaining to $\mathcal{L} > 0.0336$ μm, the influence of particle coarsening in bringing about a change in the transformation mechanism, cannot be denied. Apparently, a temporal decline in the number of preexisting θ particles (located towards the grain center) is also observed in this case. It can be argued that the pinching-off of preexisting α layers that is observed in the present phase-field simulations is unrealistic from an experimental perspective. The result of the parametric study reported in Figure 8.5(a) allows us to identify the minimum threshold (numerical value of $\mathcal{L}$) below which, pinching-off occurs. To rule out such a possibility, I assume the α layer thickness to be sufficiently high ($\mathcal{L} = 5.04 \times 10^{-2} \mu$m) for all the numerical simulations, that follow.

In order to study the influence of arrangement and spacing of θ particles on the resulting microstructure, I numerically simulate the eutectoid transformation staring from different λ_{min} (minimum inter-particle spacing). The criteria for λ_{min} that is imposed by the

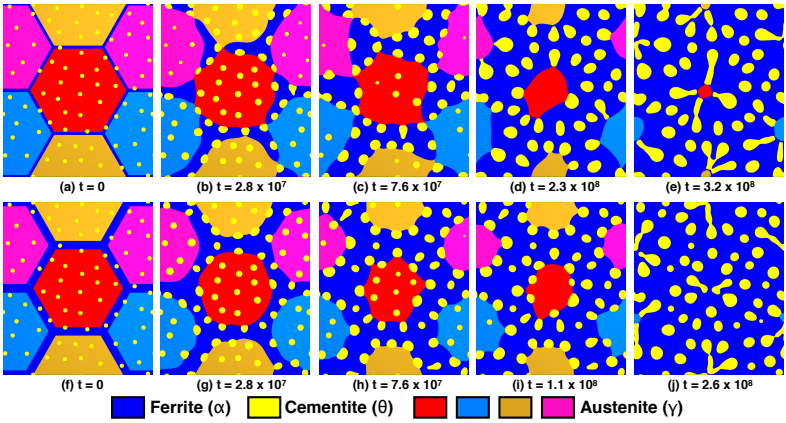

Figure 8.4.: Phase-field simulation showing the temporal evolution of the mixed eutectoid morphologies during an isothermal transformation ($\Delta T = 7.5$ K below A_1 temperature), starting from an initial configuration which comprise of grain boundary α layers of initial thickness $\mathcal{L}$ and θ particles that are randomly dispersed ($\lambda_{min} = 0.126\ \mu$m) in polycrystalline γ (grain diameter $= 1.2\ \mu$m). The effect of initial grain boundary α thickness on the temporal evolution of phases is observed in the present simulations. At a small thickness ($\mathcal{L} = 3.36 \times 10^{-2}\ \mu$m), the grain boundary α pinches-off from θ particles to minimize surface energy, at the early stages, as observed in (a)-(e). The temporal evolution shown in (f)-(j) suggests that α pinch-off do not take place at early stages, if the initial thickness is higher ($\mathcal{L} = 0.1\mu$m).

numerical pre-processing algorithm already described above, yields various distribution of θ particles (corresponding number of particles is designated as N_0). Figure 8.5(b) shows the θ size distribution obtained at the end of eutectoid transformation, by initializing numerical simulations with different number of particles (or λ_{min}). A comparison of the final θ size distribution suggests that the peak value decrease on increasing N_0 (or on decreasing λ_{min}). Due to an enhanced coarsening of θ particles at smaller λ_{min} (or larger N_0), the number of preexisting particles located towards the grain center decline temporally and subsequently, dissolve (in the later stages). As the transformation proceeds towards completion, due to a complete or near absence of preexisting θ particles, the α/γ transformation front starts to evolve co-operatively leading to the formation of elongated/bottle-shaped particles which are found to be pointing towards the grain center. The supple reversal of the transformation mode (non-cooperative to co-operative) that results in the formation of spheroidal as well as elongated/bottle-shaped particles,

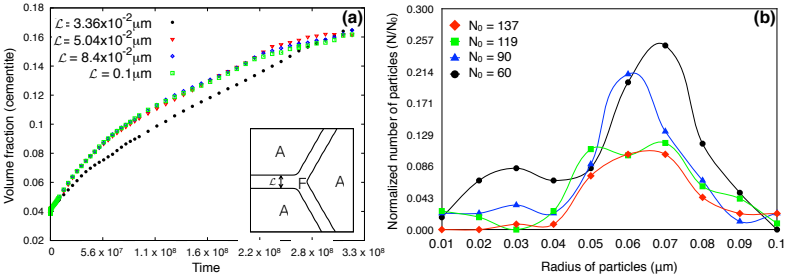

Figure 8.5.: (a) The plot showing the effect of initial thickness of grain boundary α layer ($\mathcal{L}$) on the temporal evolution of θ volume fraction. Pinching-off of α layers is observed at early stages (at $\mathcal{L} = 3.36 \times 10^{-2}$ μm) which results in a deviation from the trend observed for higher $\mathcal{L}$. (b) Starting with four different interparticle spacings, the eutectoid transformation is numerically simulated (λ_{min} = 0.075, 0.084, 0.105 and 0.147 μm) and the final particle distributions (obtained on completion of the phase transformation) are compared. For the sake of comparison, other simulation parameters such as grain size (1.2 μm), initial thickness of grain boundary α layers ($\mathcal{L} = 5.04 \times 10^{-2}$ μm) and undercooling (ΔT = 7.5 K below A_1 temperature) are kept constant for the four cases. A deviation from the bottle-shaped distribution profile is observed for $\lambda_{min} = 0.105$ μm ($N_0 = 119$) due to fragmentation of pearlitic lamellae.

explain the presence of more than one local maxima in the size distribution plots shown in Figure 8.5(b). It is noteworthy that the reported reversal in the transformation mode is not favored if the initial inter-particle spacing (λ_{min}) is large. The distribution plot pertaining to $N_0 = 90$ ($\lambda_{min} = 0.105$ μm) represents an intermediate case in which, non-cooperative as well as cooperative modes dominate during the early and later stages of the transformation respectively, as suggested by an absence of a unique distribution peak. These results essentially suggest that at smaller λ_{min}, curvature-driven coarsening predominates. Although the influence of coarsening is less pronounced at larger values of λ_{min}, the transformation for these cases proceed by a complex interplay of cooperative and non-cooperative modes, depending upon the local distribution of θ particles in the proximity of advancing α/γ front.

For a more detailed understanding, I analyze the temporal evolution of eutectoid phases starting from (a) $\lambda_{min} = 0.075$ μm and (b) $\lambda_{min} = 0.084$ μm, by plotting the corresponding particle size distribution at the representative time-steps. In the case of smaller λ_{min} (Figure 8.6(a)), a temporal shift of size distribution peak towards the right-hand side, suggests the predominance of a characteristic curvature-driven coarsening regime during

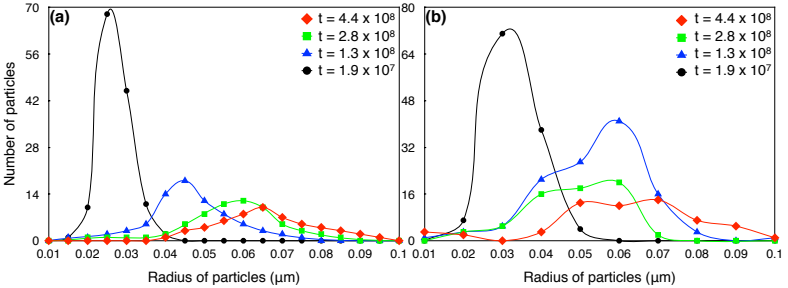

Figure 8.6.: Temporal evolution of the phases and the corresponding particle size distributions are plotted, by numerically simulating the isothermal eutectoid transformation ($\Delta T = 7.5$ K below the A_1 temperature), starting from an initial configuration comprising of grain boundary α layers (initial thickness, $\mathcal{L} = 5.04 \times 10^{-2}$ μm) and θ particles at minimum distances of (a) $\lambda_{min} = 0.075$ μm and (b) $\lambda_{min} = 0.084$ μm in polycrystalline γ (grain diameter = 1.2 μm).

the intermittent as well as final stages ($474.6 - 1559.4$ μs). At the later stages of the eutectoid transformation, coalescence of particles results in formation of non-spheroidal morphologies. Interestingly, for the case of larger λ_{min} (Figure 8.6(b)), a bimodal size distribution of evolving θ particles is obtained. To begin with (67.5 μs), the size distribution has a unique peak. However, as the α/γ transformation front temporally advances in mixed-mode, spheroidal as well as non-spheroidal particles evolve. On comparing the size distribution and the number of particles (inversely dependent on λ_{min}) in the simulated microstructure (Figure 8.6(a) and 8.6(b)), I conclude that the curvature-driven coarsening is not a dominant mode by which the eutectoid transformation proceeds, if the initial inter-particle spacing is larger.

At this point, I would like to state that the simulated bimodal size distribution of θ particles (for $\lambda_{min} = 0.084$ μm) is an inherent characteristic of a mixed-mode (cooperative/non-cooperative) eutectoid microstructures. As the transformation proceeds, the carbon redistribution is dependent on the preexisting arrangement as well as the distance of the nearest θ particles ahead of the advancing α/γ interface. Apparently, for a given random distribution of preexisting particles, the carbon redistribution mechanism is more complex when compared to the case of symmetric arrangement, for which theories are relatively well established [99, 190, 196]. The numerical results suggest an overlap of cooperative and non-cooperative transformation modes, which are primarily governed by interparticle spacing (from nearest neighbor) and spatial arrangement of θ ahead of advancing the α/γ front. As I demonstrate that the cooperative and non-cooperative evolution of the α/γ front as well as curvature-driven coarsening of θ particle are favored depending

upon the initial interparticle spacing and arrangement, the cementite morphologies and distribution found in the transformed microstructure yields insights concerning the intermittent regimes that predominate during the isothermal transformation.

8.2.2. Influence of prior γ grain size (r)

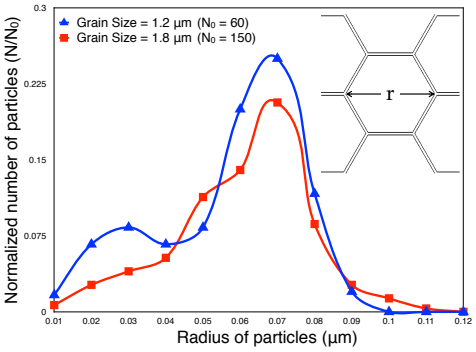

Figure 8.7.: Comparison of θ size distribution simulated at two different prior γ grain sizes ($r = 1.2$ and 1.8 μm). N_0 denotes the number of θ particles at the start of eutectoid transformation. λ for both the test cases is assumed to be same (equal to 0.147 μm). Prior α/γ boundaries are denoted by black lines in the schematic diagram.

To understand the influence of prior γ grain size on the final microstructure, I compare the size distributions of θ simulated at different 'r' (1.2 and 1.8 μm) while assuming the λ to be same (equal to 0.147 μm) for both the numerical test cases. A characteristic unimodal size distribution of θ is obtained at larger grain size (1.8 μm), as shown in Figure 8.7. On the contrary, a bimodal size distribution is favored, if the initial grain size is assumed to be smaller by 33%. It is imperative to note that the influence of introducing prior γ grain boundaries on the size distribution of θ is more pronounced at small grain size and diminishes, when increased[1].

8.2.3. Comparison with experimental microstructures

With a view to establish a synergy between the numerically simulated and experimental microstructures, I compare the various morphologies of θ observed in the experimental

[1]The preceding section written by K.A. is based upon a discussion with R.M. and B.N. which facilitated the correct interpretation of results.

microstructure with the phase-field simulations[2]. For the given set of growth conditions, one can observe various non-spheroidized θ morphologies, which lend insights into the evolution mechanism of α/γ front during various stages of eutectoid transformation. Two such exemplary θ morphologies namely elongated and bottle-shaped particles are shown in Figures 8.8(a) and 8.8(c) respectively. The occurrence of elongated particles near the center of the prior-γ grain in the transformed microstructure accentuate the present simulation results, which suggest that the α/γ transformation front evolves cooperatively, owing to an absence of preexisting θ ahead of it, during the final stages of eutectoid transformation. The temporal disappearance of θ ahead of the growth front is an outcome of curvature-driven coarsening which predominates, if λ is sufficiently small. On the contrary, bottle-shaped θ morphologies evolve, if the transformation proceeds in a mixed mode, depending on the distance from the nearest preexisting particle.

One can also identify an interesting spatial arrangement of θ particles in the transformed microstructure, which I prefer to call a "particle loop", as illustrated in Figure 8.8(b). Depending on the spatial arrangement and inter-particle spacing ($\lambda_{min} = 0.147\,\mu m$), the α/γ advancing transformation front drags the θ particles as it evolves towards the prior-γ grain center. For the present simulations, where it has been explicitly assumed that the preexisting α layers are aligned along the prior-γ grain boundaries, the simulated θ loop qualitatively agree with the experimental microstructure, illustrated along side.

At this point, it is worth clarifying that the illustrated experimental microstructures obtained by the inter-critical annealing of multi-component steel (Fe–0.92C–0.66Si–1.58Mn–1.58Cr–0.12Ni–0.05Mo–0.178Cu wt.%) serve as exemplary cases for a qualitative comparison with the numerically simulated θ morphologies and spatial arrangements [3]. For a quantitative comparison, the influence of various alloying element on the non-cooperative eutectoid transformation, needs to be considered in the future numerical studies. As the current work focuses on the analysis of a complex carbon redistribution mechanism that result in the formation of characteristic θ morphologies and arrangements in the transformed microstructure, the present numerical study is limited to the case of an isothermal transformation (ΔT = 7.5K) in binary Fe-C steel.

8.3. Discussion and outlook

Here, I have explained the influence of preexisting arrangement of θ particles on the evolution of α/γ transformation front. It is worth noting that the influence of arrangement of θ, which is shown to have profound effects on the final microstructure, has been all together neglected in the previous theoretical, experimental and numerical studies. Using phase-field simulations, I also explain the influence of preexisting α layer thickness and γ grain size on the evolution mechanisms in polycrystalline microstructures. It is shown

[2]B.N. motivated K.A. to compare the numerically simulated patterns with experimental microstructures. The comparative analysis was conducted by K.A.

[3]This statement written by K.A. is based upon a discussion with R.M. and B.N.

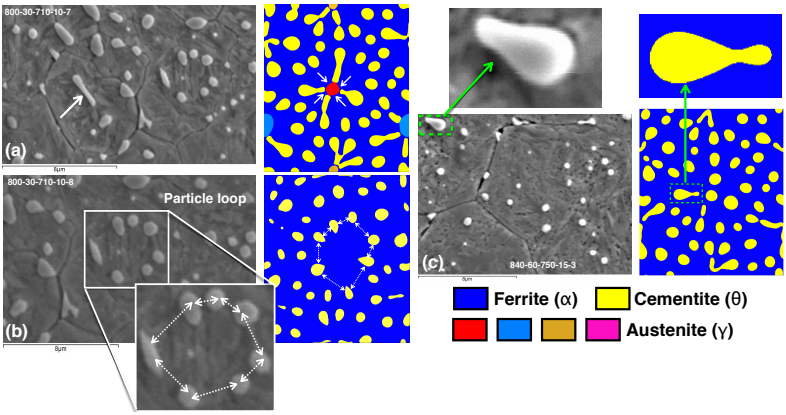

Figure 8.8.: Comparison of the θ morphologies observed in experimental microstructures with the exemplary simulation results. The illustrated experimental microstructures are obtained by isothermally holding the austenized sample (T_1 °C, t_1 minutes) at T_2 °C for t_2 minutes (Fe—0.92C—0.66Si—1.58Mn–1.58Cr–0.12Ni–0.05Mo–0.178Cu (wt.%) alloy). (a) Elongated θ particles aligned radially inwards and point towards the grain center. (b) As the α/γ transformation front evolves non-cooperatively, the divorced θ particles get aligned in a loop ($T_1 = 810$ °C, $t_1 = 30$ minutes, $T_2 =_1= 710$ °C, $t_2 = 10$ minutes). (c) The bottle θ morphology, which is representative of mixed co-operative/non-cooperative regime, active during the course of transformation. ($T_1 = 840$ °C, $t_1 = 60$ minutes, $T_2 =_1= 750$ °C, $t_2 = 15$ minutes). The experimental microstructures are provided by Z.X. Yin and H.K.D.H. Bhadeshia.

that the criterion for the lamellar-divorced-coarsening transition reported in earlier works holds even if the preexisting arrangement of θ particles is not symmetric. However, the coarsening rate is greatly influenced by the λ_{min} and relative arrangement, which in turn determine the final microstructure.

For the first time, I have reported the evolution of bimodal distribution of θ particles in Fe-C alloys, which are in good agreement with the previous experimental findings [197, 213, 214]. By analyzing the eutectoid transformation which proceeds isothermally from an initial setting comprising of a random distribution of θ particles and grain boundary α layers embedded in polycrystalline γ, I explain the mechanisms by which mixed θ morphologies evolve. Such microstructures are typically used in bearing steels [217]. It is also shown that the changing the preexisting arrangement of θ can trigger

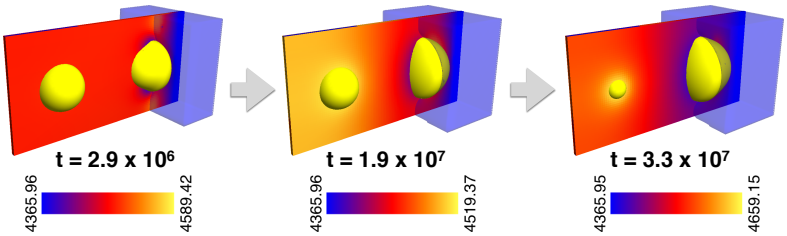

Figure 8.9.: 3-D numerical simulation showing the temporal evolution of eutectoid phases and the corresponding chemical potential map (central 2-D slice of the numerical domain) for a symmetric arrangement of preexisting θ particles ($\Delta T = 10$ K, $\lambda = 0.14$ μm). The predominance of curvature driven coarsening at small λ indicates the importance of accounting for the third dimension in numerical simulations.

a change from unimodal to bimodal distribution of particles. One can observe that the numerically simulated eutectoid microstructures possess many similarities with the experimental ones, as suggested by their comparison in Figure 8.8 and a following discussion on their evolution mechanisms. The present numerical results suggest that the curvature-driven coarsening is a dominant regime at lower λ_{min} values. If λ_{min} is chosen to larger, the transformation proceeds by complex interplay of cooperative and non-cooperative evolution modes.

Using phase-field simulations, I have shown that the morphology of preexisting ferrite layers influences the mechanism by which eutectoid transformation proceeds. However, the influence of preferential grain boundary or triple-junction nucleation on the θ size distribution have not been explored. In this context, a broader consensus on eutectoid nucleation can improve the microstructure predictive capability of the technique described in the present article. A significant limitation of this study is that the numerical simulations are limited to 2D. An exemplary simulation of the non-cooperative evolution in 3D is shown in Figure **??**. The addition of the third spatial dimension, essentially changes the dynamics of curvature-driven coarsening, which in turn, directly affects the final eutectoid microstructure[4]. Therefore, the numerical studies need to be extended by analyzing the morphological evolution of phases during the divorced eutectoid transformation in 3D.

[4]This statement, written by K.A. is based upon a discussion with R.M.

Part IV.

Phase-field modeling of polycrystalline evolution in veins

9. Free growth in an open cavity

The dependence of growth rate on facet orientations for a single crystal has been reported in the past [251, 252]. However, when polycrystal growth occurs, the neighboring crystals influence the growth rate. Microstructures formed due to crystal growth in an open cavity are characterized by an increase in grain size with more favorably oriented facets outgrowing the misoriented neighbors [253, 254]. The orientation selection rule responsible for the growth competition in such systems is based on misorientation with respect to the most preferred growth direction. In the following section, I simulate grain growth competition in 2D and 3D and deduce the orientation selection rule. Since the scope of the current study is limited to kinematics of crystal growth, the driving force is assumed to be constant. The results reported in this chapter were published in parts in [9] and [11].

9.1. Polycrystalline evolution of alum

One common mineral analogue that has been used to replicate free growth of crystals in laboratory experiments is Potash alum [$KAl(SO_4)_2 \cdot 12H_2O$] [237]. The crystal structure of alum is cubic with eight {111} facets. At room temperature it grows into an octahedral habit and also develops {110} and {100} facets. However, the growth rate of the {110} and {100} facets is much higher as compared to {111}, hence they are much smaller in size as compared to the primary facet [255]. Klapper et al. [256] report that temperature fluctuation increases the growth rate of {110} and {100} facets with respect to {111}. They also state that crystal dissolution and recrystallization can lead to formation of extra facets in the early growth stages.

In the first set of simulations, I study the effect of non-neighboring members (termed as "Long distance effect" by Nollet et al. [242]) on the free-growth regime of cubic crystals. A 2D simulation is carried out with 10 crystal seeds uniformly embedded at the bottom of the simulation domain and orientation designated as A, B or C degrees. In Figure 9.1, the second grain from left at the bottom grain boundary is assigned 'A' degrees and sixth grain as 'B' degrees. All other grains are assigned 'C' degrees. The orientation definitions in 2D simulations are given by Figure 9.1(h). Similarly, one can simulate the free-growth in 3D by embedding 36 crystal seeds uniformly at the bottom and assigning each orientation A and B once in the domain. The rest of the grains are assigned with orientation value C as shown in Figure 9.2. The numeric value of 'A', 'B' and 'C' are

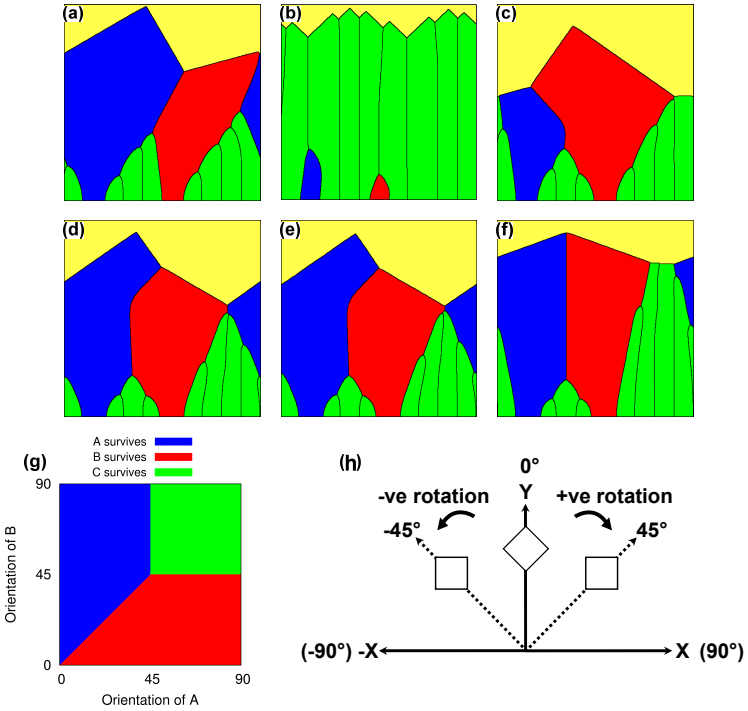

Figure 9.1.: Anisotropic growth competition of crystals with orientation A (blue), B (red) and C (green). (a) A = 15°, B = 30° and C = 45° (b) A = 15°, B = 30° and C = 0° (c) A = 30°, B = -5° and C = 45° (d) A = 10°, B = -15°and C = 45° (e) A = 11°, B = -15°and C = 45° (f) A = 25°, B = -25° and C =45° (g) Orientation map for C = 45°derived from phase-field simulation results (h) Orientation definition for 2D cubic crystal growth simulations.

chosen to investigate the effect of non-neighboring crystals (if any) on orientation selection during free-growth of crystals.

On the basis of phase-field simulation results as shown in Figures 9.1(a) - 9.1(f), an orientation map (Figure 9.1(g)) of crystal orientations 'A', 'B' and 'C' is derived which establishes the following selection rules:

- If every crystal has a different orientation, the crystal which is most favorably

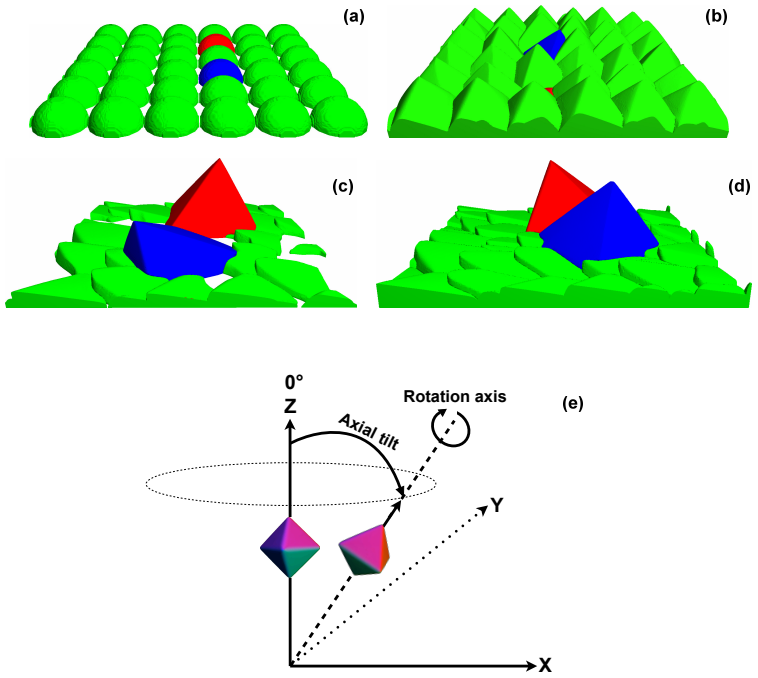

Figure 9.2.: 3D phase-field simulation of cubic crystal growth: (a) Initial condition with hemispherical nuclei uniformly embedded at the bottom of the domain and with assigned orientations of A (blue), B (red) and C (green) degrees. Growth competition leads to orientation selections according to the orientations (b) A = 15°, B = 30° and C = 0° (c) A = 5°, B = 30°and C = 45° (d) A = 15°, B = 10° and C = 45° (e) Schematic diagram to provide orientation definition for 3D cubic crystal growth simulations. The different colors of crystal facets is meant for better visualization of orientation components (axial tilt and rotation axis) and is not to be confused with color-coding in preceding sub-figures.

oriented (vertical in this case), survives and rest of the crystals are consumed.

- The consumption or survival of a crystal depends on its own orientation relative to its neighbors. The non-neighboring crystals do not affect the growth.

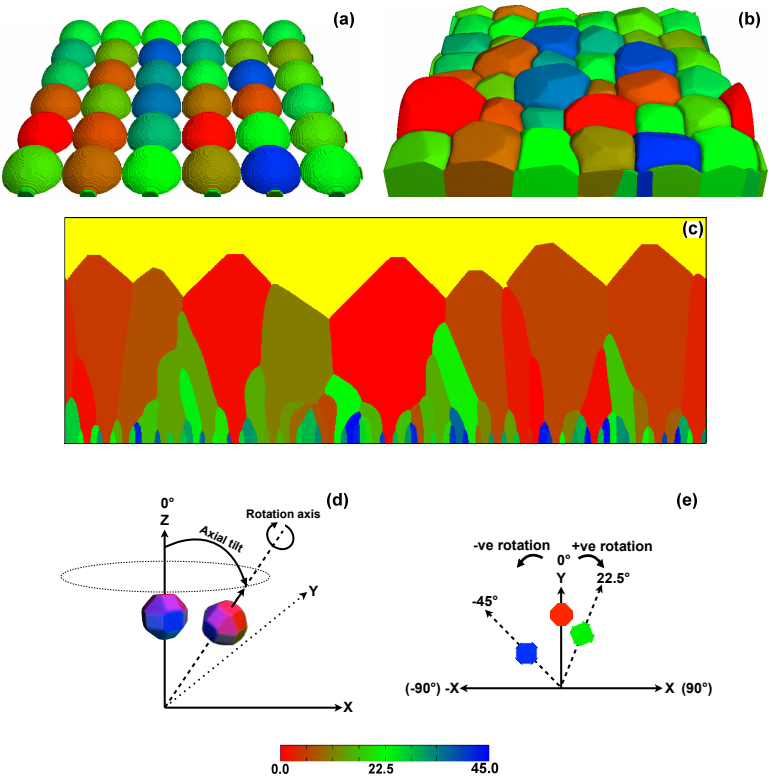

Figure 9.3.: Free growth of alum crystals with random orientations. (a) Bottom layer of the 3D phase-field simulation domain showing the spherical crystal nuclei and their assigned orientations in different colors. (b) intermediate stage of alum crystals growing in liquid. The facets {111}, {110} and {100} can be distinctly identified, (c) 2D simulation showing the final stage of growth competition. Favorably oriented crystals (reddish) outgrow their neighbors. (d) Orientation definitions for 3D and (e) 2D alum growth simulations. The colored crystal facets in Figure 9.3(d) is provided for a better visualization and is *not* related to colorbar shown below.

- Crystals retain the equilibrium shape (from Wulff construction) when in contact

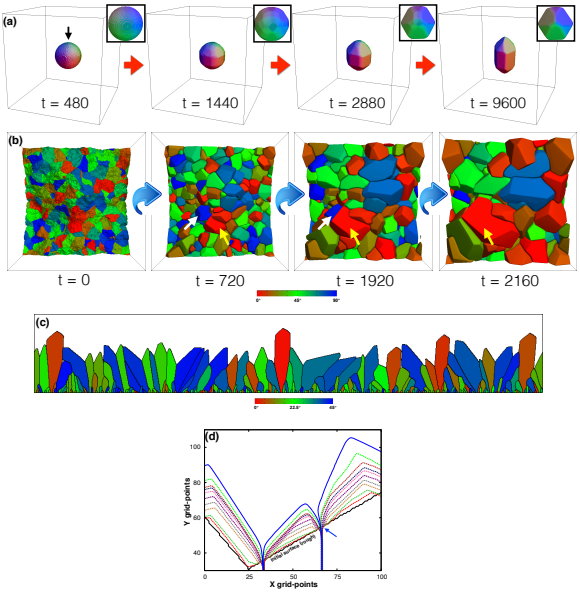

Figure 9.4.: Three dimensional phase-field simulation of (a) a quartz crystal evolving from a spherical nucleus. The volume of the evolving crystal is preserved so that the final morphology (when temporal shape evolution stops) corresponds to the equilibrium crystal shape. (b) the crystal growth competition using the faceted-type anisotropic surface energy, if the initial crack aperture is wide. The white arrow shows a misoriented crystal (see color-map) which is overgrown by the favorably oriented neighbors while the yellow arrow shows a favorably oriented crystal overgrowing the neighbors. (c) A 2D simulation showing the late stage "pillar-like" growth of quartz. The favorably oriented crystals (reddish color) outgrow the blue and green misoriented neighbors. The illustrated colormaps show the misorientation w.r.t to sealing direction (vertical). (d) Colored isolines of the temporally evolving polycrystals in early stages. It is observed that under the present set of assumptions for the numerical simulations, the triple junction stay immobile until well defined facets have formed, as shown by the blue arrow and the corresponding iso-lines.

with liquid at all times.

- Crystals having the same growth orientation with respect to most preferred orientation (vertical in this case) form perpendicular grain boundaries (relative to initial surface) and co-exist in the final microstructure, if the other neighboring crystals are not more favorably oriented. This is also observed in the 3D case when two crystals have a similar orientation with respect to the vertical line but lie in different planes.

Next, I perform a 3D simulation of alum crystal growth such that crystals also develop {110} and {100} facets in addition to {111} as shown in Figure 9.3. Hemispherical crystal seeds are uniformly embedded at the bottom of the domain as shown in Figure 9.3(a), and every crystal is assigned a random orientation with respect to the normal direction of the growth plane. The growth competition results in the consumption of poorly oriented crystals (greenish and bluish in color) and in survival of favorably oriented ones (reddish) as shown in Figure 9.3(c).

9.2. Polycrystalline evolution of quartz

I use the faceted anisotropy of the surface energy function (equation 4.3) to simulate the evolution of single quartz starting from a spherical nucleus, as shown Figure 9.4(a).

As a model test case, I relax the earlier assumption of volume preserved evolution to reproduce the growth competition in polycrystalline quartz (Figure 9.4)[1], typically observed in experimental studies. It is apparent from the temporal evolution of the freely growing polycrystal that the misoriented crystals (blue) are consumed by more favorably oriented ones (red). The quartz polycrystal develops prominent facets and strong growth competition result in the overgrowth of crystals by favorably oriented ones[2].

[1] Data visualization package used by K.A. to generate 3D iso-surfaces was developed by M.S. and B.N.
[2] The iso-lines (shown in Figure 9.4(h)) were plotted by K.A. on the advise of J.U. and B.N.

10. Grain boundary tracking behavior in unitaxial crack-seal microstructures

In the present chapter, I modify the boundary condition and parameters to present a systematic study of unitaxial crack-sealing, e.g. crack surface roughness, crack opening velocity, opening trajectory and number of crystal nuclei[1]. A detailed discussion of 2D simulation results and possible extensions of the current numerical model to 3D is also presented. This chapter was published in [9].

10.1. Crack-seal growth

In the following section, I use the phase-field method described in the previous chapter, to study the effect of various crack parameters namely roughness, opening velocity and trajectory on the crack-seal microstructure. Further, I also examine if the number of competing crystal nuclei causes a variation in the final microstructure.

Numerical simulations are carried out with periodic asperities on the crack wall and uniformly distributed crystal nuclei placed at the top of the domain. The crystals grow downwards in the direction of crack opening. All the crystals are assumed to posses a cubic anisotropy and are assigned random orientation in the range of $-45°$ to $45°$ with respect to the vertical direction.

10.1.1. Effect of crack wall roughness

The crack surface is assumed to be periodic and the degree of roughness is controlled by the vertical angle β which is varied between $90°$ and $180°$ while keeping the wavelength constant as shown in 10.1(a). An angle of $\beta = 180°$ corresponds to a smooth surface. The crack is opened periodically at an angle θ_{open} with respect to the vertical direction. In order to study the influence of crack roughness, I fix the value of θ_{open} to be $45°$. The velocity of crack opening is selected in such a way that a complete sealing of the crack occurs before every crack opening event.

[1] The original ideas to utilize the multiphase-field model to investigate vein growth characteristics was conceived by B.N. during her doctoral research. The following work presented by K.A. is an expansion of B.N's preliminary ideas.

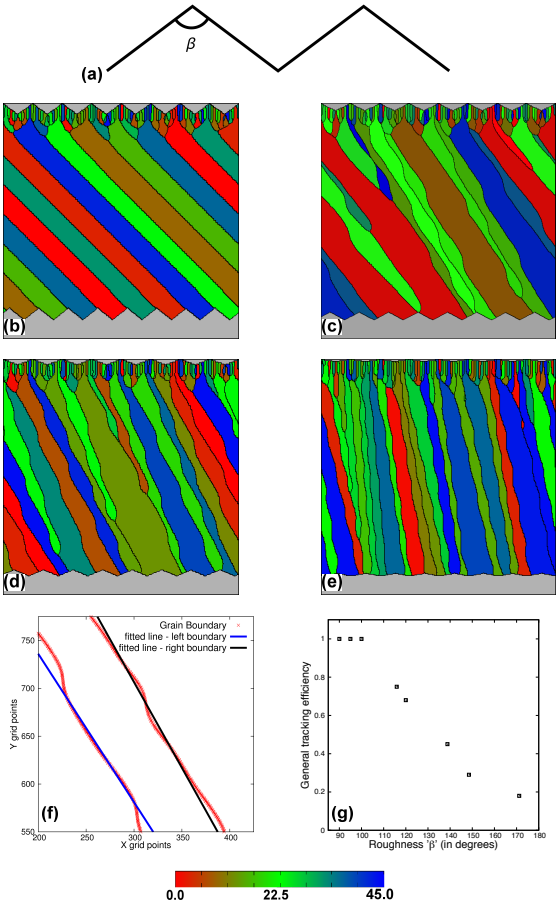

Figure 10.1.: Effect of crack-wall roughness on the grain boundary tracking behavior. The direction of the crack opening is $\theta_{open} = 45°$to the vertical line. (a) The roughness of the crack is governed by angle β. The simulated grain structures refer to wall roughness of (b) 100°, (c) 120°, (d) 139° and (e) 171°. (f) Straight lines are fitted along the grain boundaries to calculate (g) tracking efficiency, plotted as a function of crack roughness. The nature of the plot obtained from 2D phase-field simulations is consistent with the results of Urai et al. [218]. The colors refer to different crystal orientation with respect to the vertical direction (see colormap).

At a higher crack roughness ($\beta = 90°$) , it is observed in Figure 10.1(b) that the crystals track the crack opening trajectory. This is also characterized by the crack peaks (referred as 'Grain Boundary Attractor' by Hilgers et al. [241] and Nollet et al. [242]) attracting the grain boundaries and forcing the crystals to grow in a fibrous morphology. As β is successively increased in Figures 10.1(c) - 10.1(e), the tracking behavior decreases and crystals develop curved/oscillating grain boundaries. The period of oscillation reduces with decreasing roughness.

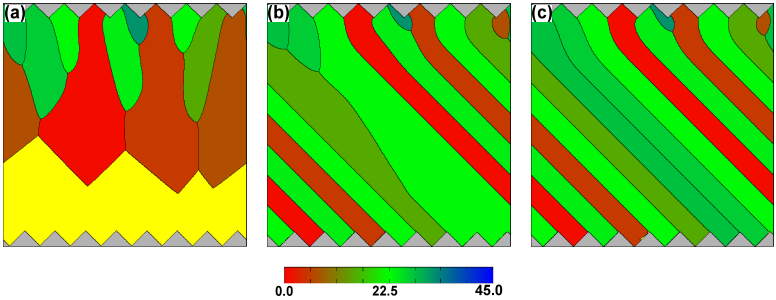

Figure 10.2.: Effect of crack-wall opening velocity on crystal growth morphology and final microstructure. The growth is elongate-blocky at higher crack opening rate in contrast to fibrous when the crack opening rate is slower. Further, within the complete crack seal regime, a morphological transition from curved to straight boundaries is observed. The direction of the crack opening is 45°with respect to vertical. The crack opens after every (a) $200\Delta t$, (b) $500\Delta t$ and (c) $700\Delta t$ seconds where $\Delta t = 0.12$ second refers to time-step width. The colors refer to different crystal orientation with respect to vertical (see colormap).

To quantify the grain boundary tracking behavior, one can plot the contour of the crystal grain boundaries (corresponding to one of the tracking grain boundary) and fit straight lines to the left and right crystal boundaries as illustrated in Figure 10.1(f). The overall tracking inclination θ_{track} is defined as the mean value of the slopes of the two lines and is used to elaborate the general tracking efficiency as:

$$\mathrm{GTE} = \frac{\theta_{track}}{\theta_{open}} \tag{10.1}$$

GTE is plotted as a function of roughness angle β in Figure 10.1(g). The resulting trend indicates that the general tracking efficiency decreases for lower crack-surface roughness, beyond a certain β value. It is to be noted that purpose of the prefix 'general' in the

term 'general tracking efficiency' (GTE)[2] is to highlight the difference with the definition of 'tracking efficiency' by Urai et al. [218]. As evident from the simulations and plotted results in Figure 10.1, GTE converges to the definition of 'tracking efficiency' when crystal growth is isotropic without any oscillations. Additionally, the definition of GTE is more general as it remains valid even when characterizing the tracking behavior of oscillating grain boundaries.

10.1.2. Effect of crack opening rate

To study the effect of crack opening velocity on vein growth, a simulation setup similar to section 10.1.1 is considered with 10 crystal nuclei. The roughness angle $\beta = 100°$ is selected to ensure a high level of tracking efficiency, if complete sealing occurs before every opening event. The crack opening angle is kept constant ($\theta_{open} = 45°$) and rate of opening is varied as shown in Figure 10.2. It is observed in Figure 10.2(a) that at higher crack opening rate (as compared to crystal growth rate), crystals lose contact with the crack surface. This leads to the formation of an elongate-blocky growth morphology, since crystals now grow more or less anisotropically and follow the orientation rule as observed for free-growth in Figure 9.1(g). At lower crack opening rate as in Figures 10.2(b) and 10.2(c), crystals grow isotropically in fibrous morphology, since the facet formation is suppressed. Further, within the complete crack-seal regime, at a higher opening velocity, the crystal boundaries have a tendency to curve in contrast to the case when opening velocity is smaller. The simulation results for the influence of crack opening velocity on crystal growth morphology are presented in Figure 10.2. A definitive change in the crystal growth morphology is observed if crack opening rate is varied.

10.1.3. Effect of crack opening trajectory

In the next series of simulations, 100 crystal nuclei with different orientation are uniformly embedded at the top of the domain and the crack opening angle θ_{open} is varied. The crack roughness angle β is selected to be 100° and a complete sealing is ensured at every opening event. The phase-field simulation results show that crystals track the crack opening trajectory, irrespective of θ_{open}. Thus, the grain boundary tracking efficiency is not affected by the crack opening angle. The results of the simulation are summarized in Figure 10.3. On further increasing the magnitude of the crack opening increment in Figure 10.4 while ensuring complete sealing before every opening event, one observes that the tracking behavior is lost and crystals grow in a random morphology (Figure 10.4(a)). However, when the crack opening increment is reduced ten-folds, while keeping θ_{open} unchanged, crystals re-establish a tracking of the crack opening trajectory as shown in Figure 10.4(b).

[2]This term was coined by K.A. based on a discussion with M.S.

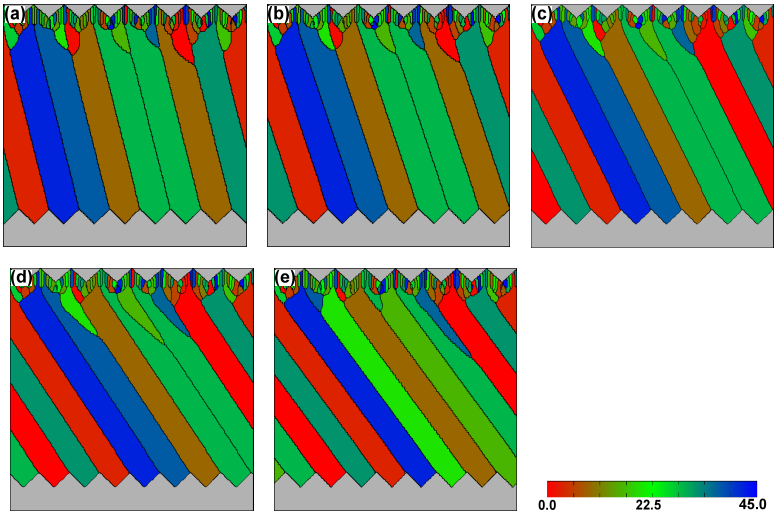

Figure 10.3.: Effect of crack opening trajectory on crack-seal microstructure. The angles of opening θ_{open} are (a) 14.0°,(b) 18.4°,(c) 26.5°,(d) 33.6°and(e) 36.8°with respect to vertical in anti-clockwise direction. The crystals track the crack opening irrespective of the trajectory, if opening increments are small and crack surface is sufficiently rough. The colors refer to different crystal orientation with respect to the vertical direction (see colormap).

10.1.4. Effect of number of crystal nuclei

The number of nuclei is varied to study its influence on the vein growth morphology. The crack is assumed to be sufficiently rough for 100% tracking of crystal boundaries and complete sealing is ensured. The phase-field simulations show that varying the initial number of nuclei does not influence the tracking behavior. It is noteworthy that the number of surviving crystals remains constant and is numerically equal to the number of peaks in the crack surface which faces the crystal growth front. The crystal boundaries stabilize at the crack peaks which suggest that these attract the grain boundaries. Further, one does not observe any change in growth morphology once the number of crystals surviving equals the crack peaks, irrespective of the initial number of nuclei as shown in Figure 10.5.

Finally, 3D phase-field simulations of crack-sealing are carried out by embedding 100 alum crystal nuclei on computationally generated rough crack surface in Figures 10.6(a)

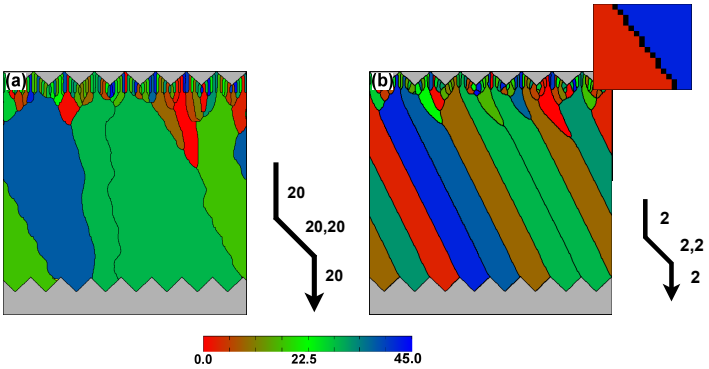

Figure 10.4.: Effect of crack opening increment on the crack-seal microstructure. The same number of crystal nuclei, crystal anisotropy and wall morphology are used as in Figure 10.3. (a) Loss of tracking behavior for linear and oblique opening in large increments (20 grid-points lateral offset). (b) Grain boundary tracking for linear and oblique opening in smaller increments (2 grid-points lateral offset). Crystals track the trajectory only when opening increments are sufficiently small. The picture on upper right hand side (plot of $\phi = 0.5$) shows the grain boundary morphology provided to compare with crack-opening path. The colors refer to different crystal orientation with respect to the vertical direction (see colormap).

and 10.6(b). The roughness of the 3D crack surface is controlled by varying the range of amplitude of peaks. Higher roughness relates to a wider range of maximum and minimum height of peak which is permissible (chosen randomly at different spatial locations). The crack is opened slowly to ensure ensuring complete sealing before every opening event. The 3D simulation results are displayed in Figure 10.6 which shows a layer-by-layer plot of the simulation domain. The simulation results reveal that a crack surface with higher roughness forces the crystals to track the opening trajectory. As the surface roughness is reduced, the resulting grain boundaries partially form curved/oscillatory morphologies (Figure 10.6(d)). It can be observed that crystals grow in a mixed regime when the wall roughness is not sufficiently high.

10.2. Discussion and outlook

In the present chapter, the multiphase-field model for grain-growth has been extended to study the crystal growth in veins in crack-sealing conditions. The presence of a barrier

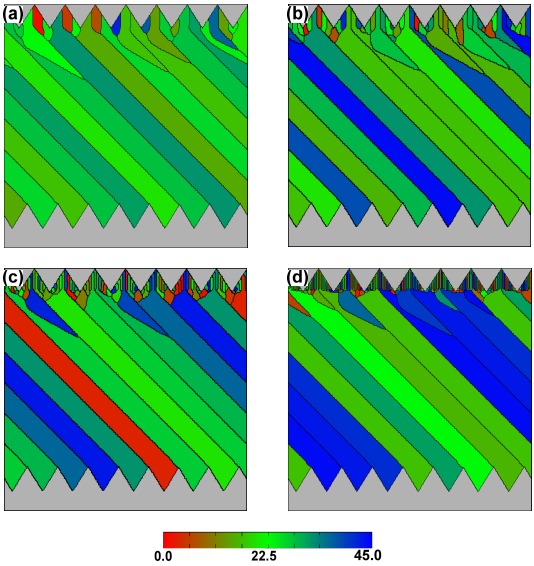

Figure 10.5.: Effect of initial number of nuclei on crystal growth morphology and final microstructure. The crack opening increments are small in the direction 45°with respect to vertical. The crack surface facing the crystal growth front has 8 peaks. The number of crystal nuclei are varied as in (a) 25, (b) 50, (c) 100 and (d) 250 to observe the effect on final microstructure. The number of crystals that end up tracking the crack openings is equal to the number of peaks on the advancing crack. Colors refer to different crystal orientation with respect to vertical (see colormap).

for example, a rigid and rough crack surface, obstructs the freely growing crystals, forcing them to grow into a morphology unrelated to the equilibrium crystal shape. It is found that the boundary conditions such as roughness, opening velocity and trajectory determine the final crack-seal microstructure. The phase-field simulation results of crack-sealing process suggest that if the wall rock is sufficiently rough and opening velocity is small, the crystals grow isotropically, in a fibrous morphology and track the crack-opening trajectory. In this case, anisotropy in surface energy does not effect the growth morphology since facet formation is suppressed due to the additional boundary condition, which corroborates the previous simulation and experimental studies on crack-sealing process [218, 241, 242]. Moreover, higher roughness of the facing wall rock also increases the fineness of fibrous microstructure. This is inferred from Figure 10.5 which shows that if the roughness is

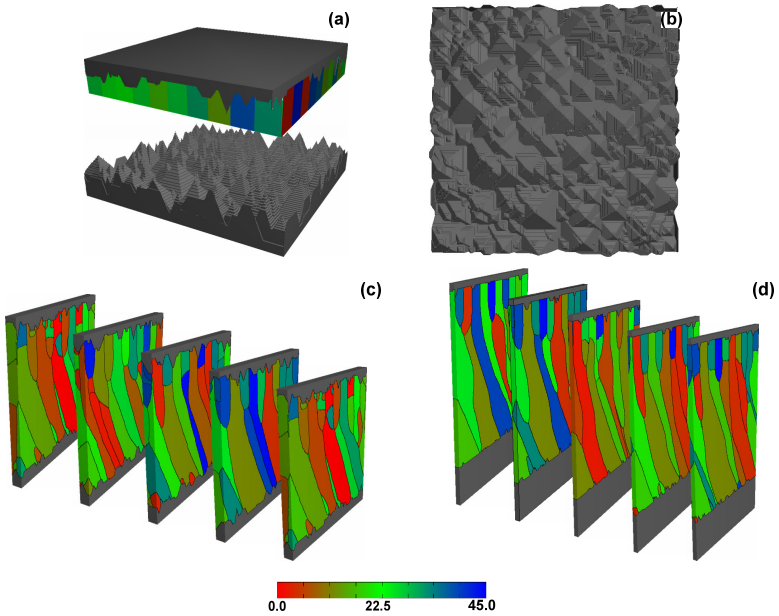

Figure 10.6.: Crystals are embedded on an algorithmically irregular surface for simulating crack-sealing process in 3D. The crack surface roughness is defined by the amplitude of peaks. To reduce the surface roughness, the amplitude of every peak is reduced by a numeric factor. (a) The initial simulation domain setting. (b) Top view of the crack surface. 3D layer plot of the phase-field simulation of crack-sealing process showing (c) grain boundary tracking along with occasional occurrence of curved boundaries for the roughness factor 6 and for a crack opening velocity of 2 grid points lateral offset, in (d), the number of curved/inflected grain boundaries increases for the roughness factor 10 and for a crack opening velocity of 4 grid points lateral offset. The crack opening trajectory is similar to the one shown in Figure 10.4(b). Colors refer to different crystal orientation with respect to vertical direction (see colormap).

sufficiently high, the number of fibers formed is numerically consistent with the peaks on the facing crack surface. At a lower crack surface roughness, the grain boundary tracking efficiency decreases and the crystal boundaries have a curved/oscillating morphology as presented in Figures 10.1(c), 10.1(d) and 10.1(e). The anisotropy of the surface energy

provides an explanation for the curvature observed in grain boundaries in this case, as the crack opening events occur along an oblique 45° line with respect to the vertical direction. It is noteworthy, that grain boundaries alone do not provide much information about the crack-opening trajectory in such cases. The simulation results also reveal that straight grain boundaries are formed when surface energy of the growing crystals is assumed to be isotropic. Further, within the complete crack-seal regime, when the opening increment is relatively faster, curved grain boundaries are formed. 3D simulations of the unitaxial crack-sealing process accentuate these findings; if the wall rock roughness is low and crack opening velocity is increased while still ensuring complete sealing before every opening event, the crystals growth occurs in a mixed regime, characterized by a decrease in tracking behavior with a propensity to form curved grain boundaries. A systematic study to correlate of crack roughness (by choosing more realistic boundary condition for e.g. fractal surface) and opening rate (in 3 dimensions for more relevant vein forming crystals like quartz or calcite) with the extent/amplitude of grain boundary curvature/oscillation is presented in Chapter 11.

At this point, I would like to clarify that the objective of present work is not to question the numerical algorithm or the simulation results of Urai et al. [218], Bons [240], Hilgers et al. [241] and Nollet et al. [242]. Rather, it is aimed to advance the numerical studies to 3D by adopting a thermodynamically consistent approach and to discuss the applicability of phase-field method to study polycrystal growth in veins. In this scope, the foremost intention is to discuss the reproducibility of previous results (in free-growth as well as crack-sealing 2D simulations) as well as advantages of using the present phase-field model (3D numerical studies for crystal of any shape, large-scale simulations and provision to implement transport)[3].

The present work establishes the phase-field method as comprehensive, artifact-free and standout approach to simulate the polycrystalline evolution in unitaxial veins. The simulation results also demonstrate the general capability of multiphase-field method in dealing with anisotropic 3D vein-growth problem. It is noteworthy that the numerical model presented in the current work provides a general framework to simulate crystals of any shape. Since the underlying model equations are based on continuum mechanical and thermodynamic concepts, several extensions of the present vein-growth model are possible. This includes the studies related to diffusion driven grain evolution and hydrodynamic convection. Including such effects in the present phase-field model is imperative for the complete understanding of the vein growth problem. Once implemented, the model can be further utilized to study the precise effect of hydrodynamic convection on the morphology of the vein front and crystal boundaries. Further, this also helps in debating the question posed by Barker et al. [260] whether vein formation involves advective fluid flow, or occurs by local diffusion of material from the surrounding wall rock. Though, this requires significant computational resources, the efficient parallelization of the phase-field solver [244] (utilized for phase-field simulations presented in this article) makes it feasible.

[3]The preceding paragraph written by K.A. is based upon a discussion with B.N., M.S. and M.R.

11. Fracture cementation processes in 3D

In the present chapter, I study the influence of the realistic boundary condition i.e. crack opening rate on the 3D tracking efficiency in cemented (or sealed) fractures, as against the 2D studies reported in chapter 10 for cubic crystals. By employing advanced visualization and innovative post-processing techniques, new methodologies to calculate the general tracking efficiency for a more complex motion of grain boundaries is proposed. This chapter was published in [10].

11.1. Numerical aspects

With an objective to numerically simulate crack-sealing in veins (or cement, as defined in petrology) and to characterize the resulting microstructure, I choose quartz crystals as a representative cement forming material. Fractal based models are considered to be an efficient method for creating realistic-appearing terrain [261]. An algorithmically generated (diamond-square algorithm) fractal surface is utilized to model a 3D crack surface (boundary condition) for phase-field simulations (Figure 11.1). The progressive

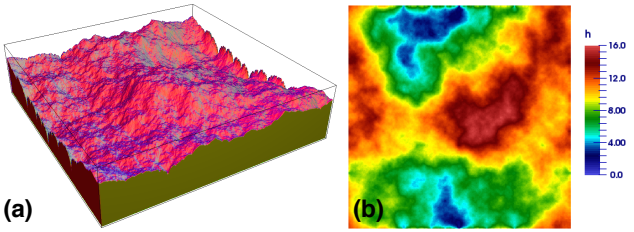

Figure 11.1.: (a) Fractal surface (generated by a well-known diamond-square algorithm) used for 3D crack-sealing simulations. (b) Height-map of the generated surface.

fracturing of host-rock and crystal precipitation in the open space is algorithmically replicated once by numerical pre-processing to obtain the initial condition for a simulation as shown in Figure 11.2. The pre-processing algorithm adopted is as follows:

- The fractal topology of the lower crack surface is generated by a C program to implement the well-known diamond-square algorithm [250]. The topography (height-map) of the upper crack surface is obtained by subtracting the respective heights (for lower crack-surface) from the total height of the parent rock in consideration. The two complementary fractal surfaces are stationed over each other with a minor clearance which represents the fracture in host rock.

- The space between the upper and lower surface is increased (by 5 grid points in the fracture direction) which represents the first crack-opening event.

- Crystals of equal size with different crystallographic orientation in space are initially laid on the lower crack surface. At this point, it is important to note that the size of the crystal nuclei needs to be equal in order to negate the advent of size-effects in the following fracture cementation simulations. The numerical pre-processing technique in order to rule out any such possibilities involves the following sub-steps: Cuboid crystal nuclei (different colors represent an axial tilt of the crystallographic axes defined in the previous section) are generated separately and merged with the parent numerical domain containing the cleft (a boundary condition) such that the former can be over-written. The resulting domain can be described as a perfectly sealed microstructure.

- The lower crack surface is shifted downwards again to create a small space between the wall and crystal front. Thus, one obtains the initial numerical domain to start the phase-field simulations.

At this point, I would like to clarify that the effectiveness of commonly used fractal techniques that are used to model natural terrain, is a topic of ongoing debate. For the present studies, I choose the diamond-square algorithm due to simplicity and ease with which it can be computationally implemented. The primary intention of using such a numerically-constructed rough surface is to demonstrate the ability of the developed pre-processing algorithm to design a relevant boundary condition (in 3D), for the simulation of fracture cementation process. In past years, efficient algorithms have been developed to generate realistic surface [262, 263]. However, a detailed comparison of such algorithms merit a separate discussion which in all certainties, is neither the focus nor the highlight of the present thesis.

The unitaxial, one-directional growth is numerically simulated to investigate the formation of 3D crack-sealing microstructure using the initial condition generated in Figure 11.2, and the tracking behavior of grain boundaries and multi-junctions are characterized. The following discussion will focus on the two 3D simulation test cases with the same initial condition but different crack-opening rate, as described in Table 11.1.

As a result of wall rock opening along the predetermined opening trajectory, the crack-aperture increases during simulation run-time. This adversely affects the computational efficiency as the size of simulation domain increases in the fracture direction. In order to avoid such complications, the simulation is carried out in a moving frame (also known as

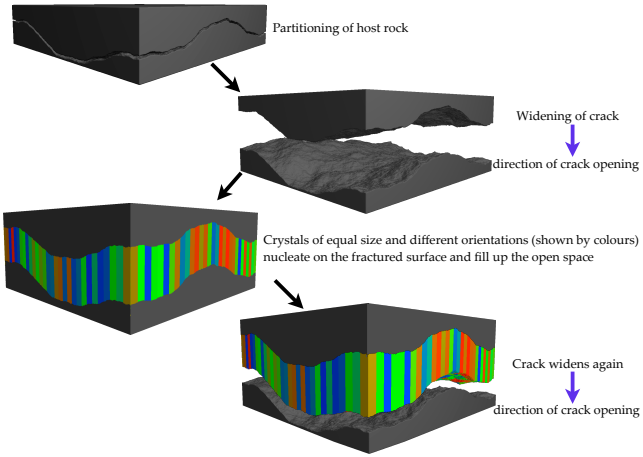

Figure 11.2.: Sequence of numerical pre-processing adopted to obtain a homogeneous overlay (of same size) of crystal nuclei on the algorithmically generated fractal surface. The final domain appearing in the above sequence is used as the initial condition for phase-field simulations.

Table 11.1.: Table showing the choice of normal crack-opening rates for simulations A and B ($\Delta x = \Delta y = \Delta z = 1.0$ and $\Delta t = 0.12$). N_A and N_B represent the crack-opening displacements in the normal direction for the test cases 'A' and 'B', respectively (as shown in Figure 11.5).

Simulation	Time between successive opening	Opening increment in vertical direction (N)	Trajectory
A	$2\Delta t$	$3\Delta x$ (N_A)	Quarter arc
B	$2\Delta t$	$8\Delta x$ (N_B)	Quarter arc

shifting-box simulation). In the present simulations, the domain is shifted in the growth direction (downwards) by adding a row of grid-point at the top of domain and discarding off a row of grid-points at the bottom, every time the advancing crystal growth front fills up 10% of the simulation box. The final domain is obtained by aggregating back the discarded rows of pixels as described by Ankit et al. [5] for a different material system. Further, one has to ensure that the advancing crystal-rock interface always stay within the boundaries of shifting-box for every simulation time-step. A typical example of the 3D phase-field simulation of crack-sealing shown in Figure 11.3 exemplifies the advantage

of numerically simulating and analyzing the fracture cementation in 3D instead of 2D.

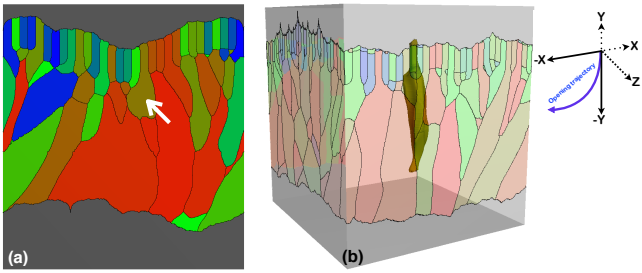

Figure 11.3.: 3D phase-field simulation of the crack-seal microstructure. The direction of crack opening is along the quarter circle in the plane of computational thin-section (as shown by the blue arrow in the opening-trajectory schematic diagram). The present simulation shows the morphology of grain boundaries after 400 crack opening and sealing events. (a) A 2D section of the 3D computational microstructure suggests consumption of the grain marked by white arrow. (b) A look at the 3D computational microstructure reveals that the grain was actually not consumed; rather it evolved along a different plane. Transparency of the surrounding grains enable the visualization of the tracking cement inside the numerical domain.

11.2. Modeling of crack as a barrier

For the present studies, the crack surface is modeled as an inert phase, which does not undergo a volumetric change to minimize the interfacial energy. In a strict numerical sense, it simply means that the phase evolution equation (4.6) is not solved at grid-points which constitute the crack. In general, I prefer to call all such aggregate of grid-points as *barrier*. To picturise the situation, let us consider a numerical domain that comprises of three phase-field parameters (ϕ_{grain1}, ϕ_{grain2} and ϕ_{liquid}) and a barrier, as shown in Figure 11.4. The corresponding domain volumes are given by Ω_{grain1}, Ω_{grain2}, Ω_{liquid} and Ω_{barrier}, respectively. The modified free energy functional (Equation 4.1), which do *not* account for any volumetric change in the barrier is given by,

$$\mathcal{F}(\boldsymbol{\phi}) = \int_{\Omega-\Omega_{\text{barrier}}} \left(f(\boldsymbol{\phi}) + \varepsilon a(\boldsymbol{\phi}, \nabla\boldsymbol{\phi}) + \frac{1}{\varepsilon} w(\boldsymbol{\phi}) \right) dx, \tag{11.1}$$

where, $\Omega = \Omega_{\text{grain1}} + \Omega_{\text{grain2}} + \Omega_{\text{liquid}} + \Omega_{\text{barrier}}$. To numerically simulate the fracture cementation process that proceeds by the crack-sealing mechanism, the barrier is constrained

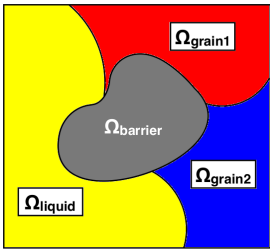

Figure 11.4.: Schematic representation of the barrier and the surrounding phase-fields. The barrier is constrained to evolve spatially, as per the desired crack-opening displacement without undergoing a change in shape or volume.

to evolve spatially (no surface energy minimization) as per the assigned crack-opening displacements shown in Figure 11.5[1].

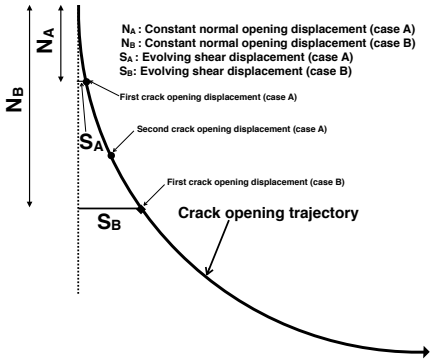

Figure 11.5.: Schematic diagram (not to scale) to illustrate the crack-opening trajectories that are prescribed for the numerical test cases 'A' and 'B'. The values of crack-opening displacements in the normal direction, N_A and N_B that are assumed to be constant are listed in Table 11.1. The shear displacements, S_A and S_B are estimated before every crack-opening event to ascertain the net displacement along a quarter circle.

[1]The preceding paragraph written by K.A. is based upon a discussion with M.S. and B.N.

11.3. Quantifying fracture cement tracking characteristics

The term 'tracking efficiency' [218] quantifies the tracking behavior of crack seal microstructures and is governed by the roughness of the fracture wall, crack opening width and the ratio of crystal growth versus crack opening rate [241, 242]. Ankit et al. [9] amend this definition to a 'general tracking efficiency' (GTE) based on a fitting procedure for linear crack opening trajectory. It is to be noted that both the above definitions of grain boundary tracking efficiency are based on the final microstructure morphology and do not account for the temporal evolution of grain boundary tracking behavior. The dynamics of tracking efficiency is particularly important when the wall roughness of the advancing crack surface is not sufficiently high and the opening trajectory is non-linear. For such cases, general tracking efficiency is numerically obtained by fitting a straight lines in infinitesimally small time interval δt in which both the crack opening as well as grain boundary morphology can be assumed to be linear. In the following section, I highlight the advantage of calculating tracking efficiency by accounting for time evolution of grain barycenter (center of mass). One can calculate the tracking efficiency of the 3D computational microstructure by two different methods:

1. The isosurfaces of the surviving crystals that are in contact with the advancing wall rock is visualized and the local peaks of the facing crack surface are plotted. I employ a post-processing algorithm which iteratively inspects after every numerical time-step, if a given grid-point is a local peak among the 'k' nearest neighbors that lie along the barrier/grains sharp-interface. For the present test cases 'A' and 'B', I assume that 'k' equals 10. The peaks of the fractal surface lying along the grain boundaries/multi-junctions are extracted from the computational microstructure of the simulations A and B (defined in Table 11.1) and are then superimposed, as shown in Figures 11.6(a) and 11.6(c), respectively[2]. The total number of the grain boundary/multi-junction tracking peaks is designated as N_{tp}. Similarly, those fractal peaks which neither lie along grain boundaries nor at multi-junctions are plotted (Figures 11.6(b) and 11.6(d)). The total number of such non-tracking peaks is denoted by N_{ntp}. The general tracking efficiency (GTE) for the 3D crack-seal microstructure is defined for the i^{th} simulation time-step as:

$$\mathrm{GTE}_1^i = \frac{N_{tp}^i}{N_{ntp}^i}. \tag{11.2}$$

   The definition of GTE_1^i is extended to account for the overall temporal evolution of

[2] This technique also known as 'masking' was implemented in the visualization package by M.S. This technique was chosen for the present scientific problem after a discussion with C.H. and B.N. The illustrated plots are prepared by K.A.

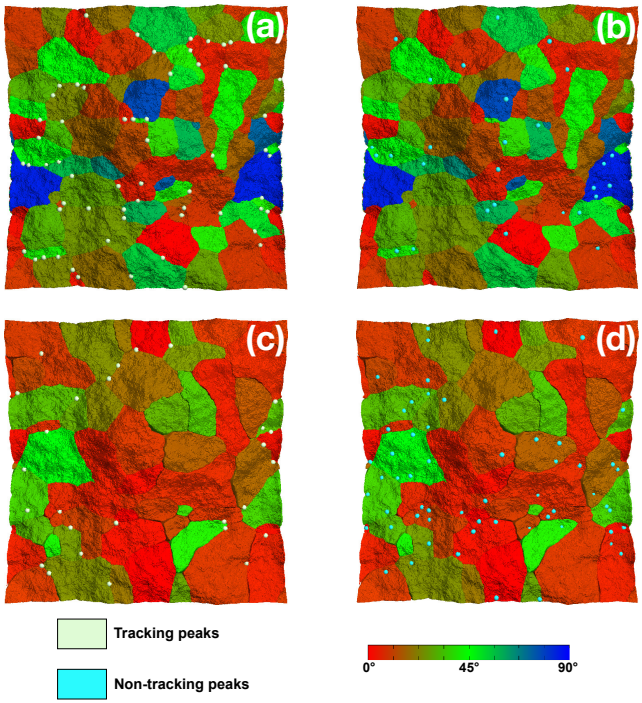

Figure 11.6.: Local peaks of crack surface (represented as colored spheres) plotted over the rock-crystal growth interface for simulation A in (a) and (b) and for simulation B as shown in (c) and (d). The fractal peaks that are tracked by the grain boundaries/triple/quadruple junctions are plotted as off-white spheres in (a) and (c). The fractal peaks not tracked by grain boundaries/multi-junctions are plotted as light-blue spheres in (b) and (d). On the basis of the final microstructures, the values of GTE_1^t ('t' being total time) for simulation A and B are 0.685 and 0.325 respectively. On accounting for temporal evolution, the corresponding values depreciate to 0.491 and 0.206. The grain colors refer to the axial tilt indexed in the color-bar.

tracking efficiency as:

$$\mathrm{GTE}_1 == \frac{\sum_{i=1}^{n(\delta t)} \frac{N_{tp}^i}{N_{ntp}^i} \cdot (\delta t)}{n\,(\delta t)} = \frac{\sum_{i=1}^{n(\delta t)} \frac{N_{tp}^i}{N_{ntp}^i}}{n} \tag{11.3}$$

where δt, n and t represent time-step width, number of time-steps and total simulation time respectively.

2. The second definition of grain boundary tracking efficiency takes into account the temporal evolution of the barycenters of the surviving crystals in the shifting box, as described in the previous section. The actual positions of the surviving crystal barycenters are obtained by adding the coordinates of the barycenters in the shifting box with the total shift of the simulation box as shown for three tracking grains (Figure 11.7).

   For calculating the general tracking efficiency, the expression proposed by Ankit et al. [9] is redefined for a small time interval δt and averaged over the total simulation time, according to

$$\mathrm{GTE}_2 = \frac{\sum_{i=1}^{n(\delta t)} \mathrm{GTE}_2^i \cdot (\delta t)}{n\,(\delta t)} \tag{11.4}$$

   where, $\mathrm{GTE}_2^i = \dfrac{\theta_{bary}^i}{\theta_{traj}^i}$. If δt is small, one can rewrite the equation to

$$\mathrm{GTE}_2 = \frac{\int_0^t \dfrac{\theta_{bary}\,(t)}{\theta_{traj}\,(t)} \cdot dt}{t} \tag{11.5}$$

   The values of GTE_1 and GTE_2 are calculated for the two simulations A and B.

11.4. Simulation results

11.4.1. Comparison of general tracking efficiencies

The resulting values for GTE_1 and GTE_2 are listed in Table 11.2 and it can be seen that the associated temporal evolution compares well. On the contrary, GTE_1^t and GTE_2^t derived from final microstructures, i.e. last simulation time-step differ significantly from GTE_1 and GTE_2 and show larger deviations with respect to each other. Additionally, the estimated GTE_2 vary with axial tilt and therefore, may lead to erroneous interpretation.

11.4.2. Statistics

It is well known from the 2D numerical studies of crack-seal process that a smaller crack-opening rate favors the formation of fibrous morphology, while, a larger crack opening rate leads to formation of blocky fracture cements [9, 241]. However, none of the

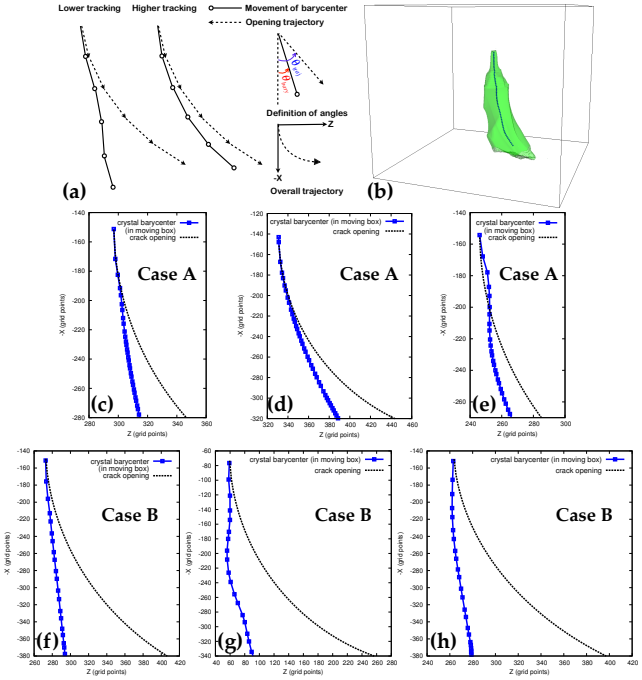

Figure 11.7.: (a) Diagram explaining the calculation of GTE_2 which accounts for the temporal evolution of tracking efficiency (GTE_2^i). The solid line represent the evolution of the crystal barycenter in the shifting box while the dashed line corresponds to crack-opening trajectory. (b) In order to account for the temporal evolution in calculation of general tracking efficiency, the barycenter of surviving crystals (in contact with advancing crack surface) is determined. For the sake of better visualization, the barycenter of one of the surviving crystal is numerically masked over its iso-surface. The GTE_2 is calculated by integrating GTE_2^i as shown in Equation 11.5 for the surviving crystals with axial tilts of (c) 5.63° (d) 42.45° and (e) 58.50° in simulation test case A and (f) 5.63° (g) 7.16° and (h) 32.01°, in B.

previous studies focuses on the statistical aspects which have the potential to provide valuable insights into the fracture cementation process. One can plot the number of grains surviving the crack opening process (in contact with the advancing crack surface)

Table 11.2.: Calculated general tracking efficiencies for the simulation test cases, A and B. Calculated values GTE_2 are comparable to the corresponding GTE_1 whereas GTE_1^t and GTE_2^t show larger deviations. This indicates that the general tracking efficiencies compare quite well provided temporal evolution is accounted for its estimation.

Simulation A				
Axial tilt	GTE_2	GTE_1	GTE_2^t	GTE_1^t
5.63°	0.473	0.491	0.234	0.685
42.45°	0.422		0.751	
58.5°	0.486		0.639	
Simulation B				
Axial tilt	GTE_2	GTE_1	GTE_2^t	GTE_1^t
5.63°	0.166	0.206	0.167	0.325
7.16°	0.204		0.254	
32.01°	0.196		0.131	

versus the temporal crack opening distance and observe a shift between the two regimes, in the present 3D simulations. As shown in Figure 11.10(a), the decline in the number of grains is significantly steeper if the crack opens at a faster rate (simulation B), as compared to the case of slower opening (simulation A). The plummeting of grain count is indicative of the anisotropy in surface energy being dominant, leading to orientation selection and growth competition, similar to free-growth conditions. In such a case, the misoriented grains are continuously eliminated by favorably oriented neighbors. On the contrary, when the crack-opening rate is smaller, the decrease in the number of grains is less steep and becomes constant, which indicates that grain boundaries are pinned by fractal peaks on the fracture surface (Hilgers et al. [241] call such peaks as *Grain Boundary Attractors*), even though the general tracking efficiency is near about 0.5 (much lesser than 1.0). The grain size distribution in the shifting box (final simulation time-step) is plotted in Figure 11.10(b) and represents those grains in contact with the advancing crack surface for the test cases A and B. On comparison, it becomes clear that the tip of the distribution shifts towards smaller mean grain sizes due to an increased pinning behavior of fractal peaks when the crack-opening rate is smaller. It is noteworthy that a major repercussion of grain-boundary/multi-junction pinning, as shown in Figure 11.8, is that the growth competition based on misorientation is suppressed. In such cases, the consumption or survival of a grain does not depend on misorientation as shown in Figure 11.9. Therefore, a higher number of grains survive the crack-sealing process as opposed to other case when crack-opening rate is faster in evidence with the result in Figure 11.10(a).

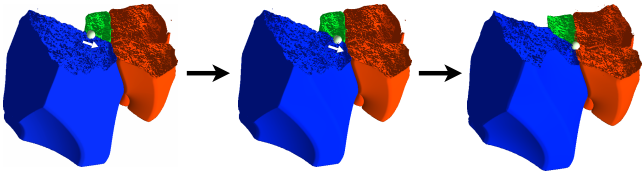

Figure 11.8.: Analysis of the temporal evolution of a fractal peak (in shifting box) which pins at the quadruple point and results in greater tracking behavior, as evident from survival of misoriented crystal fiber (in blue). The fractal peak illustrated as a white sphere acts as a grain boundary attractor while moving along a predetermined trajectory. It is interesting to note that the grain quadruple junction acts as a stronger attractor in comparison to grain boundaries, in the final stages of crack-sealing simulations (right image). The axial tilt of the grains are indexed according to the colorbar.

11.5. Discussion and outlook

The present work highlight the advantages of adopting a 3D approach, by visualizing the complex and inherently three-dimensional evolution of grain boundaries/multi-junctions in crack-sealing process. Although, the idea of using the general tracking efficiencies (GTE), as defined by Ankit et al. [9] works well for a 2D case, it is apparent that a similar procedure, in principle, cannot be employed for a general 3D case. Moreover, the previous definition of GTE by Ankit et al. [9], do not account for the temporal evolution of microstructures in the determination of tracking efficiency, which signifies the importance of present work. With a motive to account for the temporal evolution of rock microstructures, I have proposed two different approaches to determine the general tracking efficiencies and compare the results. I also clarify the main reason for a considerable influence of the crack opening rate on the grain growth statistics, i.e. on the number of grains tracking the opening trajectory, size and orientation distribution.

For obtaining a realistic wall morphology and a uniform overlay of nuclei over the crack surface which prevents the onset of size-effects, preprocessing algorithms are proposed. An innovative approach to visualize the numerically simulated fracture cements aided by post-processing techniques reveals that the grain boundary/multi-junction morphologies in 3D are more complicated as compared to 2D cases, in general. In order to deal with the third dimensionality which makes the determination of tracking efficiency difficult, I amend the definition of general tracking efficiency (GTE_1 and GTE_2) given by equations (11.3) and (11.5). While GTE_1 may be interpreted as an extension of the tracking efficiency proposed by Urai et al. [218] for the case of 3D evolution, GTE_2 accounts for the temporal change in tracking behavior of fracture cement with respect to the crack-opening trajectory. In contrast, GTE_1^t describes the tracking efficiency of the final

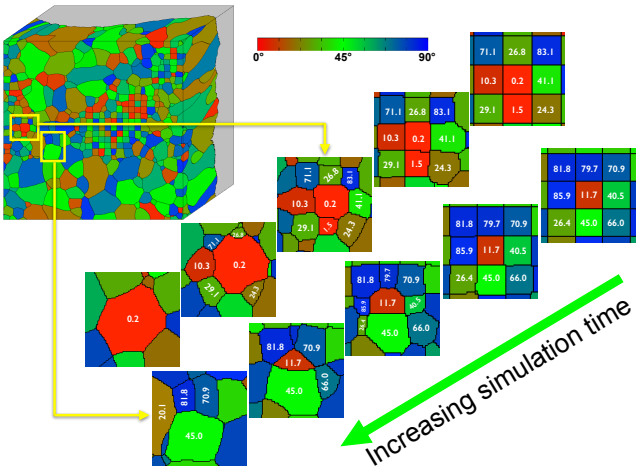

Figure 11.9.: Temporal evolution of marked areas in simulation A (slow crack-opening) show that the precipitated cement follow the trajectories of the opening peaks and evolve independently of their misorientation, with respect to the most preferred growth direction. In such a case, the grain boundaries/multi-junctions whose motion is pinned by the peaks of the advancing crack (shown in gray), track the opening trajectory. The color of the grains represent the axial tilt (numerical values also mentioned for grains in consideration) and indexed as per the colorbar.

microstructure ('t' being the total simulation time) and does not account for temporal evolution. The study of peak trajectories demonstrate that the GTE_1^t is significantly higher than GTE_1 for the simulation test cases, A and B. It is noteworthy that GTE_1 and GTE_2, both accounting for the temporal evolution of grain boundaries/multi-junctions, compare quite well as summarized in Table 11.2. The incongruousness arising out of the neglect of temporal evolution of grain boundaries/multi-junctions implies that conclusions about the tracking efficiency, as previously drawn upon the GTE_1^t data, which solely rely on final microstructure have a clearly limited validity. While the original approach of using grain boundary morphology to determine tracking efficiency proves to be inept in 3D, I comprehend that the proposed GTEs, both accounting the temporal evolution, serve as reliable methods to quantify the tracking behavior in cemented fractures.

The grain evolution statistics obtained by post-processing the 3D computational microstructure reveals that the number of grains in contact with advancing crack surface (Figure 11.10(a)) decreases steeply when the crack-opening rate is higher. It can be

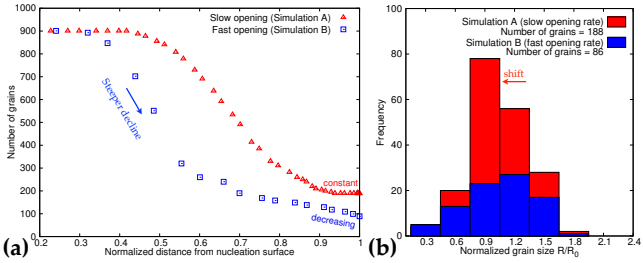

Figure 11.10.: Statistics obtained from 3D phase-field simulations. (a) Number of grains in contact with the advancing crack surface plotted as function of normalized distance from the point of greatest depression on the nucleation surface. The number of grains become nearly constant when grain boundaries/triple points are pinned at facing peaks for small crack-opening rate. At higher crack-opening rates, the growth competition dominates due to a lesser 'pinning effect' evident from a decreasing trend, even at later stages. (b) Grain size distribution for the final microstructures shown in figure 11.6. In the case of slower crack-opening, a shift of distribution peak towards smaller normalized grain size signifies greater pinning leading to higher grain boundary tracking efficiency.

argued that a steep decline in the number of grains and survival of crystals oriented along the most preferred orientation, is indicative of growth competition, which does not relate to the boundary conditions namely the crack surface roughness or the opening rate. The near incapability of fractal peaks to pin the grain boundaries/multi-junctions when crack-opening rate is higher can be seen in Figures 11.6(c) and 11.6(d), where reddish grains are found in majority. On the contrary, the decline in the number of grains is less steep for smaller crack opening rate, which finally becomes constant. Such a statistic can be attributed to stronger pinning of fractal peaks at grain boundaries and multi-junctions, which suppresses the growth competition based on misorientation of neighboring grains (Figure 11.9). An interesting outcome of visualizing the temporal evolution in Figure 11.8, is that the fractal peaks pin more strongly at quadruple junctions (grain multi-junctions in general) as compared to grain boundaries. The increase in pinning behavior of fractal peaks at smaller crack-opening rates is further accentuated by shift in the apex of grain size distribution towards small grain size (Figure 11.10(b)). Thus, the plots of number of surviving grains as well as grain size distribution (Figure 11.10), provide a statistical realization of the shift in regime and explain the fracture cement characteristics observed in Figure 11.9, which is primarily governed by crack-opening velocity in the present test cases (different from curvature driven grain coarsening process).

Finally, it is worth clarifying that the present definitions of GTEs are formulated with an

intention to indicate the importance of temporal evolution in determining the tracking efficiency. One cannot rule out the possibility of other definitions, which may be equally capable to quantify tracking behavior in 3D with high precision. Based on the insights from the present numerical simulations, I assert that as long as the temporal evolution and the 3D characteristics of the growing cement is accounted for, the derived tracking efficiency can, in principle, be calculated correctly, irrespective of the technique used. Within the scope of current work, the prime motive is to highlight the gain in accuracy by accounting for temporal evolution in the well known methodologies, which strongly emphasizes the importance of 3D numerical studies. The growth statistics, obtained by accounting for large number of grains and supplemented by 3D visualization, aims to bridge the gap between field observations (of 3D layers) and computational studies (limited to 2D till date) and advances the understanding of the fracture cementation process.

The current work which is based on diffused interface modeling approach, namely the phase-field method aims to fill-in the short-comings while focusing on the aspects that have not been addressed in the previous numerical studies. In particular, the complex motion of grain boundaries/multi-junctions have been analyzed on the basis of large-scale simulations in 3D. Wherever required, the benefits of 3D simulations have been highlighted while enumerating the limitations of 2D studies. The 3D visualization aided by post-processing techniques supplement the present numerical studies and allow to draw meaningful conclusions from the simulation test cases. A close agreement of both the general tracking efficiencies (GTE_1 and GTE_2) for the test cases 'A' and 'B', validates my findings and confirms that the aim of conducting the numerical simulations has been adequately achieved. The most outstanding achievement of the present work is the characterization of rock microstructures based on temporal evolution of grain boundaries/multi-junctions rather than relying on an approximate reconstruction from the final morphology, a popular approach in the geoscientific community [264]. Bearing in mind that it is fundamentally (essentially) difficult to design as well as carry out in-situ studies in laboratory experiments that can replicate the process of fracture cementation (e.g., Okamoto and Sekine [239], Hilgers et al. [265]), the 3D numerical studies are of paramount importance as they can alternatively provide invaluable insights into the fracture cementation process.

12. Microstructural evolution in bitaxial crack-seal veins

The aim of this final section of Part B is to investigate the evolution of bitaxial crack-seal microstructures in 3-D using the phase-field technique. A systematic study to explore the effects of changing the crack-opening vector and location of the crack, on the vein texture and grain statistics is presented. A reasonable agreement between the numerically simulated and natural microstructures is also established. This chapter was published in [11].

12.1. Model test case - effect of input parameters

The basic building block of microstructural evolution in the domain considered in the present section is the propagation of a grain boundary (GB) during a crack-seal event. In the case of unitaxial growth, the grain boundary grows against an inert template, but in bitaxial growth, the two grain boundaries will generally join towards the end of a sealing event. In order to explore the effect of different input parameters on the evolving GB morphology during bitaxial growth, I consider a test case of 2 grains separated by a grain boundary. The crack cuts across the grains, which are then displaced along an opening vector and the gap is sealed as shown in Figure 12.1. Note that the incorporation of crack is a simple geometric operation without any physical changes in the model. In these simulations, the interfacial energy of the evolving grains is assumed to be isotropic (no facet formation) by considering $a_{\alpha\beta} = 1$ in Equation 4.3. Two instances of phase-field simulations are analyzed (a) for small shear displacement ($10\Delta x$, where Δx is the grid size for finite-difference solver) and (b) for larger shear displacement ($30\Delta x$). Results show that oblique GBs ($\theta = 55\,^{\circ}$) evolve at small shear displacement. If the ratio is larger, a stair-stepped morphology with smooth corners develops. This can be compared with results of Urai et al. [218] which show sharper stair-stepped grain boundaries.

I conduct a first sensitivity analysis to study the influence of different simulation parameters on the formation of stair-stepped or oblique GB, as shown in Figure 12.2[1]. It is evident from a near-overlap of the contour plots shown in Figure 12.2(a) that varying the isotropic surface energy coefficient ($\gamma_{\alpha\beta}$) by an order of magnitude, do *not* result in a different GB morphology, for small normal crack-opening displacements. Similarly, when

[1]Such an analyses was included in the present study on the advise of J.U. and B.N. The analyses was carried out by K.A.

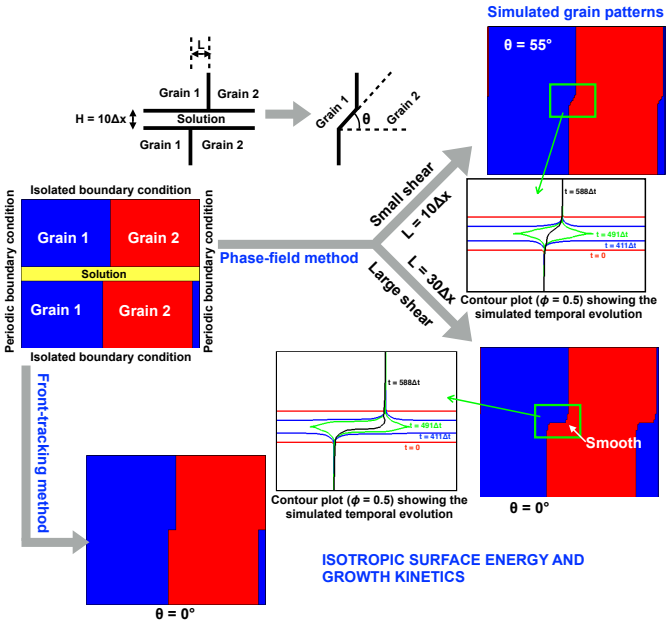

Figure 12.1.: The GB morphologies simulated by the phase-field approach for the syntaxial sealing of two grains. The surface energy of evolving grains are assumed to be isotropic and the crack aperture is constant (H = $10\Delta x$) for both the cases. The angle (θ) defined as per the schematic diagram above approaches zero for larger shear openings (L = $30\Delta x$),. The adjacent contour plot shows the temporal evolution of GBs to a smooth stair-stepped morphology. For a smaller shear displacement of the crack (L = $10\Delta x$), an oblique GB is obtained. The stair stepped morphology with sharp corners that is obtained from front-tracking method is also illustrated alongside.

the simulated GBs possessing the surface energies of cubic, left-handed and right-handed quartz crystals (where both the grains are oriented along the most-preferred growth direction) are compared to the isotropic case, an appreciable deviation is not found, as shown in Figure 12.2(b). The chosen crack aperture (equal to $10\Delta x$ as shown in inset of Fig. 12.1) for the present anisotropic case is sufficiently small to ensure complete sealing before the facets develop and same as the aperture size used for an isotropic case in Figure 12.2(a). Small deviations in the simulated GB are observed on varying the

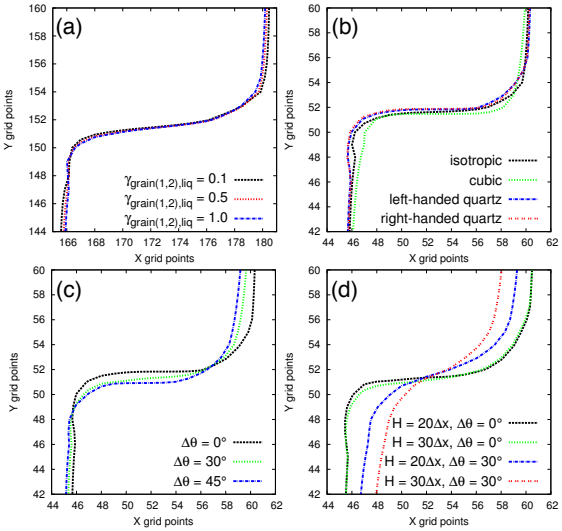

Figure 12.2.: Contour plots to demonstrate the sensitivity of the numerically simulated GB morphologies w.r.t input parameters. (a) Effect of solid-liquid interfacial energy (assumed to be isotropic for this case) parameter for constant values of H (crack aperture) and L (crack shear displacement). A deviation in the simulated morphologies is not observed. (b) Incorporation of the anisotropy in solid-liquid interfacial energy, that corresponds to cubic, left-handed and a right-handed quartz crystals do not result in significant deviation in the simulated morphology when compared to the isotropic case. The misorientation difference between the grains (for anisotropic cases) is zero. In order to study the effect of misorientation (w.r.t most preferred orientation), an anisotropic solid-liquid interfacial energy pertaining to the left-handed quartz crystal is utilized for the simulation results summarized in (c). A marked deviation in the width of stair-stepping is observed as the misorientation difference is increased from 0° to 45°. (d) Effect of crack aperture and misorientation difference on the final GB morphology. The numerical interface width is considered to be 10 grid-points, for all simulations illustrated above.

relative misorientation between the grains (surface energies corresponding to left-handed quartz) as shown in Figure 12.2(c). A more detailed investigation (as shown in Figure 12.2(d)) reveals that the relative misorientation of the grains, which is responsible for

the growth competition, lead to obliqueness (deviation from stair-stepped GB), when normal crack opening displacement is high enough (H = $30\Delta x$). At this point, it is worth iterating that the phase-field method is a diffuse-interface modeling approach, in which the interface between two grains is defined as a narrow region (of finite width) where the phase-field variables gradually vary between their values in the neighboring grains. Therefore, in order to address the phenomena of grain boundary evolution in a physically sufficient manner, it is necessary to numerically resolve the interface by a sufficient number of grid-points.

12.2. Results

Starting from an initial-setup as described in Figure 4.5, four successive crack-sealing events are simulated for normal and oblique crack opening as shown in Figures 12.3(a) and 12.3(b) respectively. The crystals are allowed to grow freely and completely fill the crack aperture following every cracking event. A significant growth competition is observed as indicated by overgrowth of blue colored crystals by red and green ones (color indicates orientation). These results can be compared with the findings of Okamoto and Sekine [239], who use the front-tracking approach to study the effect of crack aperture size and initial grain width on the growth competition in syntaxial veins (in 2D). It is also apparent that oblique opening of the crack results in elongated grains oblique to the vein boundary, as often seen in nature. In the following sections, I analyze the grain statistics obtained from the numerical simulations of polycrystalline quartz and establish a relation of the new microstructural features obtained from the 3D simulations, using post-processing and visualization techniques developed for this study.

12.2.1. Effect of shear displacement

The 3D computational microstructures after every sealing step (with or without oblique opening) as shown in Figures 12.3(a) and 12.3(b) is sectioned along the growth direction into 300 slices (2D) and the number of grains is plotted against the distance from the central plane (or slice) as shown in Figures 12.4(a) and 12.4(b) respectively. As the size of the domain is held constant ($300 \times 300 \times 300$ grid points), the number of grains in the computational domain decreases, every time a fresh crack is introduced. A gradual decline in the number of grains is also observed towards the central slice in the successive crack-sealing events, which is attributed to a temporal increase in the growth competition and overgrowth of misoriented grains. A major point of difference in statistics arises when the position of minima (corresponding to the final microstructure obtained at the end of the fourth sealing step) is compared for both the cases i.e. normal and oblique crack openings. As a result of the oblique opening shown in the schematic diagram (in Figure 4.5(c)), the number of grains below the central slice are found to be considerably lower as compared to the normal (only) crack opening mode. The average grain radius per

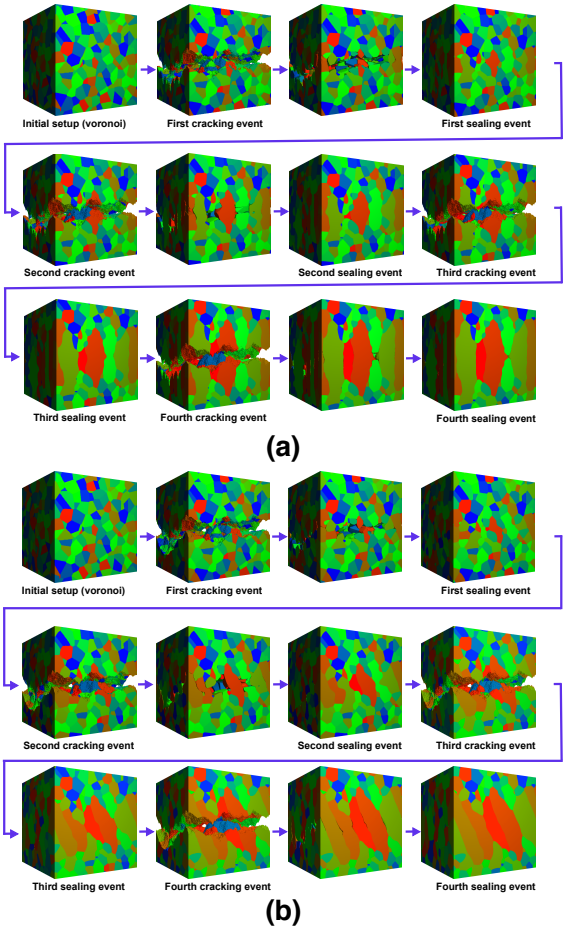

Figure 12.3.: Temporal evolution of grains when the crack opens in (a) normal direction (no shear displacement), designated as test case 'A' and (b) oblique direction (designated as test case 'B') and subsequent seals. The cracking event takes place at same position within the growing vein, as shown in Figure 4.5.

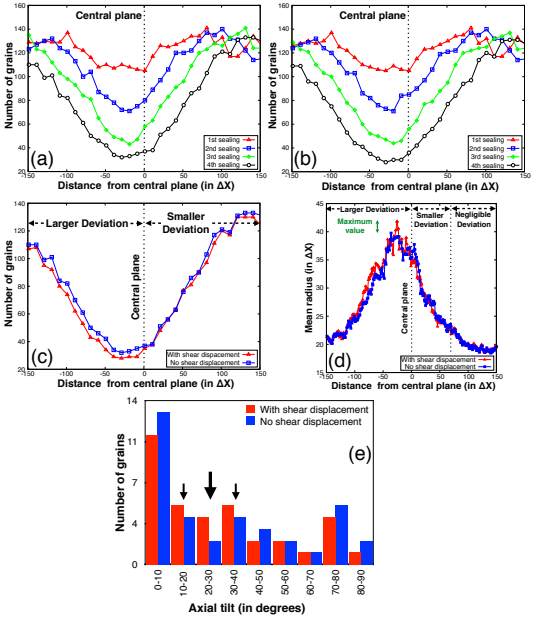

Figure 12.4.: Grain statistics signifying the effect of shear displacement in bitaxial sealing. The 3D computational microstructure obtained after every sealing step is sliced along the vein growth direction and number of grains are plotted against the slice distance (from central plane) for (a) normal opening and (b) oblique opening modes. (c) The number of grains present along the median plane and (d) the mean radius (for every slice) are compared, after the fourth sealing step, for the test cases 'A' and 'B'. On comparing statistics obtained from both the simulation instances, a larger deviation is observed for the lower half of the computational domain. (e) Histogram comparing the distribution of grain axial-tilt for the central slice of the 3D microstructure obtained after the final sealing event for both the test cases 'A' (normal opening with no shear displacement) and 'B' (oblique opening displacement). As indicated by the big arrow, a distinct reversal in the distribution trend is observed close to the direction of crack-opening displacement vector, for the test case 'B' (opening angle = 26.56°).

slice obtained for the case of oblique opening are much higher as compared to the normal (only) crack opening mode. A shift of the minima towards left (in Figure 12.4(c)) and a

higher mean radius of grains (in Figure 12.4(d)) indicate a stronger growth competition which results from the shear displacement of lower crack surface.

This is typically characterized by depletion in number of grains and increase in surface area (reduction in grain boundary curvature), apparent from both the plots, respectively. A distinct reversal of the disorientation distribution close to an axial tilt of 26.56°, as shown in Figure 12.4(e), solicits comparison with EBSD measurements for natural samples.

12.2.2. Grain-scale microstructures

The three-dimensional iso-surface of the grains present in the computational microstructure obtained after the fourth (final) crack-sealing event are visualized for both the crack-opening modes. Two distinct features are identified namely (a) stretched crystals and (b) crystal fragments. It must be recalled that the simulation parameters (grain size and crack aperture etc.) were set such that most of the initial crystals do not survive. It is interesting to note that the crystals whose c-axes are favorably oriented for growth are also outgrown by their neighbors, as a result of difference in grain boundary curvature that is directly related to grain size. A detailed description of both these microstructural features is provided in the following sections.

12.2.2.1. Stretched crystals

The stretched crystals are defined by an irregular jagged shape of the grain boundaries, in both the normal (in Figures 12.5(a) – 12.5(d)) and oblique crack opening mode (in Figures 12.5(e) – 12.5(h)). The cumulative opening vector correlates with the overall

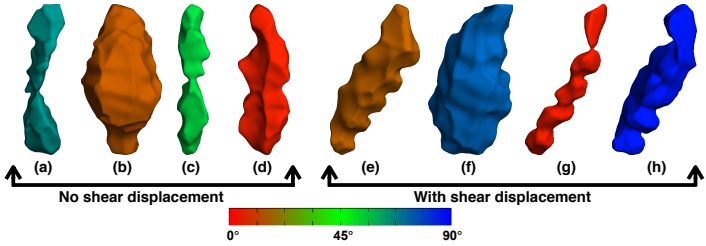

Figure 12.5.: Simulated 3D iso-surfaces of grains with axial tilts of (a) 66.929° (b) 14.711° (c) 55.84° (d) 5.695° (e) 15.441° (f) 74.246° (g) 4.982° (h) 86.171°. The iso-surfaces shown in figs. (a)-(d) are obtained by opening the crack in the normal direction (no shear displacement) while (e)-(h) are obtained by opening the crack obliquely.

shape of the stretched grains, and the wavelength of the irregularities in the grain shape is similar to the opening vectors, however, as already stated by Urai et al. [218], the individual opening-increments cannot be deduced. The full scale of orientations of the crystals in Figure 12.5 (shades of red, blue and green) suggest that all grain orientation have the opportunity to stretch. This can be attributed to the effect of grain size on growth competition, as explained below.

Another common and interesting feature that is observed during the initial stages of sealing, is the formation of crystal bridges [176], as shown in Figure B1. (Note: in the present simulations, I have assumed that the cracks are completely sealed prior to every new crack event; in future studies, I will also explore cracking during incomplete sealing, which can be easily accomplished using the present technique). Here, favorably oriented grains outgrow their neighbors to reach the upper wall. At this point the bridge starts to grow in the lateral direction. The formation of crystal bridges is not only an outcome of relative misorientation, but also of non-uniform size of the grains at the start of epitaxial growth.

12.2.2.2. Crystal fragments

In the vast majority of cases in the present simulations, as a result of growth competition, fractured crystals fail to join by sealing. Such non-joining crystal pairs are shown in Figure 12.6. I call these as crystals 'fragments' in the present thesis. Obviously, such

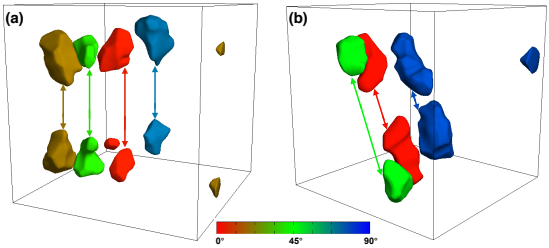

Figure 12.6.: The non-joining fragments formed when the crack opens along (a) normal direction (test case 'A' - no shear displacement) and (b) oblique direction (test case 'B'). The double headed arrows are meant to highlight the fragmented pairs.

fragments (which can often be recognized in natural samples on both sides of syntaxial veins) define the cumulative crack-opening, however they do not contain information about the opening trajectory [219].

Figure 12.7 shows a special class of regularly-spaced crystal-fragments that are extracted from the simulated microstructure and found to co-exist with stretched crystals and other

fragmented pairs. A distinct patterning of such crystal fragments is observed, which

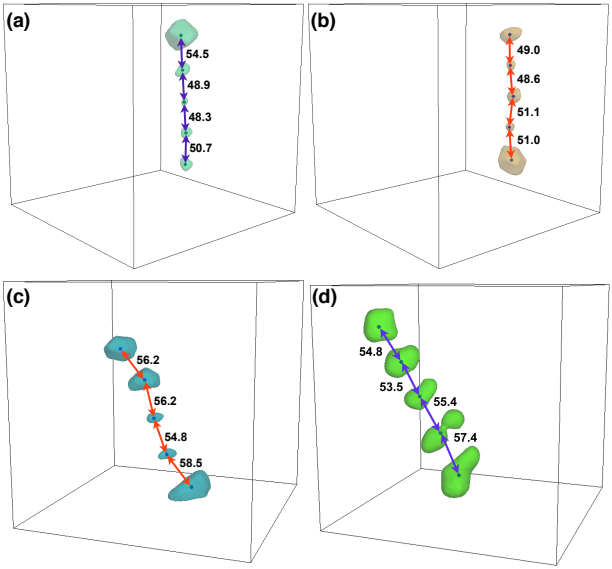

Figure 12.7.: Position of fragment barycenters (shown by dots) and inter-barycenter distance (indicated by arrows) for the crystal tilted at (a) 60.1° (b) 18.5° in normal crack-opening mode (crack displacement of 50 grid points) and (c) 36.6° (d) 68.4° for oblique opening mode (net displacement of 56 grid points). The simulation boxes used for calculating inter-barycenter distance shown above are reconstructed using numerical post-processing techniques since crystal fragments span across edges in the original domain. To overcome the problem of spanning crystal fragments across the box edges which results in erroneous calculation, the original domain is duplicated along the spanning boundaries. Further, the reconstructed domain is truncated to discard partial crystal fragments along the edges. Transparency of reconstructed crystal fragments facilitate better visualization of numerically masked barycenters.

belong to the same parent crystal (in the initial Voronoi setup) for both normal and oblique displacement. When the vectors between the barycenter of adjacent fragments are measured, as shown in Figure 12.7, these are found to be equal to the crack opening increment vector. The spatial arrangement of the fragments thus contain information

on the opening trajectory. In order to validate the above findings, I performed multiple simulations with the same crack-opening increments, but with different grain sets. In all the test cases, presence of fragment trails is observed. It is interesting that no preferred orientations are produced in any of the test-cases (see crystal coloring in Figures 12.6 and 12.7). I would like to point out that in the present model, the fractures are introduced at the mid-plane of the simulation domain. This results in repetitive cleavage of one or more fragments (formed during previous crack-opening event). Therefore, the number of fragments in such a case is equal to the number of sequential crack-sealing events.

Having recognized the ipseity of crystal fragments in the present phase-field simulations that are predicted to be similar to those seen in the natural microstructures, it is important to comprehend the mechanism of formation. Figure 12.8 shows the temporal cracking and joining of 3D crystal fragments, along with a 2D slice of the simulation domain, corresponding to the test case 'B'[2]. The parent crystal (designated as '1' and shown in green) breaks into two fragments 1.1. and 1.2. The intermittent space is sealed by more favorably oriented crystal (reddish in color). In the second cracking event, the former (1.1) breaks into two fragments. I prefer to rename the bigger fragment (of the two daughter fragments) as 1.1, while the smaller one is designated as 1.2.1. Fragment 1.2 remains intact during the second cracking event. On completion of the second sealing event, three fragments exist (1.1, 1.2.1 and 1.2). In the third cracking event, the crack splits the crystal-fragments, 1.2.1 and 1.1, into two. I prefer calling the daughter fragment from 1.2.1 as 1.2.1.1, while, the fragment breaking off from 1.1 is designated 1.1.1. It is noteworthy that the crystal fragments, which form during the preceding crack-sealing events, are derivatives of the parent crystal '1'. On chalking out the crystal lineage, it is seen that the fragments 1.1.1 and 1.2.1.1 can be considered as grand-daughter and great-grand daughter fragments of '1', respectively. A reunion of 1.1.1 and 1.2.1.1 is observed during the third sealing event. I designate the new fragment, which is formed as result of the reunification of 1.1.1 and 1.2.1.1 as 2.1. The joining of the crystal fragments is a significant evolution step, considering the information concerning crack-opening increment, which is of the present interest. In the following cracking event (fourth), 2.1 splits into two fragments, designated as 2.1.1 and 2.1.2, which do not join, as they are overgrown by neighboring grains. I would like clarify that it is perfectly acceptable to adopt a naming convention depending on the sequence of crack-sealing event rather than the size. The main point that I wish to state here is that adopting either one of the two naming conventions does not change the origin of any of the daughter fragments which is uniquely described by the corresponding axial tilt (or color).

[2]Analysis of temporally evolving fragments illustrated in figure 12.8 (prepared by K.A.) is based on a discussion with J.U.

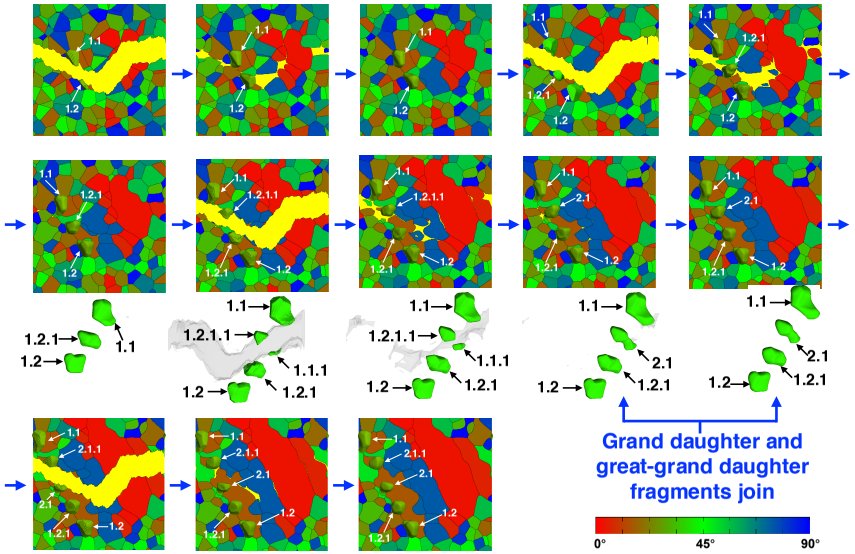

Figure 12.8.: Temporal evolution of iso-surfaces of crystal fragment (same as Figure 12.7(d)) along with a representative 2D slice of the 3D simulation domain, shown in Figure 12.3(b). Repeated cracking (normal and oblique opening) lead to the formation of fragments which belong to the parent crystal '1'. The daughter fragments 1.1 and 1.2, are overgrown by favorably oriented neighbors and contribute to the formation of grand daughter and great-grand daughter fragments in the successive crack-sealing steps. The grand and the great-grand daughter fragment join (1.2.1 and 1.2.1.1) and leads to the formation of 2.1, as there is no favorably oriented grain in the vicinity. The iso-surfaces of the fragments along with the crack surface (rendered as transparent) is also shown for the time-steps when progenies re-unite, which explain the overall mechanism of fragmentation.

12.2.2.3. Fracture connectivity during sealing

Fracture porosity and its effect on the flow behavior of partially sealed natural fracture networks [266] has important technological applications. The formation of the initial faceted overgrowth changes the dependence of flow rate on aperture, and the initial formation of crystal bridges has a large effect on the stiffness of the fracture and its closure under decreasing pore pressure. The final sealing of the fracture by crystal growth forming a vein restores rock strength, produces a flow barrier, and a mechanical heterogeneity that will have a strong effect on the propagation of both natural and man-made fractures. Here I explore how fluid percolation evolves as the grains seal the crack aperture after every crack-opening event. For this, I extract the 2D central slice (as shown in Figure 12.9(a)) from test cases 'A' and 'B' and image the temporal evolution of the liquid area fraction. Similarly, one can render the surface of the temporally evolving liquid, as shown in the Figure 12.9(b) and tabulate the volume fraction corresponding to every simulated time-step. In order to decompose the effect of shear displacement, I compare the temporal evolution of the liquid volume fractions for the two cases 'A' and 'B'. Results show that the time required to completely seal the vein progressively decreases after every crack-sealing event, for both normal and oblique opening (Figure 12.9(c)). This can be explained by considering that the grain size on the crack surface increases in each localized crack event, and large grains take longer to develop full facets. The morphology of the fluid volume not only shows that the development of crystal bridges that prevent crack closure takes place early in the process, but also that when about 20% of the crack volume is not yet sealed, the fluid loses its percolation and transport of solute to the precipitation sites can not occur in a free fluid along the crack, but rather by grain boundary triple tube diffusion or through connected matrix porosity [176].

I also compare the temporal evolution of percolation in 3D volume with the areal sealing rate in a central 2D slice as shown in Figure 12.9(d). The present simulations show that the actual volumetric sealing is slower than the areal sealing rates in 2D sections (central slice). The complete sealing of the vein involves the delinking of inter-connected channels which, in principle, is a slow process considering the sluggish growth of lateral facets [177].

12.2.3. Effect of delocalized cracking

Finally, I investigate the influence of delocalized cracking and subsequent sealing on the evolution of vein microstructure. Starting from a voronoi distribution of 1000 grains (in 2D), the same crack as in the other simulations is introduced in the numerical domain but now at one of the three predetermined positions namely 'A', 'B' and 'C' as shown in Figure 12.10. For the present test cases in 2D, the crack-opening displacement is constrained along the normal direction. It is found that the crystal growth competition in the delocalized cracking case is significantly lower as compared to the cases where crack-opening events are localized. This is related to the creation of new small seed

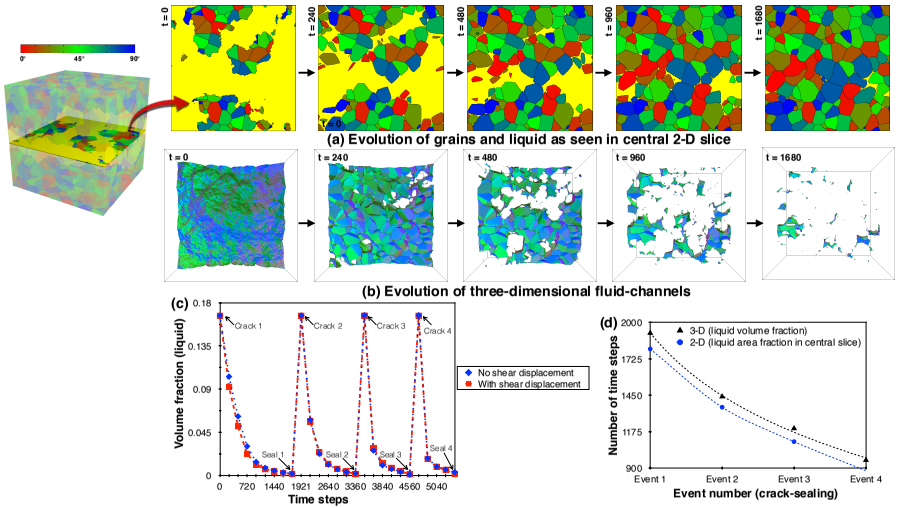

Figure 12.9.: (a) Temporal evolution of grains and liquid as observed in the central 2D slice of a 3D numerical domain. (b) A time sequence of the corresponding liquid iso-surface (as shown in (a)). A gradual decline in liquid volume fraction, as the grains evolve, refers to loss of percolation. (c) The plot showing the temporal evolution of liquid volume fraction for the two test cases 'A' (only normal crack-opening) and 'B' (crack-opening with normal as well as shear displacement). On comparison, it is apparent that the shear displacement do not influence the rate at which liquid percolation is lost. (d) The plot comparing the volumetric (accounting the temporally evolving volume fraction of the liquid) with areal sealing rate (accounting the temporally evolving area fraction of the liquid in 2D slice).

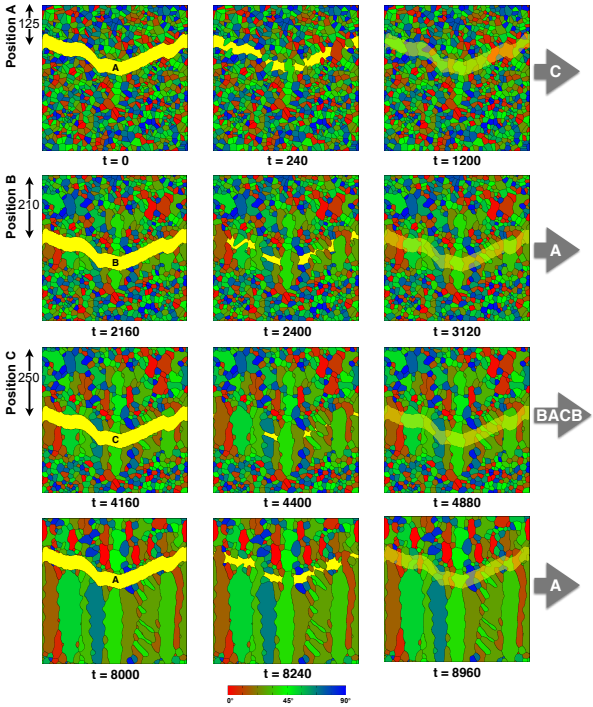

Figure 12.10.: Temporal evolution of veins illustrating the influence of delocalized cracking. Positions A, B and C are defined at distances (measured from the upper edge of the numerical domain) of 125, 210 and 250 grid-points, respectively as illustrated in the figure. The vein cracks at predetermined positions namely 'A', 'B' and 'C' in a random order. 11 successive cracking and sealing events are simulated in the order ACBACBACBAA. However, due to constraint of space only 4 sealing events have been illustrated. Grey arrows marked with the alphabets A, B and C represent the broken sequence. The translucent cracks overlaid on the sealed microstructures facilitate the distinction between the reuniting and non-reuniting grains. The crack opening displacement in the normal direction is chosen to be sufficiently high so that the growth competition occurs. The same is evident by the formation of crystal bridges (see Figure B1) at the intermittent stages. Regularly spaced crystal fragments can be identified along with the stretched counterparts after the tenth sealing event in the numerically simulated microstructure. The colormap refers to the misorientation w.r.t the fast growth direction (vertical).

crystals by every delocalized crack. The bridged crystals show strong tendency to grow along the lateral direction and fill up the pore spaces during the sealing of localized cracks as clearly seen in Figure 12.11(a). The thickening and thinning of grains towards the

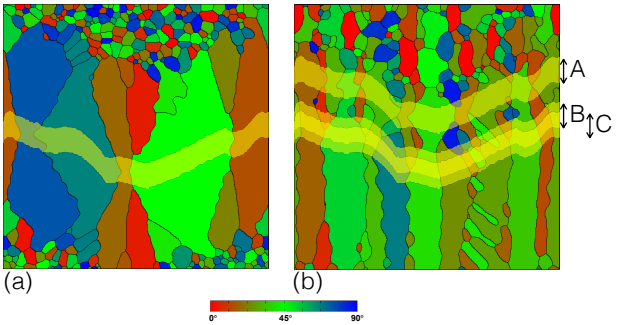

Figure 12.11.: (a) Fully localized fracturing end member. Fracturing always occur within the growing vein. (b) Random sequence of fracturing at three different positions namely 'A', 'B' and 'C'. In both cases, the crack-opening is always in the normal direction.

center of crack aperture suggests that the growth competition is high along a-axis, once the crystal bridges develop. On the contrary, when the crack-openings are delocalized along the length of the vein, the numerically simulated microstructure, as shown in Figure 12.11(b), suggests that the bridged crystals do not compete along the a-axis.

12.3. Discussion and outlook

The present simulations show that the phase-field method is a very useful tool to study microstructural development during bitaxial crack-seal process in veins. The examples presented serve as a first look on the influence of crack-opening trajectory, aperture shape and location, polycrystalline evolution rate, initial grain size and orientations, in 3D, consistent and stable numerical scheme, which allows parametric study of all these parameters. Owing to an apparently large parameter space, it was not possible to present a detailed parametric study in this first study of bitaxial sealing in veins.

As the present modeling approach considers the anisotropy of the surface energy to describe the development of facets, it essentially differs from the formulation of growth anisotropy that is implemented by Lander and Laubach [176][3]. At this point, it should be noted that either formulations can be used and little is known about the relative

[3]The preceding sentence, written by K.A. is based upon a discussion with J.U.

importance of these parameters for quartz. At first approximation, I speculate that two important parameters controlling the evolution of microstructure are the ratio of matrix grain size and crack opening vector, together with the ratio of crack opening vector and the distance which a fractured grain needs to develop facets, which could be explored in future studies.

The present simulation results show many similarities with natural bitaxial vein microstructures, such as stretched crystals, elongate crystals oblique to the vein boundary, serrated grain boundaries, and predict new features, such as crystal fragments. The present results are also in agreement with the previous numerical studies [176, 231, 242].

Using the presented method, 3D models can be used to generate testable hypotheses for the analysis of natural vein microstructures and to compare with experimental observations. In addition, the model allows study of the of the fluid morphologies during fracture sealing, paving the way for simulations of mechanical and transport properties of partially sealed fractures in crustal reservoirs. Another interesting possibility would be to investigate the tracking efficiency of elongate crystals during oblique opening.

In the studies presented in Figures 12.1 and 12.2, I investigated the influence of different simulation parameters on the formation of stair-stepped morphologies. The 2D simulations suggest that oblique grain boundaries evolve if the shear displacement is less than the diffused interface width (ε in equation 4.1). On increasing the crack-opening shear displacement, stair stepped boundaries with smooth corners evolve. The present results are comparable with those of previous numerical studies [176, 218, 231].

The phase-field method is thus an alternative 3D approach to the front tracking of Urai et al. [218], Bons [240], Nollet et al. [242], or cellular-automaton-type model of Gale et al. [175], Lander and Laubach [176], Lander et al. [231], which are at this point limited to 2D. The description of faceted morphology by an appropriate surface energy function (equation 4.3) elegantly describes the evolution of crystals of arbitrary shape (quartz in the present article) starting from a spherical nucleus, and can describe the transition from rough surfaces to faceted interfaces during growth competition, together with the final sealing of a crack.

The present study attempts to describe precipitation of quartz in veins at a relatively low temperature, where grain boundaries are immobile. Therefore, the kinetic coefficient τ (in equation 4.6) for grain/grain interaction has been assigned suitable values to ensure stiff or immobile GBs. However, I would like to point that in future studies, changing the kinetic coefficient will offer an elegant way to simulate veins under greenschist facies conditions where recrystallization and grain growth occur simultaneously.

The 3D numerical simulations of the bitaxial crack-sealing vein microstructure that is reported for the first time, suggest that the diagnostic microstructures record the crack-opening history[4]. The crystal fragments (Figure 12.8) identified in the computational

[4]The preceding sentence, written by K.A. is based on a discussion with J.U.

microstructures for both the opening kinematics, are possible indicators of crack deformation history as they can be also identified in natural microstructures. The evolution mechanism discussed in section 12.2.2.2 result in an interesting pattern where daughter fragments are aligned along the crack-opening displacement vector. The numerically simulated crystal fragments bear a close resemblance with those observed in petrographic thin sections. However, there is very limited data on 3D grain shapes in syntaxial veins, and for a full comparison of the present results with natural microstructures, 3D observation of grain morphologies and orientations are required. Additionally, the mechanism by which stretched crystals with serrated edges evolve is clearly shown by present numerical simulations [176, 218, 220].

The difference observed in the rates of permeability decline in the bitaxially sealed 3D vein microstructure and the extracted 2D slice suggest the importance of accounting for the third spatial dimension (Figure 12.9). Statistics obtained by numerically post-processing the bitaxially sealed 3D microstructures suggest a strong influence of crack-opening displacement vector on the evolving texture (Figure 12.4(e)). The 2D simulations of the delocalized crack-sealing reveal the information rendered by the aspect ratio of the sealed vein. It is noteworthy that the vein with barrel-like morphologies (with rippled edges) evolve (Figure 12.11(a)) if the location of the repetitive crack opening displacement remains the same. On the contrary, if the location of the successive crack-openings are delocalized along the growth direction, the tendency of grain boundaries to kink or bulge near the median plane is lessened (Figure 12.11(b)).

Clearly, the present numerical study is far from being complete. Conducting more parametric studies is required in order to decipher the mechanisms by which, distinct vein patterns evolve during the crack-sealing process. Further, the numerical results need to be validated against benchmark experiments and natural examples before drawing conclusive arguments. For example, the tracking characteristics of the numerically simulated crystal fragments need to be analyzed, in detail, to comprehend their true implications.

Part V.

Concluding remarks

13. Conclusions and future directions

13.1. Summary

In this dissertation, the multiphase-field approach for modeling microstructure evolution in principally two different areas of study were developed, namely eutectoid transformation in steel and polycrystalline precipitation in geological veins. While doing so, a particular focus is placed on demonstrating the analogous steps in advancing in these two different fields. The present thesis showcases the versatility of the phase-field approach which can adapted to model the morphological transitions in different systems at the mesoscale, as long as the phase diagrams and associated free-energy densities are known (or can be approximated). Apparently, one can deduce from the presented examples that the interfacial energy (can be isotropic or anisotropic depending upon the material in consideration) plays a key role in pattern formation at the micrometer length and diffusive time scales. I strongly believe that the purpose of the present thesis, which is to decompose the influence of interfacial energies on the pattern formation process in two distinct areas of study using the phase-field method (as outlined in chapter 3), has been adequately achieved.

In the first section of chapter 2, a concise literature review highlighting the historical developments in the phase-field modeling approach and various application areas is presented. A brief discussion on the state-of-the-art techniques to model polycrystalline evolution in veins is also presented in the second section. The objectives of the present work are outlined in chapter 3 while chapter 4 explains the phase-field modeling approaches that are adopted for the scientific problems in consideration.

Part III of this thesis (chapters 5–8) concern with the modeling of eutectoid transformation in binary Fe-C steels, using the multiphase-field approach that is coupled to the CALPHAD database. Chapter 5 focuses on the pearlitic growth (cooperative mode), while the factors that drive the transition from cooperative to non-cooperative mode (resulting in divorced eutectoid) are discussed in detail, in chapter 6. The influence of preexisting configuration of the eutectoid phases and undercooling (below A_1 temperature) on the evolution of ferrite/austenite transformation front in monocrystalline as well as polycrystalline austenite are discussed in chapters 7 and 8 respectively. From a modeling perspective, a third diffusion flux along the interphase interfaces has also been incorporated in the mixed diffusion–controlled growth theory. Thus, a comprehensive theory of cooperative to non-cooperative transition is established. It is anticipated that the amended theory will contribute to an efficient tailoring of eutectoid microstructures

that are widely used in the manufacture of bearings. From an industrial perspective, it is thought that the developed approach when coupled with DICTRA would lead to the quantification of the microstructure for a range of steels.

Phase-field simulations of pattern formation in geological veins are reported in part IV of this thesis. In chapter 9, the phase-field model for polycrystalline evolution (described in chapter 4) is validated by benchmarking the freely evolving alum and quartz vein patterns against physically relevant growth laws. In chapter 10, 2D numerical simulations of unitaxial sealing are reported in order to demonstrate the capability of the phase-field technique as an efficient alternative approach for modeling vein growth, otherwise predominately investigated using front-tracking methods. In chapter 11, the numerical studies are extended to 3D and the complex evolution of veins is analyzed by innovative post-processing and visualization techniques. Finally, in chapter 12, the phase-field modeling approach is extended to study bitaxial evolution of veins in 3D. For the first time, the mechanism by which, the fragmented trails evolve is discussed. The aim of the present work is to link rock deformation history with the vein patterns that are commonly found in natural microstructures. Although, the developed model does not fully resolve the non-linear dynamics associated with mineralization, synergies between the numerically simulated and natural microstructures suggest that the objectives of the present work are adequately achieved. The presented study covers many aspects of fracturing and sealing in a rock such where epitaxial growth occurs on both sides of a crack, and new cracks form after complete sealing of the crack.

13.2. Future directions

The grand-chemical potential model that has been used to investigate eutectoid transformation in binary Fe-C need to be extended to account for the role of alloying elements such as Mn, Cr and Ni. Further, the sub-lattice approach [91, 267] needs to be incorporated in the present framework to capture the complete physics of the phase transformation phenomena which involve interstitially diffusing species. A multicomponent approach could be used to study the formation of divergent pearlite, where the interlamellar spacing increases continuously leading to a decrease in growth rate as the transformation progresses. The case of pearlite dissolution has also not been discussed extensively. In this context, a quantitative modeling approach can be adopted to study the dissolution kinetics that is much faster as compared to that of pearlite formation. The present modeling approach that is developed to study divorced eutectoid microstructures could also be extended to model it's solidification parallel, namely *divorced eutectic transformation* in spheroidal graphite (SG) irons.

In the geological arena, a thermodynamic-consistent model for mineralization need to be developed and integrated in the present framework. Convective flow need to be incorporated in the present modeling approach for making realistic prediction on the sealing rate (and thereby vein permeability). The formation of partially sealed veins and

crystal bridges need to analyzed in detail. The present study has shown that the full parameter space in this domain can be simulated using these models, including porous host rock, partial sealing, delocalized cracking and mobile grain boundaries. The phase-field method can be combined with mechanical models of fracturing (such as the Discrete Element model used by Virgo et al. [247, 248]) to calculate the location and morphology of the cracks [224]. A multi-scale modeling approach need to be adopted as it is the prerequisite for achieving a comprehensive understanding of the complex vein evolution mechanisms. Modeling of multiphase, multicomponent solidification microstructures being one of the traditional strengths of the phase-field method, the technique can also be extended to study polymineralic vein evolution.

Part VI.

Appendices

A. Surface energy parameters

Vertex Number	x	y	z
1,2	0.000	0.000	±1.000
3,4	±0.152	-0.088	0.889
5	0.000	0.175	0.889
6	0.000	-0.175	-0.889
7,8	±0.152	0.088	-0.889
9,10	±0.152	0.437	0.556
11,12	±0.455	-0.088	0.556
13,14	±0.303	-0.350	0.556
15,16	±0.152	-0.437	-0.556
17,18	±0.455	0.088	-0.556
19,20	±0.303	0.350	-0.556
21,22	±0.505	0.000	0.444
23,24	0.253	±0.437	0.444
25,26	-0.253	±0.437	0.444
27,28	±0.505	0.000	-0.444
29,30	0.253	±0.437	-0.444
31,32	-0.253	±0.437	-0.444

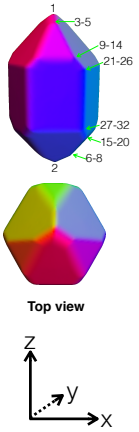

Figure A1.: The 'k' vertices (represented by $\eta_{k,\alpha\beta}$ in equation 4.3) of the 3D quartz geometry which are used to generate the surface energies of the different facets.

Table A1.: Derived facet energies for the chosen 3D quartz geometry. The interface free energy parameter, $\gamma_{\alpha\beta}$ is chosen to be equal to 1.0 for both solid/liquid and solid/solid interfaces in all the simulations.

Miller index	Surface energy
(1 0 -1 0)	$0.5\gamma_{\alpha\beta}$
(1 0 -1 1)	$0.9\gamma_{\alpha\beta}$
(0 1 -1 1)	$\gamma_{\alpha\beta}$

B. Crystal bridges

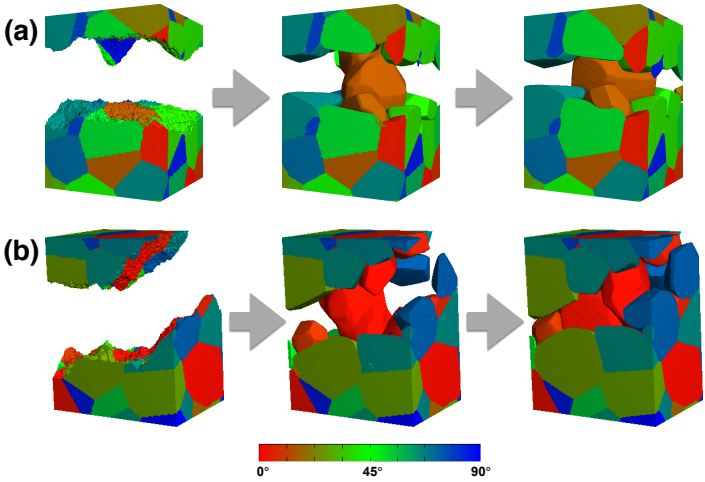

Figure B1.: Cross sections of the 3D microstructure evolution shown in Fig. 12.3 for (a) normal and (b) normal with shear displacement of the crack. The growth competition leads to accelerated growth of the favorably oriented grains (colored as red) leading to the formation of crystal bridges. The bridged crystal, whose growth is obstructed by the upper crack wall continues to evolve in the lateral directions. The cross-sectional volumes illustrated in the present figure are meant to exemplify the morphological evolution of crystal bridges. On analyzing the entire computational domain, more such crystal bridges are observed.

C. List of symbols

A. Eutectoid transformation

Symbol	Description	Units
T_E	Eutectoid temperature	K
ΔT	Undercooling	K
$\sigma_{\alpha\gamma}, \sigma_{\beta\gamma}, \sigma_{\alpha\beta}, \sigma_{\alpha\theta}, \sigma_{\theta\gamma}$	Surface energy	J/m^2
$D^{\alpha}, D^{\beta}, D^{\gamma}$	Diffusion coefficient (volume)	m^2/s
$D^{\alpha\beta}, D^{\theta\gamma}, D^{\gamma\alpha}$	Diffusion coefficient (interface)	m^2/s
ε	Parameter relating to length	m
Γ	Gibbs–Thomson coefficient	Km
$\mathcal{P}$	Trigonometric function	-
μ	Chemical potential	J/m^3
$\boldsymbol{\phi}, \boldsymbol{c}$	Phase and component vectors	-
$\alpha, \beta, \gamma, \theta$	Phase indices	-
$\eta_{\alpha}, \eta_{\beta}$	Volume fraction	-
$\theta_{\alpha\beta}, \theta_{\beta\alpha}$	Angles	degrees
m	Slopes of Liquidus/Solidus	K
k_n	Wave number	$1/m$
a	Gradient energy function	J/m^2
w	Energy potential	J/m^2
$\tau_{\alpha\gamma}, \tau_{\beta\gamma}$	Mobility	Js/m^4
Ω	Grand potential functional	J
Ψ	Grand potential density	J/m^3
Λ	Lagrange parameter	J/m^3K
g, h	Interpolation function	-
i, j, k, A, B	Component Indices	-
v	Velocity	cm/s
λ	Lamellar or interparticle spacing	μm
λ_{min}	Minimum interparticle spacing	μm
t	Time	s (if dimensional)
d_0	Particle diameter	μm
N_0	Number of preexisting particles	-
$\mathcal{L}$	Initial thickness of ferrite layer	μm
r	Radii of grain	μm

B. Vein growth

Symbol	Description	Units
ε	Parameter relating to length	m
$\boldsymbol{\phi}$	Phase vector	-
α, β	Phase indices	-
θ	Axial tilt	degrees
β	Angle	degrees
a	Gradient energy function	J/m^2
w	Energy potential	J/m^2
$\gamma_{\alpha\beta}$	Surface energy density	J/m^3
$\tau_{\alpha\beta}$	Mobility	Js/m^4
$\mathcal{F}$	Free energy functional	J
f	Bulk free energy density	J/m^3
λ	Lagrange parameter	$\mathrm{J}/m^3\mathrm{K}$
g, h	Interpolation function	-
Δt	Time-step width	s (if dimensional)
$\Delta x, \Delta y, \Delta z$	Grid-spacing	m

D. List of abbreviations

Abbreviation	Description
CALPHAD	Calculation of Phase Diagrams
L	Lamellar
D	Divorced
C	Curvature-driven coarsening
NC	Non-cooperative mode
GTE	General tracking efficiency
tp	Tracking peaks
ntp	Non-tracking peaks

Bibliography

[1] B. Nestler, H. Garcke, B. Stinner, Phys. Rev. E 71 (2005) 041609.

[2] A. Choudhury, B. Nestler, Phys. Rev. E 85 (2012) 021602.

[3] P. Gustafson, Scand. J. Metall. 14 (1985) 259-267.

[4] K. Jackson, J. Hunt, Trans. Metall. Soc. AIME 236 (1966) 1129.

[5] K. Ankit, A. Choudhury, C. Qin, S. Schulz, M. McDaniel, B. Nestler, Acta Mater. 61 (2013) 4245–4253.

[6] K. Ankit, R. Mukherjee, T. Mittnacht, B. Nestler, Acta Mater. 81 (2014) 204–210.

[7] K. Ankit, T. Mittnacht, R. Mukherjee, B. Nestler, Comp. Mater. Sci 108 (2015) 342–347.

[8] K. Ankit, R. Mukherjee, B. Nestler, Acta Mater. 97 (2015) 316–324.

[9] K. Ankit, B. Nestler, M. Selzer, M. Reichardt, Contrib. Mineral. Petr. 166 (2014) 1709–1723.

[10] K. Ankit, M. Selzer, C. Hilgers, B. Nestler, J. Petrol. Sci. Res. 4 (2015) 79–96.

[11] K. Ankit, J. Urai, B. Nestler, J. Geophys. Res.–Sol. Ea. 120 (2015) 3096–3118.

[12] L. Gránásy, L. Rátkai, A. Szállás, B. Korbuly, G. Tóth, L. Kärnyei, T. Pusztai, Metall. Mater. Trans. A 45 (2014) 1694–1719.

[13] J. Rowlinson, J. Stat. Phys. 20 (1979) 197–200.

[14] V. Ginzburg, L. Landau, Zh. Eksp. Teor. Fiz. 20 (1950) 1064–1082.

[15] J. W. Cahn, J. E. Hilliard, J. Chem. Phys. 28 (1958) 258–267.

[16] J. Langer, Dir. Condens. Matter Phys. (1986) 165–186.

[17] G. Fix, Ch. Crc. Res. Notes (1983) 580–589.

[18] J. Collins, H. Levine, Phys. Rev. B 31 (1985) 6119–6122.

[19] J. Langer, R. Sekerka, Acta Metall. Mater. 23 (1975) 1225–1237.

[20] G. Caginalp, P. Fife, Phys. Rev. B 34 (1986) 4940–4943.

[21] G. Caginalp, P. Fife, Phys. Rev. B 33 (1986) 7792–7794.

[22] G. Caginalp, E. Socolovsky, J. Comput. Phys. 95 (1991) 85–100.

[23] G. Caginalp, W. Xie, Phys. Rev. E 48 (1993) 1897–1909.

[24] G. Caginalp, J. Jones, Ann. Phys.-New York 237 (1995).

[25] O. Penrose, P. Fife, Physica D 43 (1990) 44–62.

[26] O. Penrose, P. Fife, Physica D 69 (1993) 107–113.

[27] L.-Q. Chen, A. Khachaturyan, Acta Metall. Mater. 39 (1991) 2533 – 2551.

[28] Y. Wang, L.-Q. Chen, A. Khachaturyan, Acta Metall. Mater. 41 (1993) 279 – 296.

[29] A. G. Khachaturyan, Theory of structural transformations in solids, Dover Publications Inc., 2008.

[30] L.-Q. Chen, Annu. Rev. Mater. Sci. 32 (2002) 113–140.

[31] Y. Wang, D. Banerjee, C. Su, A. Khachaturyan, Acta Mater. 46 (1998) 2983–3001.

[32] D. Li, L. Chen, Acta Mater. 47 (1998) 247–257.

[33] Y. Wang, A. Khachaturyan, Acta Mater. 45 (1997) 759–773.

[34] A. Artemev, Y. Jin, A. Khachaturyan, Acta Mater. 49 (2001) 1165–1177.

[35] Y. Li, S. Hu, Z. Liu, L. Chen, Appl. Phys. Lett. 78 (2001) 3878–3880.

[36] S. Choudhury, Y. Li, C. Krill III, L.-Q. Chen, Acta Mater. 53 (2005) 5313–5321.

[37] J. Zhang, L. Chen, Acta Mater. 53 (2005) 2845–2855.

[38] L.-Q. Chen, J. Am. Ceram. Soc. 91 (2008) 1835–1844.

[39] T. Koyama, Sci. Technol. Adv. Mater. 9 (2008) 013006.

[40] Y. Le Bouar, A. Loiseau, A. Khachaturyan, Acta Mater. 46 (1998) 2777–2788.

[41] D. Rodney, Y. Le Bouar, A. Finel, Acta Mater. 51 (2003) 17–30.

[42] A. Finel, G. Boussinot, Y. Le Bouar, Q. Bronchart, J. Mater. 56 (2004) 215.

[43] R. Folch, M. Plapp, Phys. Rev. E 72 (2005) 011602.

[44] A. Karma, W.-J. Rappel, Phys. Rev. E 53 (1996) R3017–R3020.

[45] A. Karma, W.-J. Rappel, Phys. Rev. E 57 (1998) 4323–4349.

[46] A. Karma, Phys. Rev. Lett. 87 (2001) 115701.

[47] A. Wheeler, W. Boettinger, G. McFadden, Phys. Rev. A 45 (1992) 7424–7439.

[48] S. G. Kim, W. T. Kim, T. Suzuki, Phys. Rev. E 58 (1998) 3316–3323.

[49] S. Kim, Acta Mater. 55 (2007) 4391–4399.

[50] J. Tiaden, B. Nestler, H. Diepers, I. Steinbach, Physica D 115 (1998) 73–86.

[51] P. Cha, D. Yeon, J. Yoon, Acta Mater. 49 (2001) 3925.

[52] R. Folch, M. Plapp, Phys. Rev. E 68 (2003) 106021–106024.

[53] I. Steinbach, F. Pezzolla, B. Nestler, M. Seeßelberg, R. Prieler, G. Schmitz, J. Rezende, Physica D 94 (1996) 135–147.

[54] H. Garcke, B. Nestler, B. Stinner, SIAM J. Appl. Math. 64 (2004) 775–799.

[55] R. Kobayashi, J. Warren, W. Carter, Physica D 119 (1998) 415–423.

[56] H. Kobayashi, M. Ode, S. Kim, W. Kim, T. Suzuki, Scripta Mater. 48 (2003) 689–694.

[57] L. Gránásy, T. Pusztai, T. Börzsönyi, G. Tóth, G. Tegze, J. Warren, J. Douglas, J. Mater. Res. 21 (2006) 309–319.

[58] R. Kobayashi, Physica D 63 (1993) 410–423.

[59] A. Wheeler, B. Murray, R. Schaefer, Physica D 66 (1993) 243–262.

[60] G. Ivantsov, Growth Cryst. 1 (1956) 76–65.

[61] G. Ivantsov, Growth Cryst. 3 (1959) 53–60.

[62] J. Warren, W. Boettinger, Acta Mater. 43 (1995) 689–703.

[63] W. Losert, D. Stillman, H. Cummins, P. Kopczyński, W.-J. Rappel, A. Karma, Phys. Rev. E 58 (1998) 7492–7506.

[64] D. Danilov, B. Nestler, J. Cryst. Growth 275 (2005) e177–e182.

[65] Y.-L. Huang, A. Bracchi, T. Niermann, M. Seibt, D. Danilov, B. Nestler, S. Schneider, Scripta Mater. 53 (2005) 93–97.

[66] B. Nestler, D. Danilov, A. Bracchi, Y.-L. Huang, T. Niermann, M. Seibt, S. Schneider, Mat. Sci. Eng. A 452-453 (2007) 8–14.

[67] A. Karma, Phys. Rev. E 49 (1994) 2245–2250.

[68] A. Karma, A. Sarkissian, Metall. Mater. Trans. A 27 (1996) 635–656.

[69] B. Nestler, A. Wheeler, Physica D 138 (2000) 114–133.

[70] S. Kim, W. Kim, T. Suzuki, M. Ode, J. Cryst. Growth 261 (2004) 135–158.

[71] M. Plapp, J. Cryst. Growth 303 (2007) 49–57.

[72] A. Parisi, M. Plapp, EPL 90 (2010) 26010.

[73] A. Choudhury, B. Nestler, A. Telang, M. Selzer, F. Wendler, Acta Mater. 58 (2010) 3815 – 3823.

[74] T. Lo, A. Karma, M. Plapp, Phys. Rev. E 63 (2001) 031504.

[75] D. Herlach, D. Matson, Solidification of Containerless Undercooled Melts, John Wiley & Sons, 2012.

[76] B. Nestler, A. Wheeler, L. Ratke, C. Stöcker, Physica D 141 (2000) 133–154.

[77] G. Tegze, T. Pusztai, L. Gránásy, Mat. Sci. Eng. A 413-414 (2005) 418–422.

[78] F. Wang, A. Choudhury, M. Selzer, R. Mukherjee, B. Nestler, Phys. Rev. E 86 (2012) 066318.

[79] L. Ratke, W. Thieringer, Acta Metall. Mater. 33 (1985) 1793 – 1802.

[80] F. Wang, A. Choudhury, C. Strassacker, B. Nestler, J. Chem. Phys. 137 (2012) 034702.

[81] W. J. Boettinger, J. A. Warren, C. Beckermann, A. Karma, Ann. Rev. Mater. Res. 32 (2002) 163–194.

[82] I. Singer-Loginova, H. Singer, Rep. Prog. Phys. 71 (2008).

[83] N. Moelans, B. Blanpain, P. Wollants, Calphad 32 (2008) 268–294.

[84] M. Asta, C. Beckermann, A. Karma, W. Kurz, R. Napolitano, M. Plapp, G. Purdy, M. Rappaz, R. Trivedi, Acta Mater. 57 (2009) 941–971.

[85] N. Provatas, K. Elder, Phase-Field Methods in Materials Science and Engineering, John Wiley & Sons, 2011.

[86] B. Nestler, A. Choudhury, Curr. Opin. Solid St. M. 15 (2011) 93–105.

[87] J. Christian, The Theory of Transformations in Metals and Alloys, Pergamon, Oxford, 1975.

[88] K. Thornton, J. Ågren, P. Voorhees, Acta Mater. 51 (2003) 5675–5710.

[89] D.-H. Yeon, P.-R. Cha, J.-K. Yoon, Scripta Mater. 45 (2001) 661–668.

[90] I. Loginova, J. Odqvist, G. Amberg, J. Ågren, Acta Mater. 51 (2003) 1327–1339.

[91] I. Loginova, J. Ågren, G. Amberg, Acta Mater. 52 (2004) 4055–4063.

[92] A. Yamanaka, T. Takaki, Y. Tomita, Mat. Sci. Eng. A 480 (2008) 244–252.

[93] W. Yan, N. Xiao, Y. Chen, D. Li, Comp. Mater. Sci. 81 (2014) 503–509.

[94] K. Nakajima, M. Apel, I. Steinbach, Acta Mater. 54 (2006) 3665–3672.

[95] C. Zener, Trans. AIME 167 (1946) 550–595.

[96] M. Hillert, Jernkont. Ann. 141 (1957) 757–789.

[97] I. Steinbach, M. Apel, Acta Mater. 55 (2007) 4817–4822.

[98] A. Pandit, Theory of the pearlite transformation in steels, Ph.D. thesis, University of Cambridge, 2011.

[99] A. Pandit, H. Bhadeshia, Proc. R. Soc. A-Math. Phys. 468A (2012) 2767–2778.

[100] E. P. DeGarmo, J. Black, R. A. Kohser, B. E. Klamecki, Materials and process in manufacturing, John Wiley & Sons, USA (2003).

[101] M. Mecozzi, J. Sietsma, S. Van Der Zwaag, Comp. Mater. Sci. 34 (2005) 290–297.

[102] M. Mecozzi, J. Sietsma, S. Van Der Zwaag, M. Apel, P. Schaffnit, I. Steinbach, Metall. Mater. Trans. A 36 (2005) 2327–2340.

[103] M. Mecozzi, J. Sietsma, S. Van Der Zwaag, Acta Mater. 54 (2006) 1431–1440.

[104] J. Sietsma, S. Van Der Zwaag, Acta Mater. 52 (2004) 4143–4152.

[105] M. Militzer, M. Mecozzi, J. Sietsma, S. van der Zwaag, Acta Mater. 54 (2006) 3961–3972.

[106] R. Thiessen, I. Richardson, J. Sietsma, Mat. Sci. Eng. A 427 (2006) 223–231.

[107] R. Thiessen, J. Sietsma, T. Palmer, J. Elmer, I. Richardson, Acta Mater. 55 (2007) 601–614.

[108] V. Savran, Austenite formation in C-Mn steel, Ph.D. thesis, Technical University, Delft, 2009.

[109] H. Azizi-Alizamini, M. Militzer, Int. J. Mater. Res. 101 (2010) 534–541.

[110] H. Azizi-Alizamini, M. Militzer, Solid State Phen. (2010).

[111] J. Rudnizki, B. Böttger, U. Prahl, W. Bleck, Metall. Mater. Trans. A 42 (2011) 2516–2525.

[112] T. Takaki, Y. Hisakuni, T. Hirouchi, A. Yamanaka, Y. Tomita, Comp. Mater. Sci. 45 (2009) 881–888.

[113] Y. Suwa, Y. Saito, H. Onodera, Comp. Mater. Sci. 44 (2008) 286–295.

[114] T. Takaki, Y. Tomita, Int. J. Mech. Sci. 52 (2010) 320–328.

[115] A. Vondrous, P. Bienger, S. Schreijäg, M. Selzer, D. Schneider, B. Nestler, D. Helm, R. Mönig, Comput. Mech. 55 (2015) 439–452.

[116] D. Fan, L.-Q. Chen, Acta Mater. 45 (1997) 3297–3310.

[117] Y. Suwa, Y. Saito, H. Onodera, Comp. Mater. Sci. 40 (2007) 40–50.

[118] S. Kim, Y. Park, Acta Mater. 56 (2008) 3739–3753.

[119] K.-J. Ko, P.-R. Cha, D. Srolovitz, N.-M. Hwang, Acta Mater. 57 (2009) 838–845.

[120] N. Moelans, F. Wendler, B. Nestler, Comp. Mater. Sci. 46 (2009) 479–490.

[121] Y. Suwa, Y. Saito, H. Onodera, Scripta Mater. 55 (2006) 407–410.

[122] N. Moelans, B. Blanpain, P. Wollants, Acta Mater. 55 (2007) 2173–2182.

[123] K. Chang, W. Feng, L.-Q. Chen, Acta Mater. 57 (2009) 5229–5236.

[124] M. Toloui, M. Militzer, Int. J. Mater. Res. 101 (2010) 542–548.

[125] K. Banerjee, M. Militzer, M. Perez, X. Wang, Metall. Mater. Trans. A 41 (2010) 3161–3172.

[126] A. Artemev, Y. Wang, A. Khachaturyan, Acta Mater. 48 (2000) 2503–2518.

[127] Y. Wang, A. Khachaturyan, Mat. Sci. Eng. A 438-440 (2006) 55–63.

[128] K. Bhattacharya, Microstructure of Martensite - How it forms and how it gives rise to the shape-memory effect, Oxford University Press Inc., New York, 2003.

[129] A. Saxena, A. Bishop, S. Shenoy, T. Lookman, Comp. Mater. Sci. 10 (1998).

[130] S. Shenoy, T. Lookman, A. Saxena, A. Bishop, Phys. Rev. B 60 (1999) R12537–R12541.

[131] V. Levitas, D. Preston, Phys. Rev. B 66 (2002) 134206.

[132] V. Levitas, D.-W. Lee, Phys. Rev. Lett. 99 (2007) 245701.

[133] A. Idesman, J.-Y. Cho, V. Levitas, Appl. Phys. Lett. 93 (2008) 043102.

[134] V. Levitas, D.-W. Lee, D. Preston, Int. J. Plasticity 26 (2010) 395–422.

[135] M. Mamivand, M. Zaeem, H. El Kadiri, Comp. Mater. Sci. 77 (2013) 304–311.

[136] H. Yeddu, A. Malik, J. Ågren, G. Amberg, A. Borgenstam, Acta Mater. 60 (2012) 1538–1547.

[137] H. Yeddu, A. Borgenstam, P. Hedström, J. Ågren, Mat. Sci. Eng. A 538 (2012) 173–181.

[138] H. Yeddu, V. Razumovskiy, A. Borgenstam, P. Korzhavyi, A. Ruban, J. Ågren, Acta Mater. 60 (2012) 6508–6517.

[139] A. Malik, H. Yeddu, G. Amberg, A. Borgenstam, J. Ågren, Mat. Sci. Eng. A 556 (2012) 221–232.

[140] H. Yeddu, A. Borgenstam, J. Ågren, Acta Mater. 61 (2013) 2595–2606.

[141] H. Yeddu, T. Lookman, A. Saxena, Acta Mater. 61 (2013) 6972–6982.

[142] A. Malik, G. Amberg, A. Borgenstam, J. Ågren, Acta Mater. 61 (2013) 7868–7880.

[143] A. Malik, G. Amberg, A. Borgenstam, J. Ågren, Model. Simul. Mater. Sci. 21 (2013) 085003.

[144] H. Yeddu, T. Lookman, A. Saxena, Mat. Sci. Eng. A 594 (2014) 48–51.

[145] H. Yeddu, T. Lookman, A. Saxena, J. Mater. Sci. 49 (2014) 3642–3651.

[146] H. Yeddu, T. Lookman, A. Borgenstam, J. Ågren, A. Saxena, Mat. Sci. Eng. A 608 (2014) 101–105.

[147] H. Chen, A. Chakrabarti, J. Chem. Phys. 108 (1998) 6006–6013.

[148] H. Chen, A. Chakrabarti, J. Chem. Phys. 108 (1998) 6897–6905.

[149] K. Binder, S. Puri, S. Das, J. Horbach, J. Stat. Phys. 138 (2010) 51–84.

[150] L. Gránásy, T. Pusztai, G. Tegze, J. Warren, J. Douglas, Phys. Rev. E 72 (2005) 011605.

[151] R. Folch, J. Casademunt, A. Hernández-Machado, Phys. Rev. E 61 (2000) 6632–6638.

[152] W. Oates, H. Wang, Model. Simul. Mater. Sci. 17 (2009) 064004.

[153] X. Yang, M. Forest, H. Li, C. Liu, J. Shen, Q. Wang, F. Chen, J. Comput. Phys. 236 (2013) 1 – 14.

[154] Q. Du, C. Liu, X. Wang, J. Comput. Phys. 198 (2004) 450–468.

[155] T. Biben, C. Misbah, Phys. Rev. E 67 (2003) 031908/1–031908/5.

[156] T. Biben, K. Kassner, C. Misbah, Phys. Rev. E 72 (2005) 041921.

[157] X. Wang, Q. Du, J. Math. Biol. 56 (2008) 347–371.

[158] J. Lowengrub, A. Rätz, A. Voigt, Phys. Rev. E 79 (2009) 031926.

[159] C. Peco, A. Rosolen, M. Arroyo, J. Comput. Phys. 249 (2013) 320–336.

[160] J. Oden, A. Hawkins, S. Prudhomme, Math. Mod. Meth. Appl. S. 20 (2010) 477–517.

[161] R. Travasso, E. Poiré, M. Castro, J. Rodrguez-Manzaneque, A. Hernández-Machado, PLoS ONE 6 (2011) e19989.

[162] R. Travasso, M. Castro, J. Oliveira, Philos. Mag. 91 (2011).

[163] G. Vilanova, I. Colominas, H. Gomez, Comput. Mech. 53 (2014) 449–464.

[164] F. H. Fenton, E. M. Cherry, A. Karma, W.-J. Rappel, Chaos 15 (2005) 013502.

[165] A. Karma, Annu. Rev. Condens. Matter Phys. 4 (2013) 313–337.

[166] Y. Wang, J. Li, Acta Mater. 58 (2010) 1212–1235.

[167] Y. Shibuta, Y. Okajima, T. Suzuki, Sci. Technol. Adv. Mat. 8 (2007) 511–518.

[168] H. Emmerich, Adv. Phys. 57 (2008) 1–87.

[169] H. Emmerich, J. Phys.-Condens. Mat. 21 (2009) 464103.

[170] P. Millett, M. Tonks, Curr. Opin. Solid St. M. 15 (2011) 125–133.

[171] S. F. Cox, M. A. Etheridge, Tectonophysics 92 (1983) 147 – 170.

[172] D. Koehn, C. Hilgers, P. D. Bons, C. W. Passchier, J. Struct. Geol. 22 (2000) 1311 – 1324.

[173] J. Zhang, J. B. Adams, Model. Simul. Mater. Sc. 10 (2002) 381.

[174] S. Bloch, R. Lander, L. Bonnell, AAPG Bull. 86 (2002) 301–328.

[175] L. Gale, R. Lander, R. Reed, and S. Laubach (2010), J. Struct. Geol., 32(9), 1201 – 1211.

[176] R. Lander, and S. Laubach, (2015), Geol. Soc. Am. Bull., 127(3-4), 516–538.

[177] S. Laubach, and K. Diaz-Tushman, (2009), J. Geol. Soc. London, 166(2), 349–362.

[178] J. Hubert, H. Emmerich, J. Urai, J. Metamorph. Geol. 27 (2009) 523–530.

[179] J. E. Taylor, J. W. Cahn, Physica D 112 (1998) 381 – 411.

[180] J. Eggleston, G. McFadden, P. Voorhees, Physica D 150 (2001) 91 – 103.

[181] M. Fleck, L. Mushongera, D. Pilipenko, K. Ankit, H. Emmerich, Eur. Phys. J. Plus 126 (2011) 1–11.

[182] M. Selzer, Mechanische und Strömungsmechanische Topologieoptimierung mit der Phasenfeldmethode, Ph.d., Karlsruhe Insititute of Technology, 2014.

[183] F. Wendler., A. Okamoto, and P. Blum (2015), Geofluids, doi:10.1111/gfl.1214 in press.

[184] V. Zackay, H. Aaronson, Decomposition of Austenite by Diffusional Processes, Interscience Publishers, New York, 1962.

[185] M. Kral, M. Mangan, G. Spanos, R. Rosenberg, Mater. Charact. 45 (2000) 17 – 23.

[186] M. De Graef, M. Kral, M. Hillert, JOM 58 (2006) 25–28.

[187] C. Zener, Kinetics of the Decomposition of Austenite., Wiley, NY, 1947.

[188] W. Tiller, Polyphase solidification., in: Liquid Metals and Solidification (ASM proceedings), 1958, pp. 276.

[189] I. Steinbach, M. Plapp, Continuum Mech. Therm. (2011) 1–9.

[190] H. Bhadeshia, Prog. Mater. Sci. 57 (2) (2012) 268–435.

[191] T. Oyama, O. D. Sherby, J. Wadsworth, B. Walser, Scripta Metall. Mater. 18 (8) (1984) 799–804.

[192] C. K. Syn, D. R. Lesuer, O. D. Sherby, Metall. Mater. Trans. A 25 (7) (1994) 1481–1493.

[193] E. M. Taleff, C. K. Syn, D. R. Lesuer, O. D. Sherby, Metall. Mater. Trans. A 27A (1) (1996) 111–118.

[194] J. O'Brien, W. Hosford, J. Mater. Eng. Perform. 6 (1997) 69.

[195] K. Honda, S. Saito, J. Iron Steel Inst. 102 (1920) 261–269.

[196] J. D. Verhoeven, E. D. Gibson, Metall. Mater. Trans. A 29 (4) (1998) 1181–1189.

[197] N. V. Luzginova, L. Zhao, J. Sietsma, Metall. Mater. Trans. A 39 A (3) (2008) 513–521.

[198] I. Steinbach, F. Pezzolla, Physica D 134 (1999) 385 – 393.

[199] A. Karma, W.-J. Rappel, Phys. Rev. E 53 (1996) R3017.

[200] R. Almgren, SIAM J. Appl. Math. 59 (1999) 2086–2107.

[201] M. Nicoli, M. Plapp, H. Henry, Phys. Rev. E 84 (2011) 046707.

[202] M. Plapp, Philos. Mag. 91 (2011) 25–44.

[203] I. Steinbach, Model. Simul. Mater. Sci. Eng. 17 (2009) 073001.

[204] M. Ohno, K. Matsuura, Phys. Rev. E 79 (2009) 031603.

[205] A. Choudhury, M. Plapp, B. Nestler, Phys. Rev. E 83 (2011) 051608.

[206] K. Nakajima, Y. Tanaka, Y. Hosoya, M. Apel, I. Steinbach, Mater. Sci. Forum 558-559 (2007) 1013–1020.

[207] R. Mendoza, I. Savin I, K. Thornton, P. Voorhees, Nat. Mater. 3 (2004) 385.

[208] D. Wu, Nat. Mater. 3 (2004) 353.

[209] A. Ardell, V. Ozolins, Nat. Mater. 4 (2005) 309.

[210] E. Clouet, L. Laé, T. Épicier, W. Lefebvre, M. Nastar, A. Deschamps, Nat. Mater. 5 (2006) 482.

[211] J. Hoyt, Nat. Mater. 10 (2011) 652.

[212] M. Ahmadabadi, H. Shirazi, H. Ghasemi-Nanesa, S. Nedjad, B. Poorganji, T. Furuhara, Mater. Design 32 (2011) 3526.

[213] E. Brown, G. Krauss, Metall. Trans. A 17 (1986) 31–36.

[214] J. D. Verhoeven, Metall. Mater. Trans. A 31 (2000) 2431–2438.

[215] D. Molnar, R. Mukherjee, A. Choudhury, A. Mora, P. Binkele, M. Selzer, B. Nestler, S. Schmauder, Acta Mater. 60 (20) (2012) 6961–6971.

[216] R. Mukherjee, A. Choudhury, B. Nestler, Model. Simul. Mater. Sc. 21 (7) (2013) 075012.

[217] H. S. Hasan, M. J. Peet, H. Bhadeshia, Int. J. Mater. Res. 103 A (2012) 1319-1324.

[218] J. L. Urai, P. F. Williams, H. L. M. van Roermund, J. Struct. Geol. 13 (1991) 823 – 836.

[219] D. Durney, J. Ramsay, Incremental strains measured by syntectonic crystal growths, Gravity and Tectonics (1973) 67–96.

[220] P. Bons, M. A. Elburg, and E. Gomez-Rivas (2012), J. Struct. Geol., 43(0), 33 – 62.

[221] S. Taber (1918), J. Geol., 26(1), 56–73.

[222] O. Mügge (1928), Geol. B. Bd., A(58), 303.

[223] J. Ramsay (1989), Nature, 284, 135–139.

[224] S. Laubach, R. Reed, J. Olson, R. Lander, L. Bonnell, J. Struct. Geol. 26 (2004) 967–982.

[225] S. Becker, P. Eichhubl, S. Laubach, R. Reed, R. Lander, R. Bodnar, Geol. Soc. Am. Bull. 122 (2010) 1081–1093.

[226] S. Becker„ C. Hilgers, P. Kukla, and J. Urai (2011), J. Struct. Geol., 33(4), 676 – 689.

[227] J. Nüchter, and B. Stöckhert (2007), J. Struct. Geol., 29(9), 1445 – 1462.

[228] J. Nüchter, and B. Stöckhert (2008), Tectonics, 27, TC1007 doi:10.1029/2007TC002180.

[229] S. Laubach (1997), AAPG Bull., 81, 604 – 623.

[230] S. Laubach, J. Olson, and J. Gale (2004), Earth Planet. Sc. Lett., 222, 191 – 195.

[231] R. Lander, R. Larese, and L. Bonnell (2008), AAPG Bull., 92(11), 1537–1563.

[232] M. Holland, and J. Urai (2010), J. Struct. Geol., 32(9), 1279 – 1290.

[233] C. Hilgers, and J. Urai (2002), Tectonophysics, 352, 257 – 274.

[234] C. Hilgers, and J. Urai (2005), J. Struct. Geol., 27, 481 – 494.

[235] K. van Noten, C. Hilgers, J. Urai, and M. Sintubin (2008), Geol. Belg., 11(3–4), 179 – 198.

[236] C. Hilgers, and E. Tenthorey (2004), Terra Nova, 16(4), 173 – 178.

[237] S. Nollet, C. Hilgers, and J. Urai (2006), Geofluids, 6(2), 185 – 200.

[238] A. Okamoto, H. Saishu, N. Hirano, and N. Tsuchiya (2010), Geochim. Cosmochim. Ac., 74(13), 3692 – 3706.

[239] A. Okamoto, and K. Sekine (2011), J. Struct. Geol., 33(12), 1764 – 1775.

[240] P. Bons, (2001), J. Struct. Geol., 23(6–7), 865 – 872.

[241] C. Hilgers, D. Koehn, P. Bons, and J. Urai (2001), J. Struct. Geol., 23(6–7), 873 – 885.

[242] S. Nollet, J. Urai, P. Bons, and C. Hilgers (2005), J. Struct. Geol., 27(2), 217 – 230.

[243] S. G. Kim, D. I. Kim, W. T. Kim, Y. B. Park, Phys. Rev. E 74 (2006) 061605.

[244] B. Nestler, M. Reichardt, M. Selzer, in: J. Hirsch, B. Skrotzki, G. Gottstein (Eds.), Proceedings of the 11th International Conference on Aluminium Alloys, Aachen, Germany, 2008, pp. 1251–1255.

[245] Web atlas (2014), http://www.mindat.org.

[246] B. Nestler, F. Wendler, M. Selzer, B. Stinner, H. Garcke, Phys. Rev. E 78 (2008) 011604.

[247] S. Virgo, S. Abe, and J. Urai (2013), J. Geophys. Res.-Solid Earth, 118(10), 5236–5251.

[248] S. Virgo, S. Abe, and J. Urai (2014), J. Geophys. Res.-Solid Earth, 119(12), 8708–8727.

[249] F. Renard, M. Andréani, A. Boullier, and P. Labaume (2005) Geol. Soc. Spec. Publ., 243, 67 – 79.

[250] G. S. Miller (1986), Comp. Graph., 20(4), 39–48.

[251] O. Mügge, Z. Kristallogr. 62 (1925) 415–442.

[252] J. W. Mullin, Crystallization, Butterworth-Heinemann, Oxford, 2001.

[253] O. Schmidegg, Jb. Geol. Bundesanstalt 78 (1928) 1–51.

[254] J. M. Thijssen, H. J. F. Knops, A. J. Dammers, Phys. Rev. B 45 (1992) 8650–8656.

[255] H. L. Bhat, R. I. Ristić, J. N. Sherwood, T. Shripathi, J. Cryst. Growth 121 (1992) 709 – 716.

[256] H. Klapper, R. A. Becker, D. Schmiemann, A. Faber, Cryst. Res. Technol. 37 (2002) 747–757.

[257] C. Hilgers, J. L. Urai, J. Struct. Geol. 24 (2002) 1029 – 1043.

[258] A.-J. Bons, P. D. Bons, Micropor. Mesopor. Mat. 62 (2003) 9 – 16.

[259] R. F. Sekerka, Cryst. Res. Technol. 40 (2005) 291–306.

[260] S. L. Barker, S. F. Cox, S. M. Eggins, M. K. Gagan, Earth Planet. Sc. Lett. 250 (2006) 331 – 344.

[261] A. Fournier, D. Fussell, L. Carpernter, Commun. ACM 25 (1982) 371 – 384.

[262] J. P. Lewis, ACM T. Graphic. 6 (1987) 167–190.

[263] K. Arakawa, E. Krotkov, Graph. Model Im. Proc. 58 (1996) 413–436.

[264] C. Passchier, R. Trouw, Microtectonics Springer-Verlag Berlin Heidelberg, second edition. 1996.

[265] C. Hilgers, K. Dilg-Gruschinski, J. Urai, Geology 32 (2004) 261–264.

[266] J. Olson, S. Laubach, and R. Lander (2009), AAPG Bull., 93(11), 1535 – 1549.

[267] L. Zhang, M. Startmann, Y. Du, B. Sundman, and I. Steinbach (2015), Acta Mater., 88, 156 – 169.